XPERIMENTAL EXTENDED PREDICTIONS WITH A NINE-LEVEL HEMISPHERIC MODEL

K. MIYAKODA, J. SMAGORINSKY, R. F. STRICKLER, and G. D. HEMBREE

Geophysical Fluid Dynamics Laboratory, ESSA, Princeton, N.J.

ABSTRACT

Two-week predictions were made for two winter cases by applying the Geophysical Fluid Dynamics Laboratory high-resolution, nine-level, hemispheric, moist general circulation model. Three versions of the model are discussed: Experiment 1 includes the orography but not the radiative transfer or the turbulent exchange of heat and moisture with the lower boundary; Experiment 2 accounts for all of these effects as well as land-sea contrast; Experiment 3 allows, in addition, the difference in thermal properties between the land-ice and sea-ice surfaces, as well as an 80% relative humidity condensation criterion reduced from the 100% criterion in Experiments 1 and 2.

The computed results are compared with observed data in terms of the evolution of individual cyclonic and anticyclonic patterns, the zonal mean structure of temperature, wind, and humidity, the precipitation over the United States, and the hemispheric energetics.

The forecast near sea level was considerably improved in Experiments 2 and 3 over Experiment 1. The experiment succeeded in forecasting the birth of second and third generation extratropical cyclones and their behavior thereafter. The hemispheric sum of precipitation was increased five times in Experiment 2 over that in Experiment 1, and even more in Experiment 3, the greatest contribution occurring in the Tropics. Two winter cases were considered. The correlation coefficients between the observed and the forecast patterns for the change of 500-mb geopotential height from the initial time remained above 0.5 for 13 days in one case and for 9 days in the other.

There are, however, several defects in the model. The forecast temperature was too low. In the flow pattern the intensities of the Highs and Lows weakened appreciably after 6 or 8 days, reflecting the fact that the forecast of eddy kinetic energy was less than the observed. On the other hand, the intensity of the tropospheric westerlies was too great.

CONTENTS

1. INTRODUCTION

This is an extension of the work of Smagorinsky, Strickler, et al. (1965) that was presented at the Moscow Symposium on Dynamics of Large Scale Processes in the Atmosphere. That paper discussed a set of 4-day predictions made with a general circulation model. In the present study, refined versions of that model have been applied to an extended prediction period of 2 weeks.

The period of 2 weeks was chosen for several reasons. A period of 4 days is not long enough to study the bias in the mathematical prediction model, if there is any, because the solution at the 4th day obtained by a model is still undergoing initial adjustment. Second, it may be desirable to cover the period of a *zonal index cycle* that has a characteristic time scale of 11 to 14 days. Third, there has recently been a great deal of discussion about the *predictability* of cyclone-scale systems through the hydrothermodynamical method. According to the recommenda-

tions of the Panel on International Meteorological Co-operation to the Committee on Atmospheric Sciences, National Academy of Sciences, U.S.A. (1966), "the limit of deterministic predictability for the atmosphere is about *two weeks* in the winter and somewhat longer in the summer." We, of course, agree with the concept that "it would be impossible to make determinate forecasts for arbitrarily long time intervals, because of the continuous character of the turbulent spectrum and the limitations of any observational net." It might, however, be unduly pessimistic to speculate that, within *5 days* or *10 days* or *2 weeks*, the forecast result on the synoptic scale is utterly different from the observed. One purpose of the present study is, therefore, to challenge this idea. Our attitude might seem naive to those who accept the short limit of predictability. We believe that it is still worthwhile to attack this problem from a standpoint different from previous works, even if the limit may eventually prove to be 2 weeks.

In order to make a 2-week prediction, it is quite probable that radiant energy must be considered to maintain large-scale atmospheric features. On the other hand, past experience (for example, Bushby and Hinds, 1955) tells us that the effect of the land-sea contrast is also very important even for 1- or 2-day predictions (together with the orographic effects). These effects have been included in our prediction model.

Other processes were also included in the hope of improving the prediction model. The present study contains three major experiments. Why these experiments were designed and what results were achieved will be described in the main part of this paper. Many of the details are given in the Appendixes.

2. THE PREDICTION MODEL

The basic equations used in this study were described in the papers by Smagorinsky, Manabe, and Holloway (1965) and Manabe, Smagorinsky, and Strickler (1965). The general characteristics of the model are: nine vertical levels (see table 1); primitive equations; hemispheric; $N=40$ horizontal resolution (there are 40 gridpoints between the Pole and the Equator, so the grid size is approximately 320 km at the Pole, 270 km at midlatitude, and 160 km at the Equator); "moist" model including the orography (fig. 1).

All the equations governing the atmospheric state and motion are defined on the stereographic projection map at nine vertical levels using Phillips "σ-coordinates." The lateral boundary is roughly at the Equator and is an insulated, free-slip "wall." The surface pressure is variable with time and space. The internal viscosity is Smagorinsky's nonlinear version (with effective Karman constant $k=0.4$). The surface friction is such that the drag coefficient is everywhere constant. The horizontal gradient of geopotential height is computed on constant pressure surfaces. (See Smagorinsky, Strickler, et al., 1965). The differential equations are then approximated by the Arakawa-Lilly "kinetic energy conserving" finite difference method. The entire Northern Hemisphere is covered by 5,025 gridpoints per level.

Temperature is determined by the usual thermal equation, and in addition the lapse rate is instantaneously adjusted to the dry adiabatic rate in any layer in which it is exceeded.

The hydrologic processes are incorporated. Water vapor is transferred three dimensionally by existing winds. Then the process of small-scale convection, i.e., subgrid-scale convection, is simulated by a "moist adiabatic temperature adjustment." The temperature is instantaneously adjusted to the moist adiabatic lapse rate whenever supersaturation occurs and at the same time the lapse rate exceeds the moist adiabatic lapse rate. On the other hand, large-scale condensation is assumed to take place if supersaturation occurs and the lapse rate is submoist adiabatic. The heat released by these condensation processes is fed back into the corresponding layer.

Shortwave and longwave radiation is calculated by Manabe and Strickler's (1964) scheme. Cloud coverage is taken from Telegadas and London (1954) and London (1957). These data are climatological monthly means (see tables in Appendix I) which are functions of latitude and height. The gases which act as absorbers of radiant energy, including water vapor, are climatological monthly means and are also functions of latitude and height (see table in Appendix I).

The sea-surface temperature used in this study is the January normal (fig. 2), which is assumed constant with time during the entire prediction period. The turbulent transfer of momentum, heat, and moisture in the boundary layer is taken into account. The land-surface temperature is determined through the heat balance at the surface, where the soil is assumed to have no heat capacity. The albedo of the sea is taken from Budyko (1956). The albedo of land is assumed to be a function of latitude only, taken from Kung, Bryson, and Lenschow (1964) and Posey and Clapp (1964) (see Appendix I). The "availability" of soil moisture on land (see Saltzman, 1967, for the definition), which is used for determining evapotranspiration, is assumed 0.5 everywhere over land, and 1.0 over sea. The snowline is fixed with time, and, when computing the heat budget at the ground, the surface temperature north of this snowline is not allowed to exceed 0°C (the excess heat is assumed to melt some of the snow).

It should be noted that the following effects were not taken into account: the diurnal or seasonal variations of insolation, the time and space change of albedo due to the deposit of new snow, the response with the oceans, and the time and longitudinal variation of cloud cover.

In the present study, experiments were made with three versions of the model:

Experiment 1 has no radiative transfer and no turbulent exchange of heat and moisture with the earth's surface. This result was reported previously by Smagorinsky, Strickler, et al. (1965).

Experiment 2 includes the effects of radiative transfer and turbulent exchange with the surface and also accounts for land-sea contrast.

Experiment 3 contains, in addition to these features, the difference in thermal properties between the land-ice and sea-ice surfaces, and the condensation criterion is 80% instead of 100% as in Experiments 1 and 2.

TABLE 1.—*Standard heights and pressures of the nine-level model p: pressure, p_*: surface pressure*

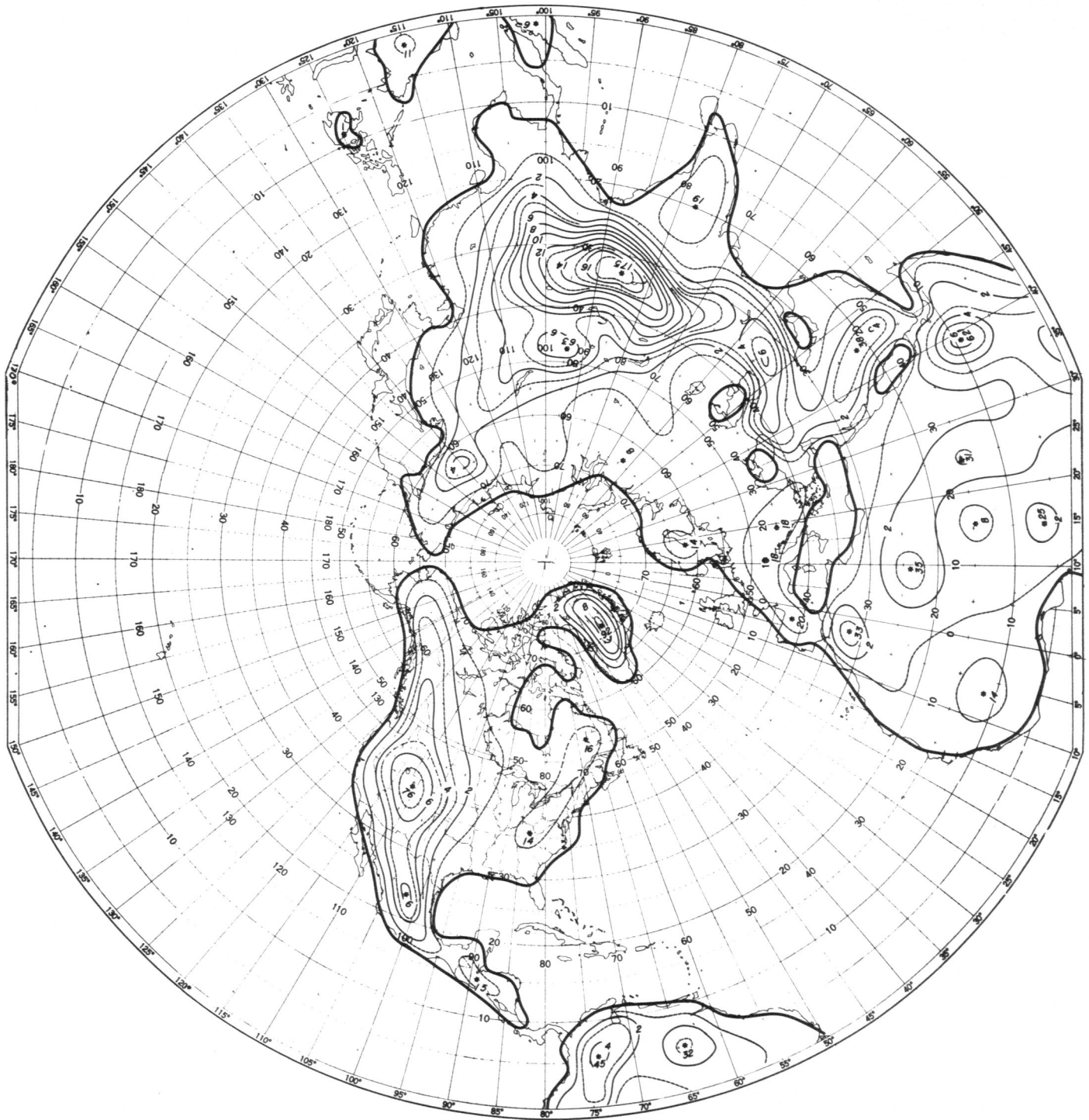| Level k	p/p_*	Standard height (km)	
1	.008916	31.60	
2	.074074	18.00	Stratosphere
3	.188615	12.00	
4	.336077	8.30	
5	.500000	5.50	
6	.663923	3.30	Troposphere
7	.811385	1.70	
8	.925926	0.64	Boundary layer
9	.991084	0.07	

FIGURE 1.—The orography. The lighter solid contours are elevations in 2,000-ft intervals and are marked by italics in thousands of feet. Extrema are indicated by stars.

The reasons for doing these particular experiments will be discussed later.

Concerning the speed of the present prediction model, 10 hr of computing time are required for each day of the prediction with the UNIVAC 1108 computer. An additional 1 hr for each day is used in checking and computing diagnostic integrals.

3. INITIAL CONDITIONS

The forecasts were made for two initial data cases. One was for the 2-week period which began 1200 GMT, Jan. 9,

1964, and the other was for the period which began 1200 GMT, Jan. 4, 1966. Note that the 1964 case was also used by Smagorinsky, Strickler, et al. (1965). The 1964 case includes Experiments 1, 2, and 3 (also referred to as 53F, 53G2, and 53J) for the three versions of the model mentioned in section 2. The 1966 case was used in the Experiment 3 version (also referred to as 61J). Analyzed aerological data were supplied by the National Meteorological Center (NMC) at Suitland, Md.

Height analyses for 11 mandatory pressure surfaces from 1000 mb to 10 mb and temperature analyses for 10 levels, from 850 mb

FIGURE 2.—Sea-surface temperature, the January normal in °K, and the sea-ice area, stippled (after U.S. Navy Hydrographic Office, 1944). The real geography is given by thin lines, and the model geography is by thick lines.

to 10 mb, were made. The moisture data for the 850-, 700-, and 500-mb levels were specially analyzed for these experiments by NMC. The initial relative humidity above 300 mb for the 1964 case was assumed 10%. We noticed later, however, that this value was too high, so for the 1966 case the value was assumed to be 0%.

The NMC data were given on the octagonal hemispheric 1,977-point grid with the grid distance equal to 408 km at the Pole. These data are redefined by linear interpolation onto the present quasi-circular 5,025-point grid with the grid distance of 320 km at the Pole.

In the operational NMC analysis, no data south of 15°N were included. The tropical area in our forecasting domain was, therefore, filled with smoothly extrapolated values for geopotential height, temperature, and water vapor, and with zero for wind velocities.

The "initialization" of the data was made by conventional techniques. The horizontal wind velocity was obtained by solving the so-called "balance equation" and the vertical velocity was by the "ω-equation."

In the following sections, for the sake of simplicity, the specific illustrations will be mostly for the 1964 case, but the results of the 1966 case are also reflected in the discussion.

4. EXPERIMENTS 1 AND 2

Figure 3 shows an important result of Experiment 1. It is the error in temperature, i.e., the forecast hemispheric mean temperature by Experiment 1 minus the observed as a function of height. It is noted that the computed temperature in midtroposphere during the forecast becomes higher than the observed, whereas in the lowest troposphere it becomes lower than the observed. The reason may be that heat was released by condensation, and there was no compensating effect such as radiative cooling, or interchange of heat with the surface. The dynamics of the atmosphere normally tends to stabilize the temperature distribution, especially in the lowest levels.

In expectation of removing this error, additional physical effects were included in the more sophisticated model used in Experiment 2. Before discussing the temperature in Experiment 2 we should first examine the time evolution of precipitation and evaporation for Experiments 1 and 2 in order to determine the difference in latent heat release. Figure 4 shows that:

1) The precipitation in Experiment 2 is five times greater than in Experiment 1.

2) The precipitation starts from small values, increases fairly rapidly, and levels off after about 4 days.

3) The rate of evaporation is large at the very beginning.

4) The rate of precipitation becomes balanced with that of evaporation as computation goes on.

To understand 1) better, it may be useful to look at the latitudinal distribution of precipitation (fig. 5). These are 24-hr rates obtained by taking the zonal and time average for Experiment 1 (0–4 days), Experiment 2 (3–14 days) and Experiment 3 (3–11 days), where the number of days in parentheses is the averaging period. As was seen in figure 4, the precipitation in Experiment 1 is already near its maximum level after the first day, so the averaging was started with the first day. One of the most noteworthy features of Experiment 1 in figure 5 is that the distribution has no maximum at the Equator, whereas those of Experiments 2 and 3 have sharp peaks at the Equator.

This shows that much of the precipitation in Experiment 2 occurs in the Tropics, though even at middle latitudes the rate of precipitation in Experiment 2 is twice as large as that in Experiment 1. This is due to both the supply of water vapor from the surface and the radiative exchanges, which are allowed in Experiment 2 but not in Experiment 1. The radiative process over land is important because together with the high sea-
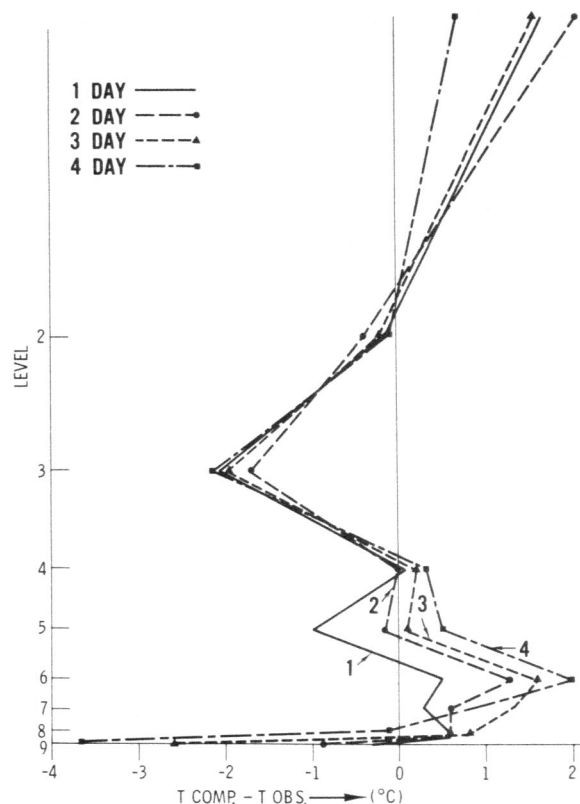

FIGURE 3.—Temperature error, i.e., the computed minus the observed temperatures, which are hemispherically averaged, in Experiment 1 is shown for 1, 2, 3, and 4 days. The ordinate is the vertical level.

surface temperatures in the Tropics it contributes to the destabilization of the atmospheric stratification. The two maxima in the precipitation distribution were also characteristic of the general circulation study (Manabe et al., 1965), in which the tropical peak was even sharper.

This may be shown more clearly by figure 6, where the latitudinal distribution of the 24-hr precipitation rate is displayed for the 1st, 3d, and 5th days for Experiment 2. The precipitation starts first in the middle latitudes, and then it develops in the Tropics. This point is related to 2) above. Our initial data have no disturbances in the tropical area, so that it takes time for tropical precipitation to develop.

Figure 7 illustrates the time evolution of the rates of precipitation at the two maxima, i.e., at 3°N and 39°N lat. It appears to take about 4 days for the tropical precipitation to reach its equilibrium although some increase is noticed after that time.

A more detailed analysis reveals that the condensation in the Tropics started over land. The disturbances apparently developed first near the tropical mountains in the initially calm Tropics, though this effect was diminished later.

As for 3) above, the larger initial rate of evaporation results from a defect in the initialization technique. The surface wind was computed by the "balance equation" excluding surface friction, so that the wind intensity was too large initially, and accordingly evaporation was intensified.
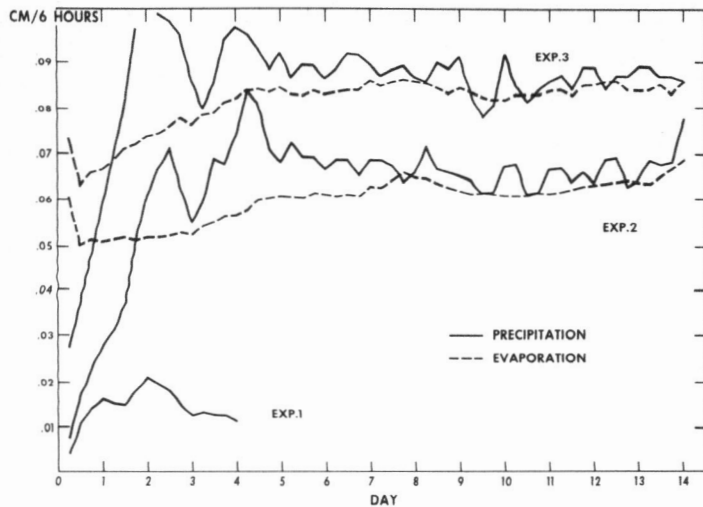
FIGURE 4.—Time evolution of the 6-hr rates of precipitation (solid lines) and evaporation (dashed lines) hemispherically averaged for Experiments 1, 2, and 3.

FIGURE 5.—Latitudinal distribution of the 24-hr rate of precipitation for Experiments 1, 2, and 3.
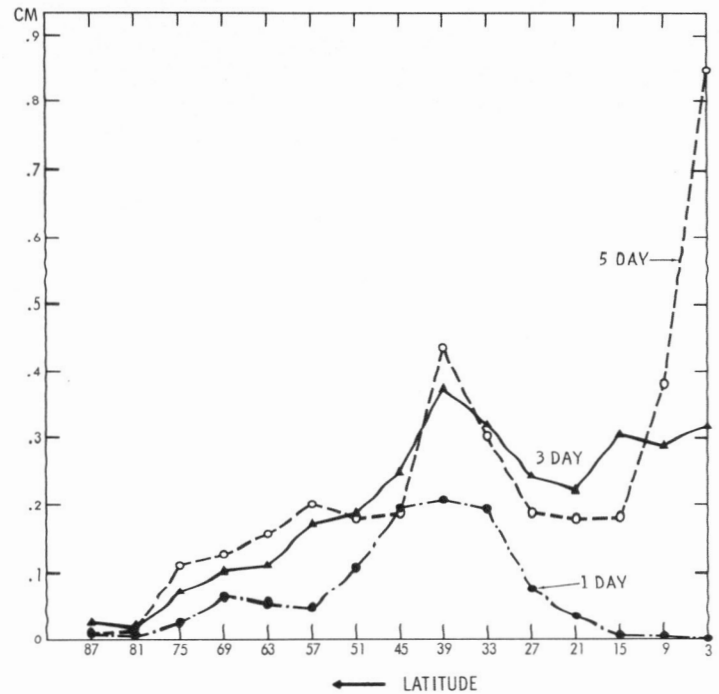

FIGURE 6.—Time variation of the latitudinal distribution of the 24-hr rate of precipitation in Experiment 2. The curves are for 1, 3, and 5 days.
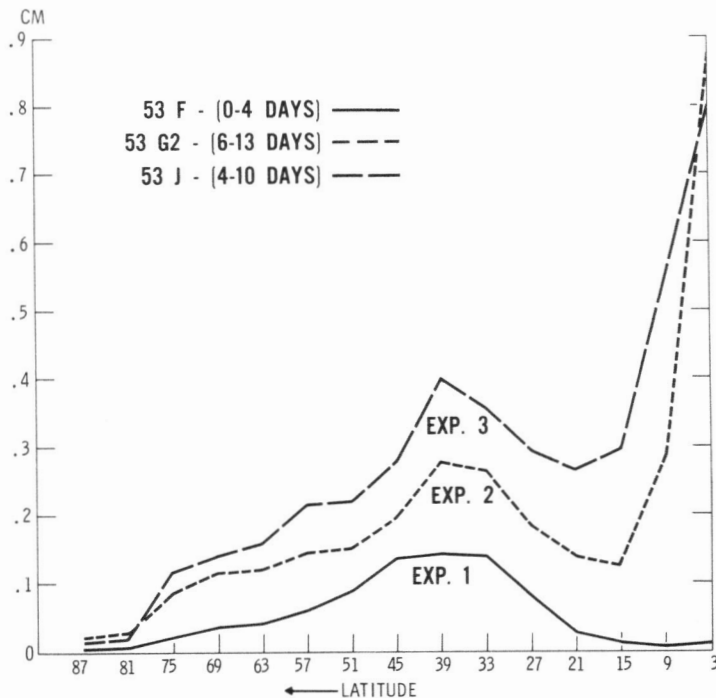

FIGURE 7.—Six-hour rates of precipitation at the two latitudes of maxima, 3° and 39°N, in Experiment 2. The abscissa is time in days.

Next, let us look at other characteristics of the precipitation forecast. Figure 8 is the land and sea distribution of precipitation for the period of 3–14 days. The dots in the figure are the estimated precipitation for winter by Möller (1951). It may be seen that in the middle latitudes the precipitation over the sea is greater than over land in both results. In the Tropics, the precipitation is much greater over land than over sea, although this tendency is not observed in Möller's result. Note that the condensation over the sea at high latitudes is extremely high. Analysis revealed that this result is due to the extreme coldness over the land and sea ice in the lower part of the model atmosphere in contrast to the relatively warm temperature of the very small area of open sea at high latitudes. We will return to this point later.

Let us next consider the heat fluxes from the surface. Figure 9 is the latitudinal distribution of the turbulent fluxes of latent and sensible heat over land and sea. The winter data from Budyko (1963) over sea are also shown. It is seen that the heat fluxes over sea at high latitudes are extremely large. As mentioned earlier, this is partly caused by the erroneous coldness over land. The effect is amplified because of the small area of open sea at high latitude in January.
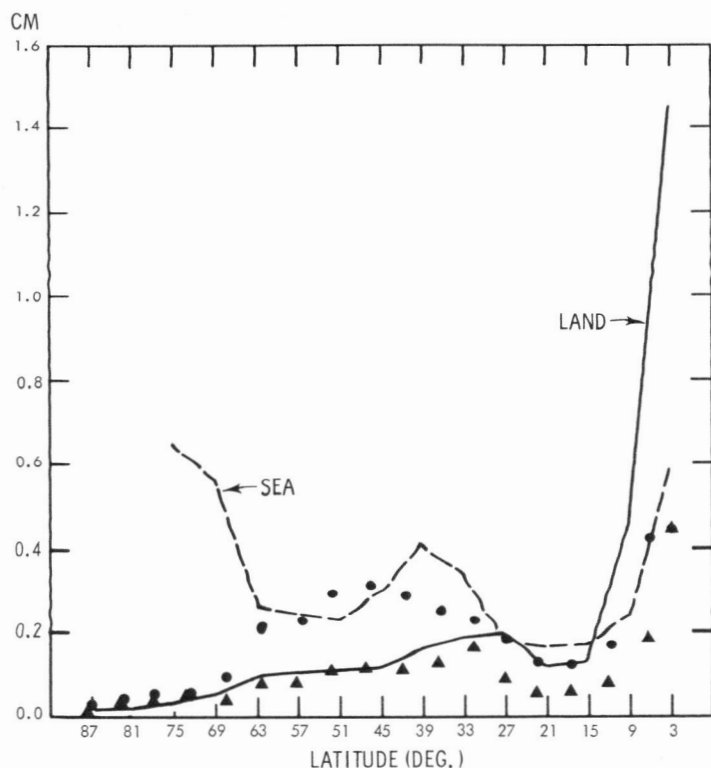
FIGURE 8.—Latitudinal distribution of the 24-hr rates of precipitation over land and sea in Experiment 2. The dots are estimated data for winter by Möller (1951). The small solid circle is for sea, and the triangle is for land.
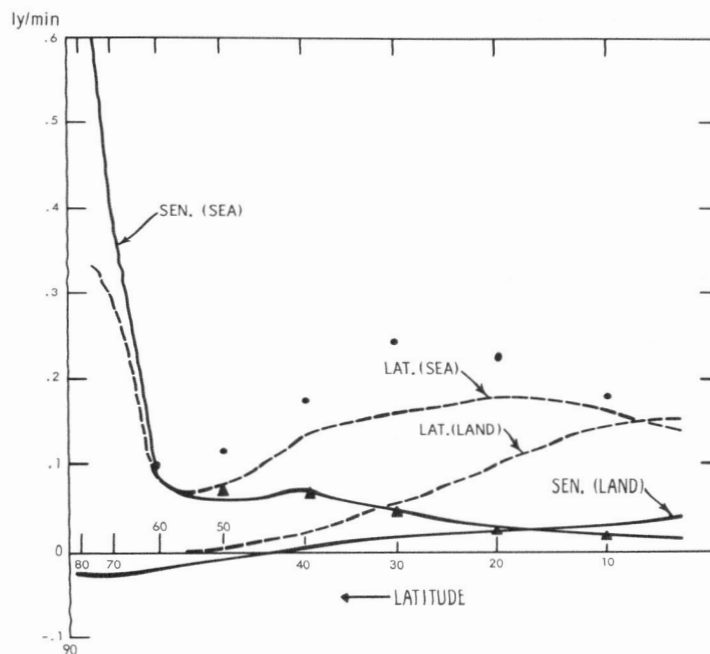

FIGURE 9.—Latitudinal distribution of turbulent heat flux at the lower boundary in Experiment 2, averaged for 14 days. SEN. (SEA) and SEN. (LAND) are the sensible heat fluxes over sea and land, respectively. LAT (SEA) and LAT (LAND) are the latent heat fluxes over sea and land. Budyko's (1963) winter values of moisture and heat fluxes over the sea are shown by small solid circles and triangles, respectively.

Now to return to the discussion of the temperature error. Figure 10 is the vertical profile of hemispheric mean temperature error in Experiment 2. Contrary to the case of Experiment 1, the computed temperature is appreciably lower than the observed. Even at the 13th day, the cooling tendency in Experiment 2 continues.

This characteristic has already been noticed by Manabe et al. (1965). In that experiment, the computed temperature at the 500-mb level was 5°C less than the observed. However, the two results are not exactly comparable, because the general circulation study treated the annual mean, whereas we are now dealing with a particular January.

To examine this degeneracy in greater detail, a height-latitude diagram of the temperature error of Experiment 2 at the 11th day is given in figure 11. We see that the cooling is especially pronounced at high latitudes near the surface and also at middle latitudes in the middle troposphere and stratosphere. The local temperature deficit at high latitudes sometimes amounted to as much as 50°C.

Because of this discrepancy, one may suspect some type of error in the radiational computation. The net transfers of radiant energy at the surface and at the top of the atmosphere have been computed and verified against those of London (1957) (see fig. 43 in Appendix II). The agreement is good. However, in our experiments we used the same cloud coverage as was used by London. It is also noted that the albedo of land at that latitude is irrelevant in

the present computation, since there is no insolation in the *polar night.*

It is thought that the excessive cooling at high latitudes may be explained, at least in part, by two effects. One is that the difference in the thermal properties of land ice and of sea ice has to be considered. Another point is that a fictitious "land breeze" effect might be accelerating the cooling tendency.

We shall return to the former in the next section, but will now discuss the "land-breeze" effect. When the land-sea contrast is accounted for in the model, a strong temperature gradient develops along the coast. Under this situation, erroneous cold spots are created if the wind blows from land to sea. Figure 12 illustrates this, though it is for Experiment 3. The temperature at level 9 sometimes becomes very low, say −50°C. Note that these temperature errors are not produced if the wind direction is from sea to land.

Our interpretation of this result is that a strong temperature gradient will produce a land breeze, but the present grid cannot properly resolve such small-scale developments (about 100 km) and a considerable truncation error is created.

In connection with the temperature discrepancy at middle latitudes which was mentioned above, one may consider the possibility that an increase in the amount of condensation may contribute toward eliminating the temperature deficit.

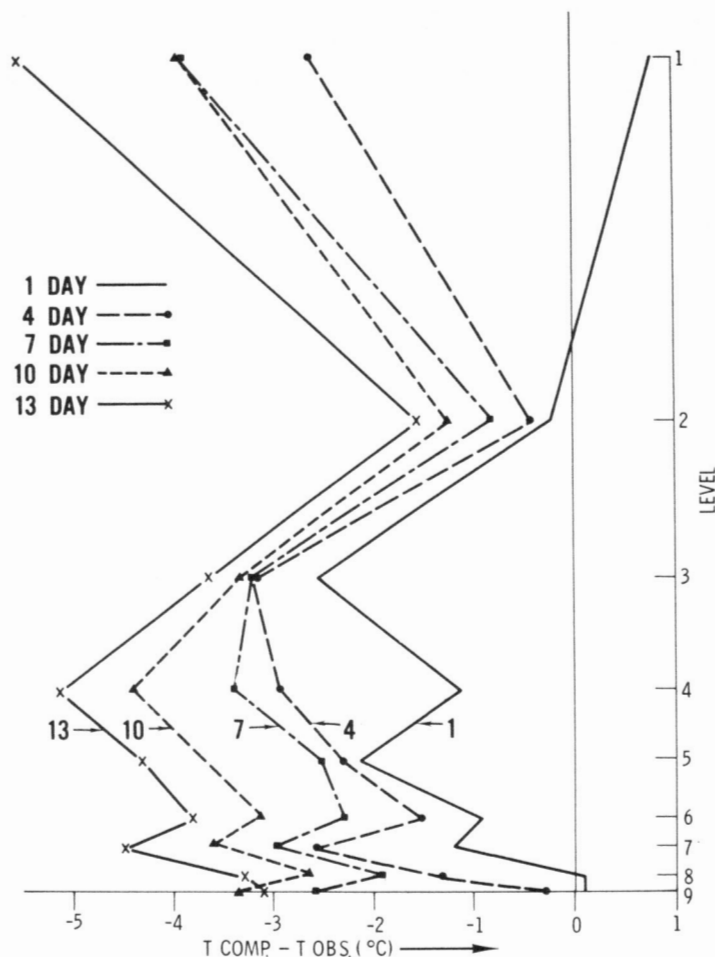As a matter of fact, the humidity computed in Experiment 2 appeared too large in comparison with the ob-

FIGURE 10.—Temperature error, i.e.,/the computed minus the ob-
served hemispherically averaged temperatures, in Experiment 2 is
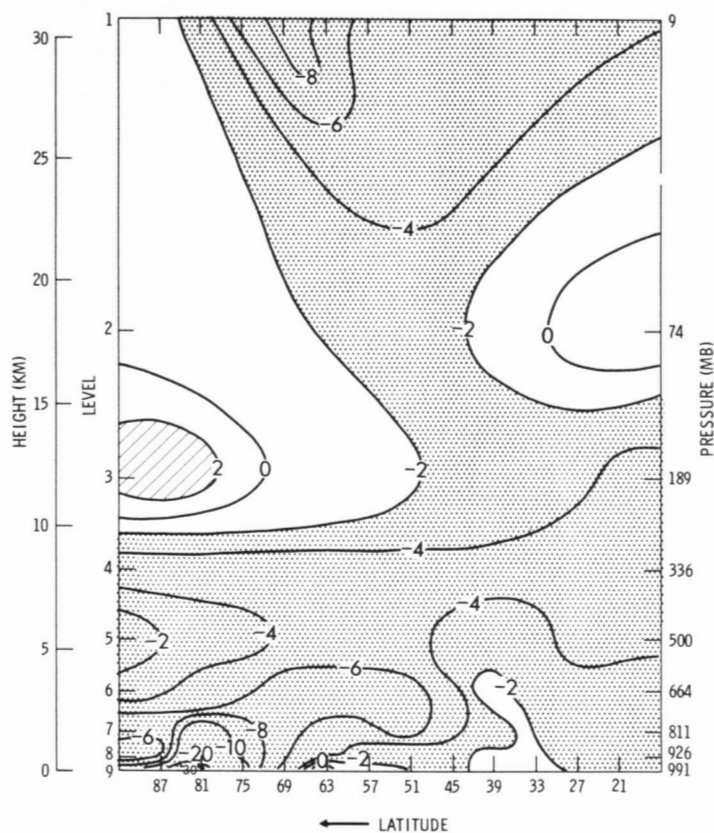shown for 1, 4, 7, 10, and 13 days.

FIGURE 11.—Meridional section of the zonally averaged tempera-
ture error in Experiment 2 for the 11th day in units of °C. The
areas where the difference is more negative than −2°C are stip-
pled, and those where the difference is larger than 2°C are shaded.
The ordinate is the vertical level.

served humidity. In figure 13 are shown the forecast
time variation of the latitudinal distribution of hu-
midity at 850 mb in Experiment 2 and the observed
variation. This may indicate that when the 100% con-
densation criterion is used, the water vapor storage is
overestimated. This tendency was also noted by Manabe
et al. (1965). In that report the humidity is found to be
even higher than in the present study (see also figs. 72–88
in Appendix III).

5. EXPERIMENT 3

In Experiment 3, the condensation criterion was set
to 80% instead of 100%. The argument for a reduced
criterion was made by Smagorinsky (1960). The hu-
midity that we are concerned with is, so to speak, the
gross humidity, which is a space-averaged quantity.
Namely, with a finite grid size the upper limit of the
relative humidity need not be 100%. If the grid size were
reduced to zero, the criterion should converge to 100%.

Presumably, the limit should also depend upon the height
and the latitude of the place at which the condensation
occurs. Since little was known about the spatial distribu-
tion of the limit, 80% was employed at all latitudes and
at all heights in the present study.

This criterion was already tested in the previous experi-
ment (Smagorinsky, Strickler, et al., 1965). It was then
concluded that only a slight increase in precipitation was
obtained in the area north of 45°N, but the precipitation
over the area south of 45°N was nearly doubled compared
to that for the 100% criterion. But the forecast period in
that experiment was only 12 hr.

This time we extended the period to 2 weeks. This
would, we hoped, provide us with a greater insight on
this problem. One could expect that the allowed water
vapor storage would be reduced by the lowered condensa-
tion criterion. Simultaneously, the rate of evaporation
would be increased, the condensation would be increased,
and accordingly more heat should be released.

Another degree of freedom added in Experiment 3 is the
distinction in the thermal properties of surface land ice
and sea ice. Recognition must be given the fact that there
is a great deal of heat conduction through solid ice over-
lying a sea surface, as well as through breaks in the ice.
According to Sverdrup et al. (1942), quoting the result of
the "Maud" expedition 1918–25, the temperature at the
surface of the ice (covered by snow) for the Northern
Hemisphere varies as shown in table 2.

In the present experiment, therefore, we assumed that
the surface temperature of the sea ice is −28.0°C. The
availability of moisture over sea ice was arbitrarily as-
sumed to be 0.5 (the same as over land).

T_9 and V_9, 3 days 53J
$[deg.°K]$

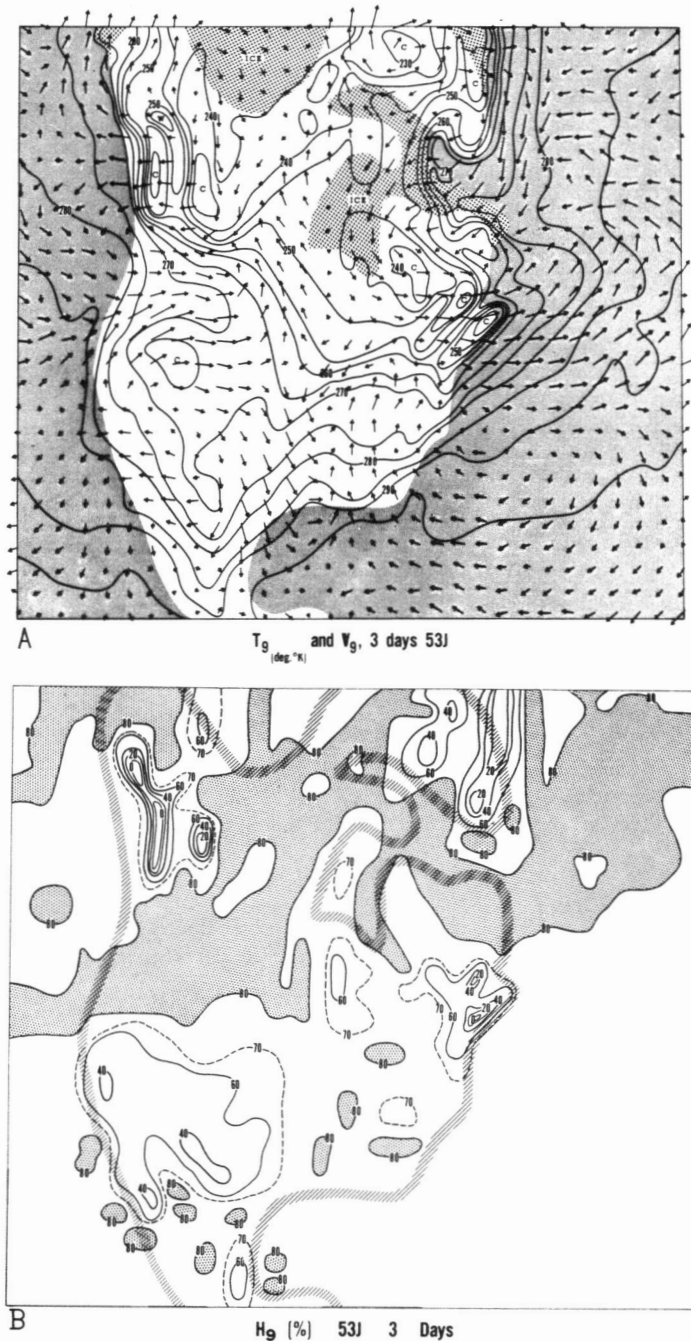A

H_9 [%]   53J   3 Days

B

FIGURE 12.—An example of the fictitious "land breeze" effect along the coast of the North American Continent at the 3d day in Experiment 3. (A) temperature at σ-level 9 is shown by contours in °K at an interval of 5°K. The wind velocity at level 9 is also illustrated by arrows. The cold spots in question are seen on both the East and the West Coast. It is noted that the extremely cold area over the sea ice in Experiment 2 is not found in this result of Experiment 3. (B) relative humidity in percent at level 9 is shown by contours. The moisture saturation area, where the relative humidity is 80%, is shaded. The coastlines are indicated by small segments of slanting lines. The erroneous cold spots in the upper figure correspond to the area where the humidity is extremely low in this figure.
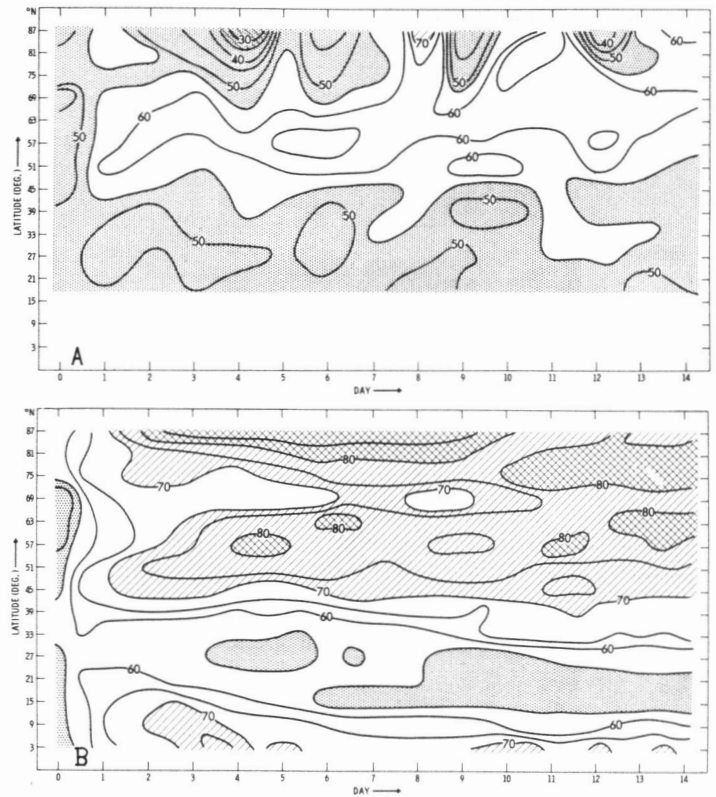
FIGURE 13.—Latitude-time diagram of the zonally averaged relative humidity in percent at the 850-mb level. (A) the observed, and (B) the computed humidity in Experiment 2. The area where humidity is higher than 70% is shaded, and that where it is less than 55% is stippled.

closer to the observed than it was in Experiment 2, as far as the 850-mb level is concerned.

Next we turn to the temperature prediction. The vertical profile of the hemispherically averaged temperature error in Experiment 3 is shown in figure 15. In comparing it with the result of Experiment 2 (fig. 10), we see that the temperatures at levels 1, 2, and 3 are not very different, but those at levels 4 through 9 have been clearly improved, especially after the first 4 days. It is noted that the temperature deficit is already large in the first 4 days. This is probably due to the deficiency in the amount of condensation at the beginning of the forecast. However, the final temperature deficit, after a sufficient period of time, may not be influenced by this initial handicap.

Figure 16 is the height-latitude diagram of the temperature error at the 11th day in Experiment 3, which corresponds to figure 11 for Experiment 2. First of all, the temperature at the lowest level at high latitude is closer to the observed temperature than that of Experiment 2, but still deficient. The middle troposphere in the sub-tropics and in the middle latitudes is slightly warmer than in Experiment 2. This is due to the increased release of heat by condensation.

Yet the computed temperature is still lower than the observed. The largest underestimation occurs at level 3 near the Tropics (not shown here). Factors which might contribute to this deficiency are the lack of a seasonal march of temperature due to the fixed zenith angle of the

Let us first look at the time variation of humidity at the 850-mb level in Experiment 3 (fig. 14). This figure can be compared with the observed humidity in figure 13. It is evident that the humidity in Experiment 3 is much

TABLE 2.—*Annual variation of the surface temperature of sea ice, after Sverdrup et al. (1942) in °C*

Jan.	Feb.	Mar.	Apr.	May	June
−28.0	−30.9	−29.1	−21.6	−7.4	−1.5
July −0.0	Aug. −0.0	Sept. −4.7	Oct. −12.3	Nov. −23.0	Dec. −29.9
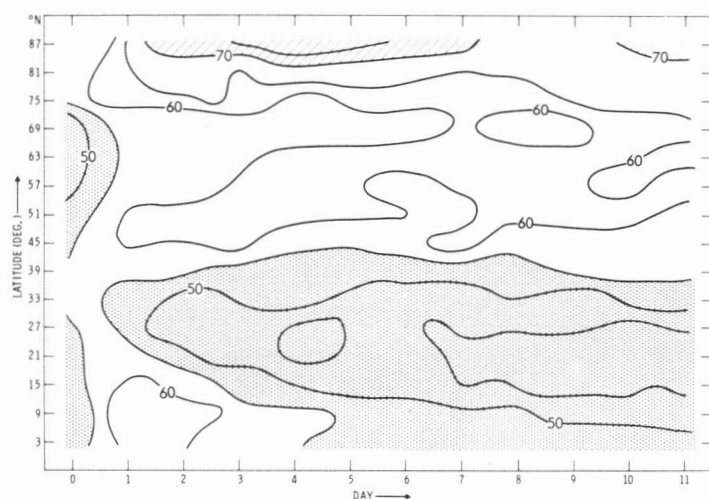
FIGURE 14.—Latitude-time diagram of the computed relative humidity in percent in Experiment 3 at the 850-mb level. This is compared with figure 13.

FIGURE 15.—Hemispherically averaged temperature error for Experiment 3 at 1, 4, 7, 10, and 13 days. The ordinate is the vertical level.

sun, and also the assumption that the heat capacity of the land is zero. The cold stratospheric temperature might be due to an abrupt drop in the vertical gradient in the mixing ratio of water vapor that is used for the radiation computations in the stratosphere (see Appendix I). This discrepancy in stratospheric temperatures will be discussed again later.

Next let us look back at the latitudinal distribution of precipitation in figure 5. It may be seen that at the Equator the precipitation in Experiment 3 is almost the same in amount as in Experiment 2, and in the middle latitude it is greater than in Experiment 2. The subtropical minimum is shifted northward, i.e., 21°N in Experiment 3 from 15°N in Experiment 2. Furthermore, the amount of precipitation at the minimum point is appreciably higher. In other words, the heat released by condensation in Experiment 3 is more evenly distributed with latitude than in Experiment 2. This is an important characteristic of Experiment 3. As will be mentioned later, this feature is relevant to the atmospheric circulation, especially in the Tropics and also to some extent in the middle latitudes.

Figure 17 distinguishes between the precipitation over the land and sea in Experiment 3; it should be compared with figure 8 for Experiment 2. One can see that the increase of precipitation in Experiment 3 over that in Experiment 2 is conspicuous over the sea. Comparing the

computed precipitation with Möller's data (1951), the precipitation over the sea in Experiment 3 is much higher. But this may not necessarily imply that the precipitation in Experiment 3 is overestimated.

The turbulent flux of heat and moisture at the surface is displayed in figure 18, which can be compared with figure 9 for Experiment 2. It is noticed that the evaporation over the ocean is increased greatly in Experiment 3 and that the sensible heat flux over the sea is decreased significantly in Experiment 3 (see the hemispheric evaporation in figure 67 of Appendix II).

The elimination in Experiment 3 of the large precipitation and the large sensible and latent heat fluxes at high latitudes over the sea is partly due to the increased temperatures of the sea ice effect. However, the areas considered are not identical in that the area covered by sea ice was included with the land points in Experiment 2 but counted as sea in Experiment 3.

6. SYNOPTIC PATTERNS

THE OBSERVED 1000-MB GEOPOTENTIAL FIELD

In short-range forecasts, i.e., 1 or 2 days, the movement of cyclones and the tendency for deepening or filling are the major problems. On the other hand, in a 2-week forecast, the life histories of cyclones are also important features of the prediction. The model should be capable of simulating all of these variations.

Before going into a discussion of the prediction results, it is perhaps useful to describe the actual evolution of the individual cyclone and anticyclone patterns of the 1964 case.
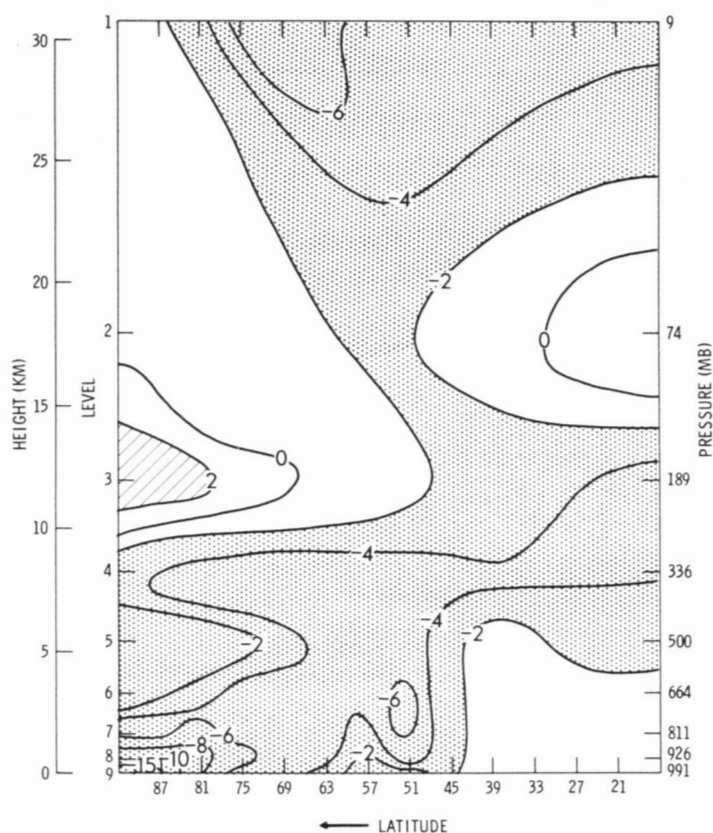
FIGURE 16.—Meridional section of zonally averaged temperature error for Experiment 3 at the 11th day in units of °C. See figure 11 for the details.
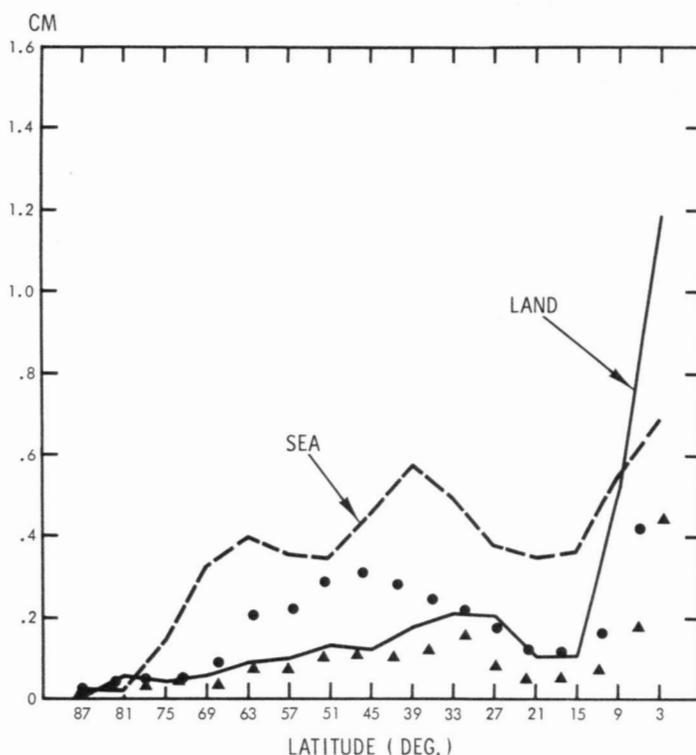

FIGURE 17.—Latitudinal distribution of the 24-hr rates of precipitation over land and sea in Experiment 3. See figure 8 for further explanation.

Figure 79 in Appendix II is the daily series of 1000-mb patterns of geopotential height for 15 days from the 9th through the 23d of January 1964. Incidentally this example was described by Sawyer (1965) in detail. As he mentioned, the most characteristic feature of this case is the *blocking anticyclone* which was located over the British Isles and persisted virtually intact from December 1963 through February 1964.

There were three major cyclones over the entire Northern Hemisphere. For the sake of convenience, we shall name these cyclones A, B, and C. A was located over the Pacific Ocean, and it moved gradually for 10 days from near Japan to the Rocky Mountains in North America. B stayed at almost the same place over the Atlantic Ocean off the west coast of Europe; it was blocked by the anticyclone. C was persistently located over northwestern Siberia.

It is interesting and important that near Formosa in Asia and over the Gulf of Mexico or sometimes near the northern Rocky Mountains, new cyclones were formed every few days. They developed rapidly within a couple of days, moved northeastward, and then merged into the preexisting major cyclones. It is likely that these cyclones are generated only when upper level vortices pass over the points in question. (Namias (1954) mentioned cases in which the genesis is related to the basic long-period mid-tropospheric wave patterns.) The areas of cyclone de-velopment correspond roughly to the so-called *west Pacific*, the *Atlantic*, and the *middle Pacific* polar frontal zones.

Let us call the newly formed cyclones A', A'', B', B'', etc. for the two regions, i.e., east of the Asian continent and over the United States, respectively. For example, A' is the second genera-tion cyclone formed over Formosa. The following is the record of new cyclones for the 2 weeks. The number in parentheses indicates the day of cyclogenesis or merging. For example, the fact that A' is merged into A is expressed by $A' \rightarrow A$.

Genesis: A' (3), A'' (8), B' (0), B'' (3), B''' (8), B^{IV} (10), B^{V} (13). B^{IV} and B^{V} were formed near the northern Rockies.

Merging: $A' \rightarrow A$ (6), A'' became major cyclone (11), $B' \rightarrow B$ (3), $B'' \rightarrow B$ (6), B''' became major cyclone (11), $B^{IV} \rightarrow B$ (14).

THE PREDICTED 1000-MB GEOPOTENTIAL FIELD

The series of the daily predicted patterns of 1000-mb geopotential height in Experiment 3 are shown in figure 49.

As seen, the blocking anticyclone continued to stay over or near Europe during the entire 2 weeks. This agrees well with the observed. Concerning the forecast of the formation and merging of cyclones, it can be safely said that the formation of the third generation cyclone B'' on the 3d day was successfully computed, and also that the merging of B'' into the major cyclone B on the 6th day was well predicted. In detail the results are as follows:

Genesis: A' (3), A'' (8), B'' (3) are successful, and B^{IV} (10) is also good. But B''' (8) and B^{V} (13) are unsuccessful. Note that B''' appeared in the prediction on the 10th day, so there was a 2-day discrepancy.

Merging: A'' became major cyclone (11) and B''' became the major cyclone (11). $B' \rightarrow B$ (3) and $B'' \rightarrow B$ (6) are successful, but $A' \rightarrow A$ (6) is not good.
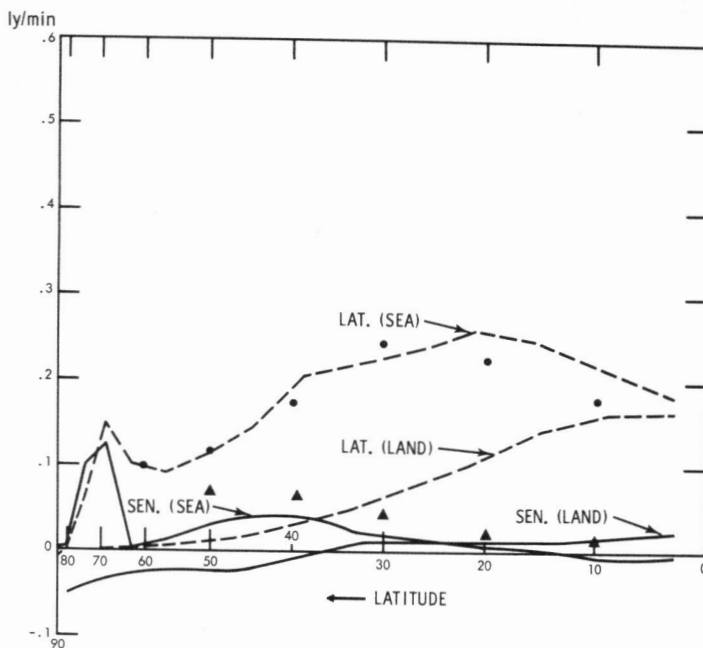
FIGURE 18.—Latitudinal distribution of turbulent heat flux at the lower boundary in Experiment 3, averaged for 10 days. See figure 9 for further explanation.

It is quite significant that even after 14 days it is possible to find a one-to-one correspondence between the cyclones of the observed and the computed patterns.

Perhaps the largest defect in the present forecasts is that the amplitude between the cyclones and anticyclones diminishes progressively and considerably with time.

Another shortcoming in the present forecast is the *wiggling* (roughness) in the pattern of geopotential height which becomes more pronounced as the computation continues. The general circulation experiments show greater wiggling with "moist" models than with "dry" models, and it also increases when the horizontal grid resolution is increased from $N=20$ to $N=40$. It is probable that the scheme for small-scale convection is partly responsible for it (Syōno and Yamasaki, 1966).

As seen in figure 49, the first great error in the present forecast occurred with the lack of development of cyclone A on the 2d and 3d days along the middle Pacific polar frontal zone. Associated with this, the merging of A' into A on the 6th day was not well computed. The reason for the failure is not clear. One may suspect that an error in the sea surface temperature pattern was responsible, but we have recently made a recomputation of the same case in which a more realistic sea surface temperature was used, and the development of A was not appreciably different. It is our present opinion that this error may be due to inadequacies in the initial data, though tangible evidence is lacking.

It is worthy of note that cyclone A, which had almost faded out, redeveloped on the 7th day when it came close to the west coast of the United States. This is a good example of how continentality might act to enhance the determinism of the atmosphere. This will be shown and discussed further in connection with the trough ridge diagram.

THE 500-MB GEOPOTENTIAL FIELD

The 500-mb geopotential forecast is in general better than the lower level forecast in any verification measure. Figure 19 shows, as an example, the 500-mb forecast for the 11th day. The rest of the results for 500 mb are given in figure 50 of Appendix II.

We see that identification of the individual troughs and ridges can easily be made between the predicted and the observed patterns. One difference between the forecast and observed patterns is that the predicted pattern is smoother in the middle scale. For instance, on some days there was an observed cutoff cyclone which did not appear in the forecast.

THE 50-MB GEOPOTENTIAL FIELD

The details of the forecast of the lower stratospheric geopotential height will be discussed in a separate paper. One important feature is the progressive decrease in temperature of the middle latitudes at about the 50-mb level. It causes the region of polar-night westerlies to be extended southward and to be connected with the tropospheric westerlies (see Appendix II).

COMPARISON OF THE GEOPOTENTIAL HEIGHT PATTERNS OF EXPERIMENTS 1, 2, AND 3

Next, let us compare the geopotential fields of the three experiments. There are important differences between Experiments 1 and 2, which can be attributed to the inclusion of land-sea contrast in Experiment 2. It is now well known that, due to the supply of the heat from the ocean, cyclone development (fig. 20) is intensified off the east coast of continents especially in winter. There has been a great deal of study of the effects of heat from the ocean. It is not appropriate to enumerate these papers here, but from the standpoint of numerical prediction models, some of the papers that discuss this point are: Bushby and Hinds (1955), Reed (1958), Spar (1960), Petterssen, Bradbury, and Pedersen (1962), and Japan Meteorological Agency (1965).

In our case also, the 1000-mb height patterns of Experiments 1 and 2 reveal a sizable difference at the 4th day. A cyclone over the Atlantic Ocean is predicted more accurately in Experiment 2 than in Experiment 1.

The difference between Experiment 2 and Experiment 3 can be illustrated by comparing figure 21 which gives the 1000-mb geopotential height for the 11th day. As was demonstrated earlier, the difference between the two experiments in the supply of heat from condensation is quite large, and, as a consequence, the amplitude of cyclones and anticyclones is larger in Experiment 3 than in Experiment 2, and the amplitude in Experiment 3 is slightly closer to that of the observed.

It is very interesting that the birth of cyclone B''' on the 8th day, which was not computed at all in Experiment 2, was successfully simulated in Experiment 3, but this cyclone was not very deep and the date of genesis was 2 days late, compared with reality.

It should be mentioned that these differences are not as large as one might suppose. One of the lessons we learned is that the midtroposphere does not seem to be particularly sensitive over periods of the order of a week to the usual external effects, such as the sea-ice effect, a 20% reduction in condensation criterion, or the sea-surface temperature anomaly, at least as far as this model is concerned.

This is a very important point in estimating the *predictability* of the atmosphere. Probably, a substantial difference between Experiment 2 and Experiment 3 will appear after the 2-week period.

THE TROUGH AND RIDGE DIAGRAM

To get a comprehensive view of the movement and the variation of intensity of the atmospheric waves, it is useful to look at a trough and ridge diagram (Hovmöller, 1949), which is a longitude-time chart of geopotential height taken along a certain latitude circle.

Figures 22 and 23 are the diagrams for the 500-mb and 1000-mb geopotential heights, respectively, for the zone between 35° and 45°N at intervals of 24 hr for the observed and the prediction in Experiment 3 over the 2-week period. Each value is obtained by averaging over 5° of long. and 10° of lat.

It has been noted by Hovmöller (1949) and Graham (1955) that the patterns in this type of diagram consist generally of two modes. One is the basic flow, which is characterized by the longitudinally quasi-stationary waves and is represented by the first three harmonics of a Fourier expansion series. The other is the superposed perturbation, which is characterized by the eastward-moving waves that progress at a speed of about 9° long. per day or less. Notice that the moving waves penetrate

into the stationary ridges, and always redevelop on the other side.

The wave motion in the smaller scale is complex. Almost two decades ago Charney and Eliassen (1949) made the first attempt at dynamical treatment of dispersive waves and demonstrated the prediction of 500-mb geopotential values 24 hr ahead. The behavior of these complex waves was computed with remarkable success.

Now let us turn to the results in the present study, i.e., see figures 22 and 23 (also figs. 87 and 88 in Appendix III for the 1966 case).

In the following, we discuss the results for 500 mb:

1) The agreement between the prediction and the observed is very good. The behavior of the *longwaves* (for instance, the ridge over the middle Pacific Ocean at 153°W on the initial day which moved slightly toward the west after the 7th day) was accurately predicted. The wave trains of *medium scale* (for instance, the waves over the Atlantic Ocean between 0° and 60°W around the 11th day) were also well simulated.

2) The "excessive westward propagation of the longwaves" discussed by Wolff (1958) and Cressman (1958) is not found in this prediction.

3) The speed of the moving troughs (for instance, 147°E on the initial day) in the computation is rather good. Even after 14 days, the error in location of the predicted trough was 10° to 15° long. Why is the wave speed predicted well
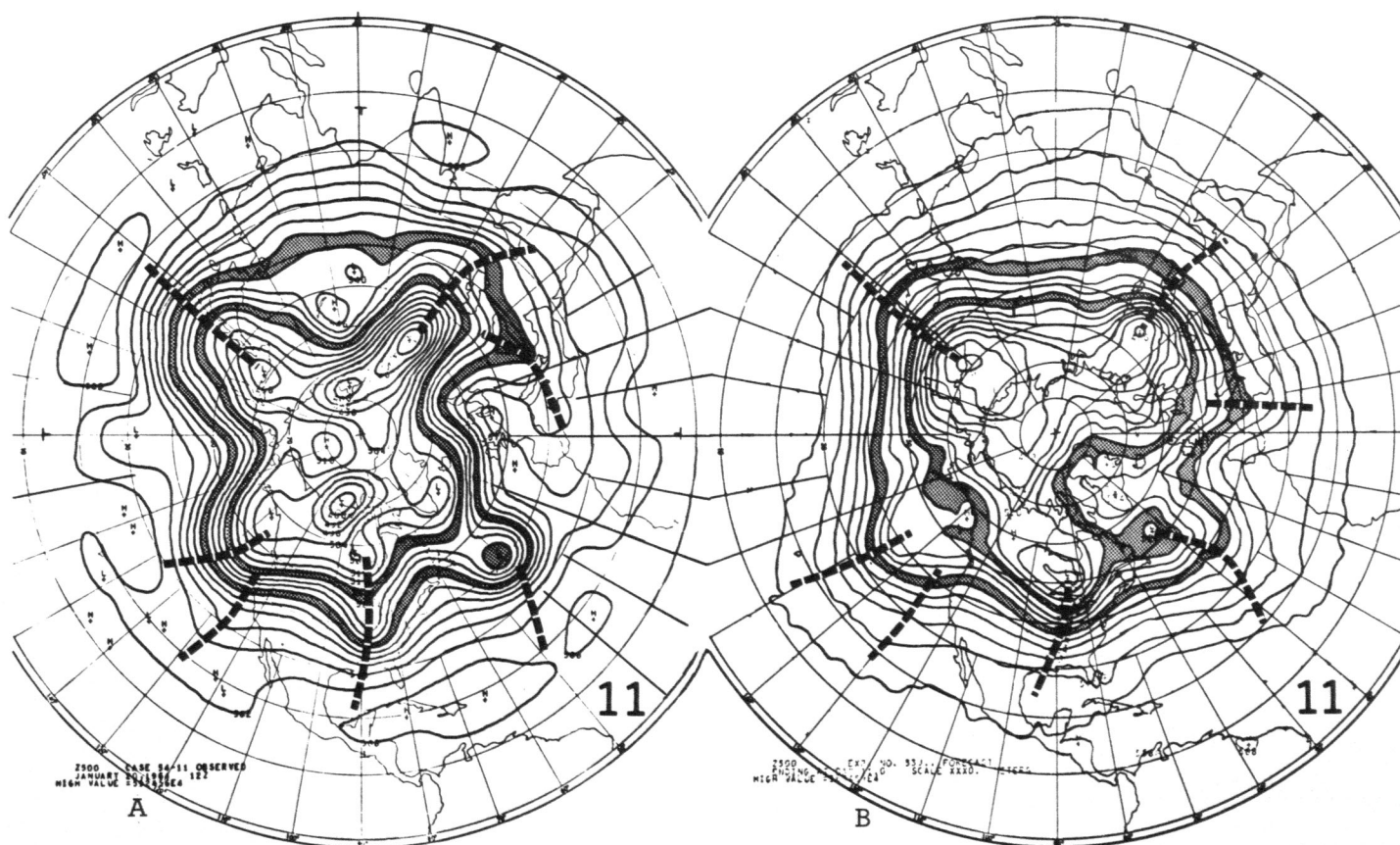
FIGURE 19.—The 500-mb geopotential height patterns for the 11th day. (A) the observed, and (B) the forecast in Experiment 3. The contour interval is 60 m. The belts of the geopotential height between 5220 and 5280 m and between 5460 and 5520 m are stippled to bring out the patterns. The trough lines are shown by dashed lines.

1000 MB
4 TH DAY
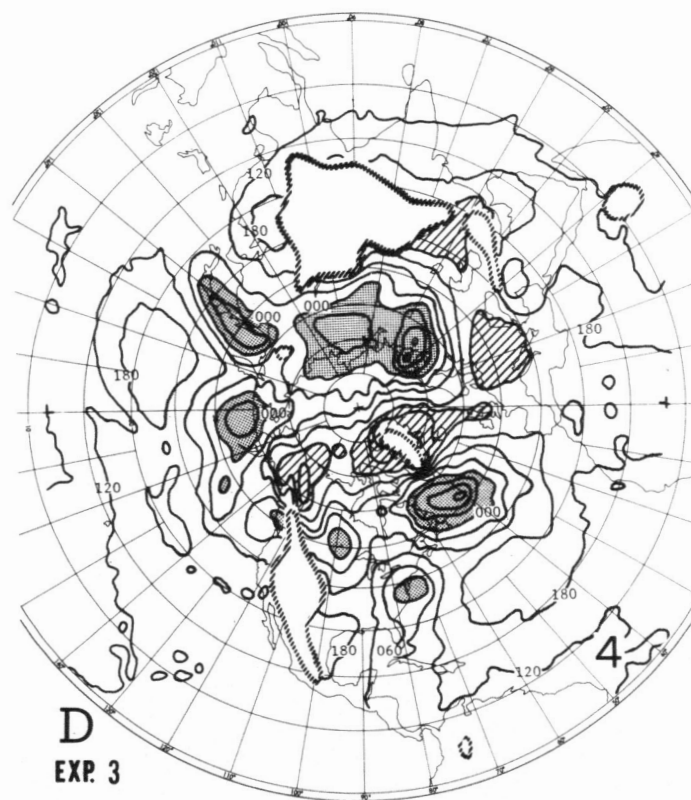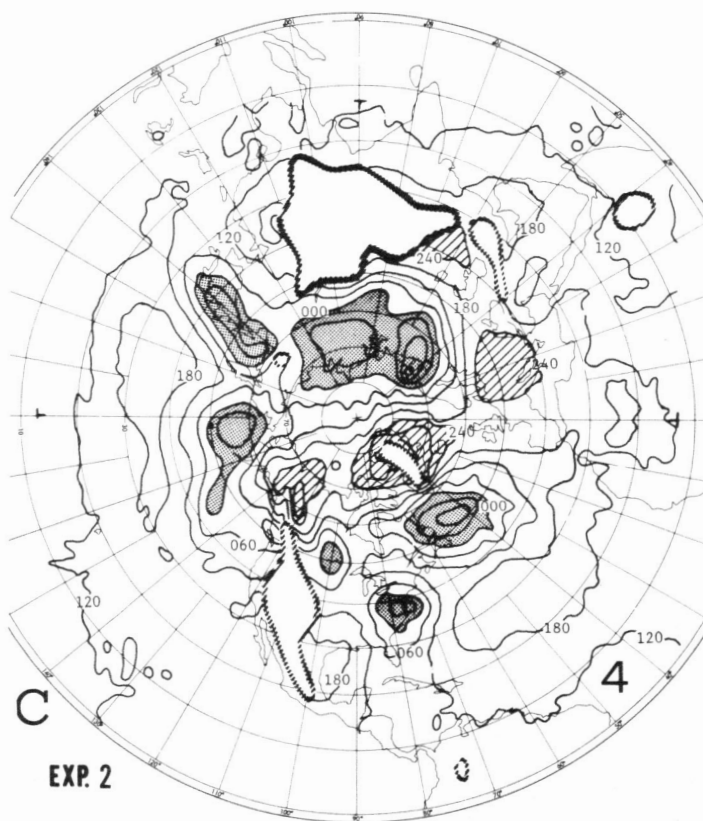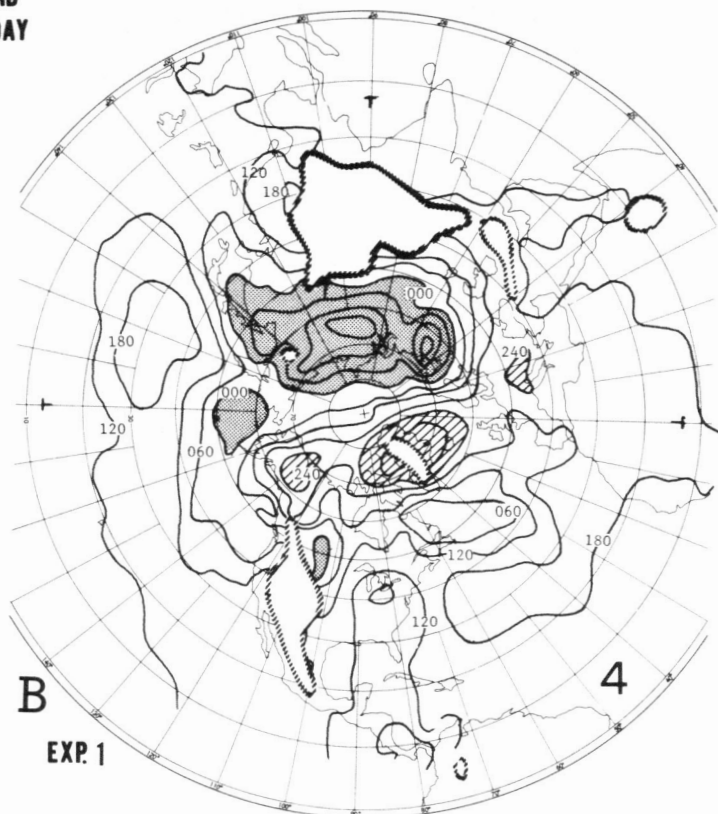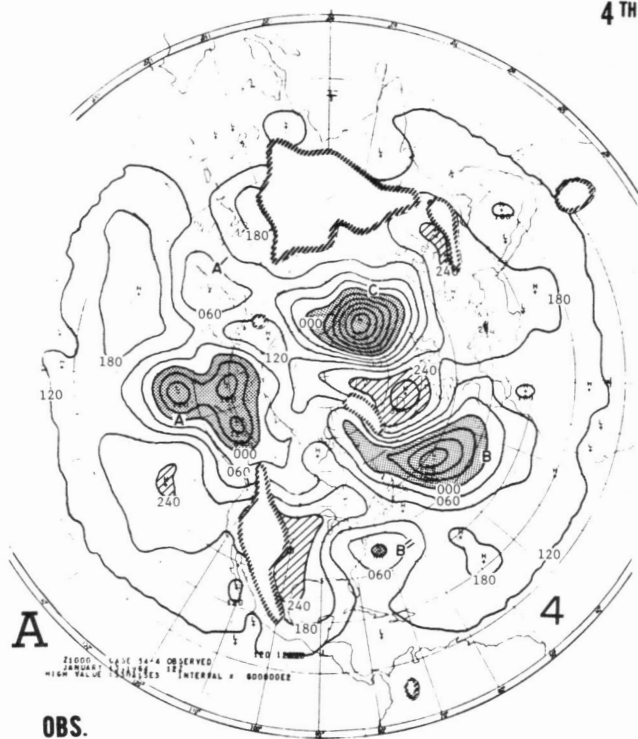
FIGURE 20.—The 1000-mb geopotential height for the 4th day. (A) the observed, (B) Experiment 1, (C) Experiment 2, and (D) Experiment 3.
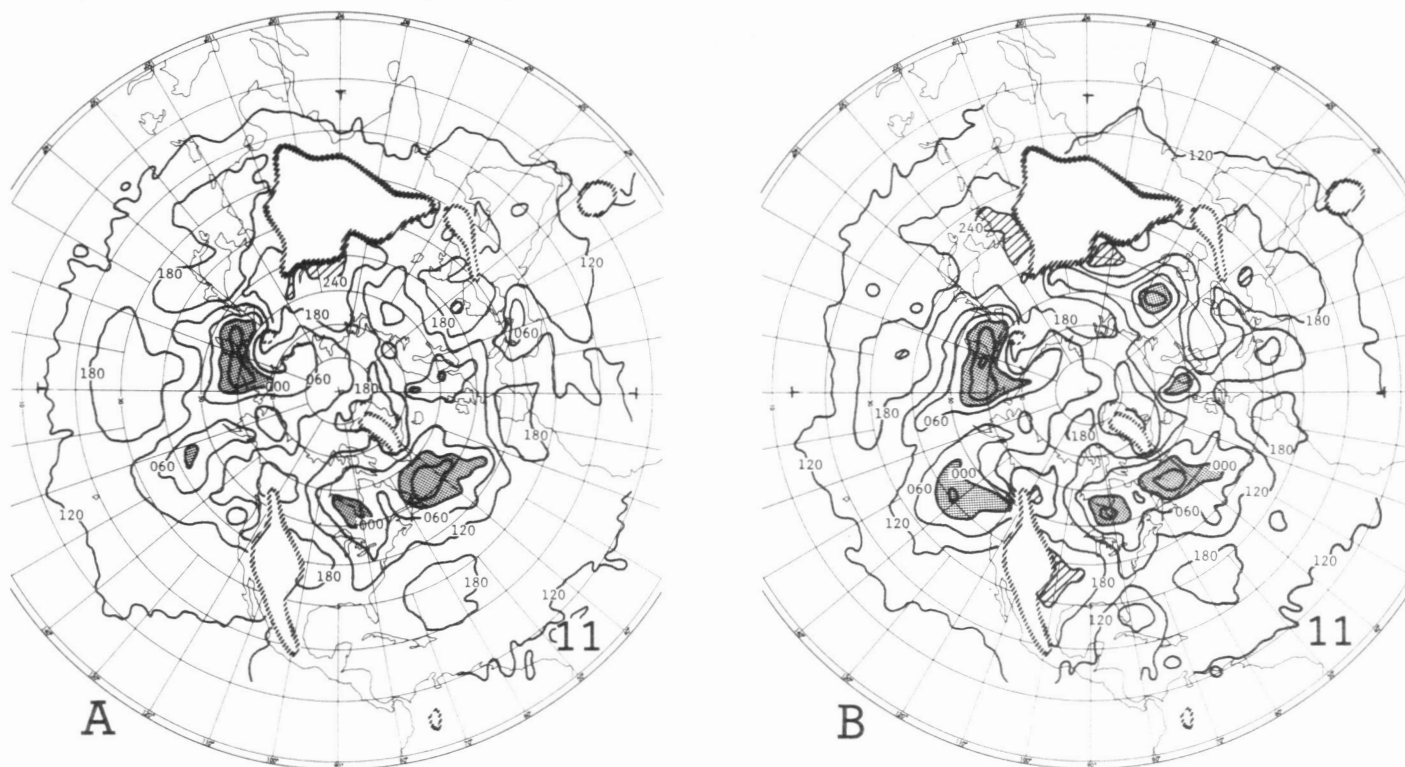
FIGURE 21.—The predicted 1000-mb geopotential height pattern for the 11th day for Experiment 2 (A) and Experiment 3 (B).

despite the fact that the zonal wind of the computation was appreciably stronger than it should be? One possibility is that, since the space truncation error causes a reduction in phase speed, its effect in this case was offset by the excessive advection. Another possibility is that the zonal wind at the *steering level*, probably level 5, did not deviate very much from the observed wind after all (see fig. 21). However, the 10° difference may cause the phase of synoptic-scale disturbances to be completely opposite, which is serious from a practical viewpoint.

4) It is interesting to note that, even if some trough (for instance, 63°E on the 4th day) or ridge (for instance, 128°W on the 6th day) in the computation did not agree with the observation at an early stage of the prediction, sometimes agreement is improved at a later time. This may be partly because we are looking at only the geopotential height at a certain latitude on a certain level. The disturbance might have just deviated from this latitude or level temporarily and returned later. However, we tend toward the notion that the geographically fixed heat sources and continentality are instrumental in the subsequent improvement in the computed state.

5) However, there is an obvious defect in the predicted pattern that is common to both the 1964 and 1966 cases. The quasi-stationary modes, or longwaves, are more dominant, while the eastward-moving components, the relatively shorter waves, are too small in amplitude.

7. VERIFICATION

To evaluate the prediction skill, we have computed standard deviations of error in geopotential heights and correlation coefficients with respect to the time changes in height. These measures are the same as those defined in the report of WMO's working group on numerical weather prediction (1965).

The standard deviation of error is the root-mean-square error of the forecast height with mean error removed. This quantity is usually compared with persistence, which refers to a hypothetical forecast of no change of the geopotential height from the initial time. The correlation coefficient is taken between the observed and the computed time change of the height from the initial time.

Let us denote z_{obs} as the observed height and z_{fcst} as the forecast height. Definitions of the various quantities are as follows:

Deviation of z:

$$X = z_{fcst} - z_{obs},$$

Mean of deviation:

$$X = \sum X/n,$$

where the summation is made for gridpoints north of 20°N and n is the number of gridpoints.
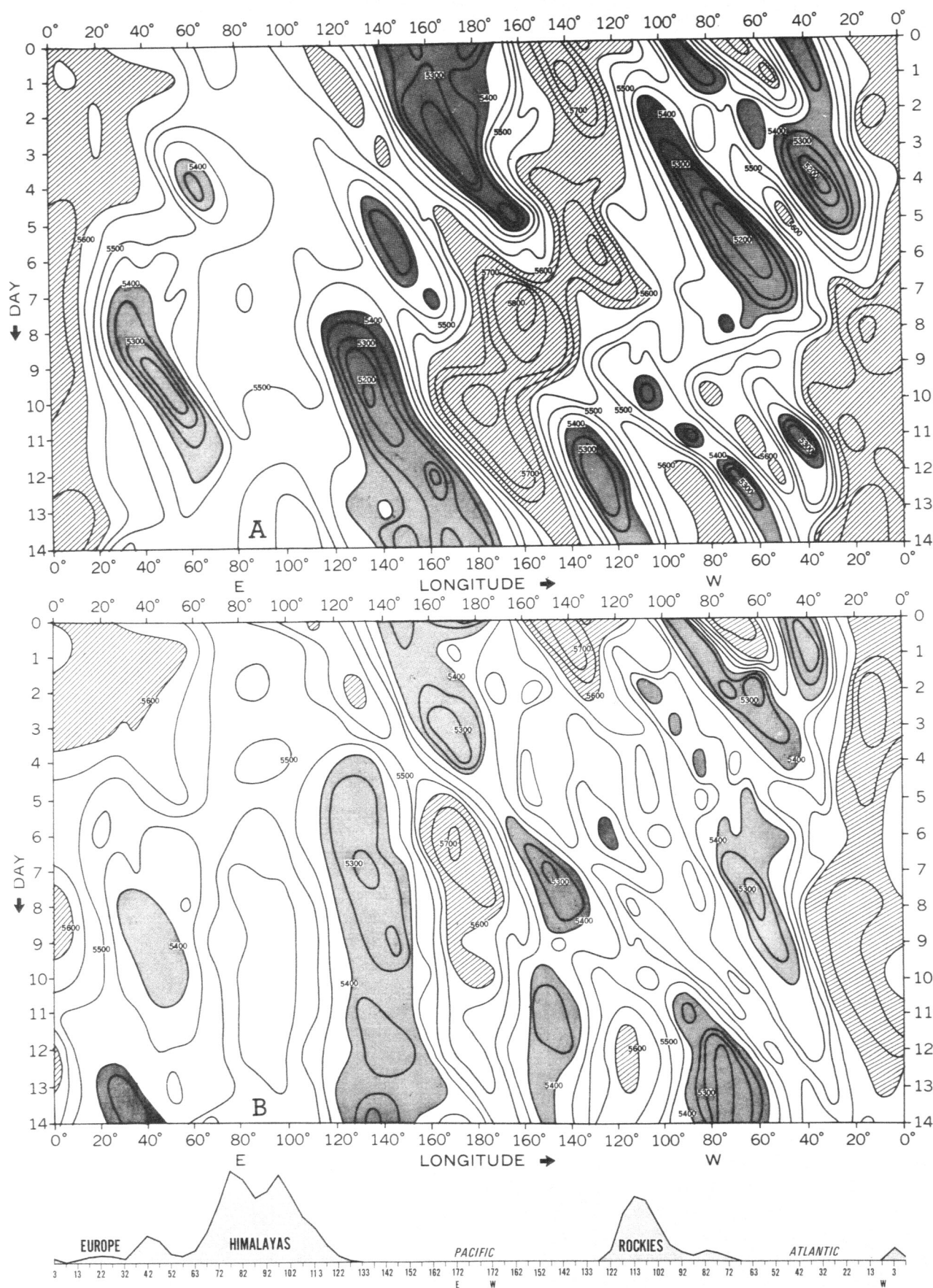
FIGURE 22.—Trough-and-ridge diagrams of the 500-mb level for the 1964 case. (A) the observed, and (B) the prediction of Experiment 3. The contours are for the 500-mb geopotential height in a zonal belt between 35° and 45°N. The units are decameters. The interval is 50 m. The ordinate is time in days, and the abscissa is longitude. The ridge areas with geopotential greater than 5600 m are hatched, and the trough areas with values lower than 5400 m are stippled.
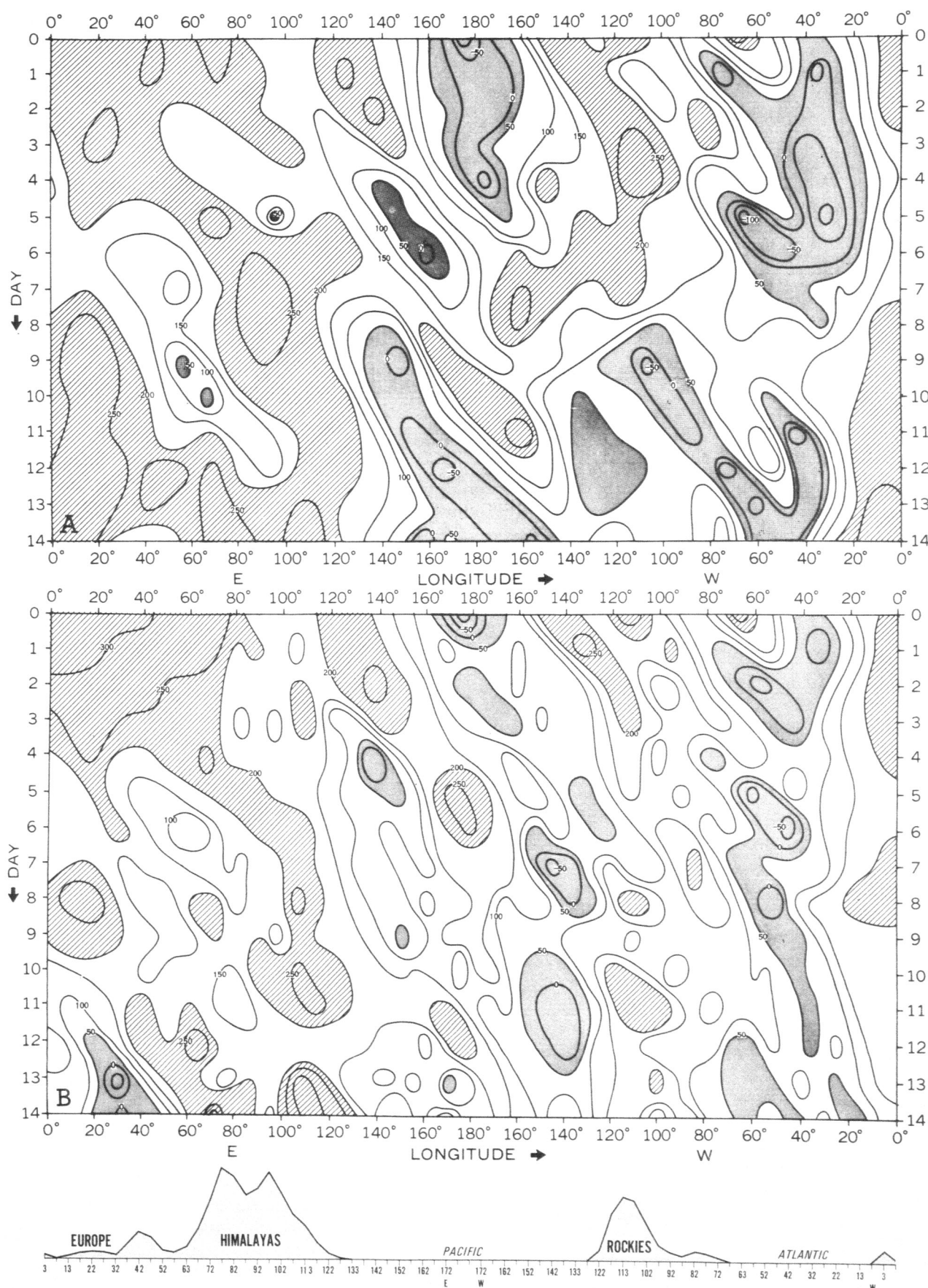
FIGURE 23.—Trough-and-ridge diagrams of the 1000-mb level for the 1964 case. (A) the observed, and (B) the prediction of Experiment 3. The contours are for the 1000-mb geopotential height in a zonal belt between 35° and 45°N. The units are meters. The contour interval is 50 m. The ordinate is time in days, and the abscissa is longitude. The anticyclone areas with geopotential values higher than 200 m are hatched, and the cyclone areas with values lower than 100 m are stippled.

Standard deviation:

$$\text{S.D.}(X) = \sqrt{\sum(X - \overline{X})^2/n}.$$

Denoting $z(t)$ the geopotential height for the day t and $z(0)$ that for the initial day, we have

Time change of the observed height:

$$Y_1(t) = z_{obs}(t) - z_{obs}(0),$$

Time change of the forecast height:

$$Y_2(t) = z_{fcst}(t) - z_{obs}(0),$$

Persistence:

$$\text{Persist.} = \sqrt{\sum(Y_1 - \overline{Y}_1)^2/n},$$

Correlation coefficient:

$$\text{Correl. coeff.} = \frac{\sum(Y_1 - \overline{Y}_1)(Y_2 - \overline{Y}_2)/n}{\text{S.D.}(Y_1) \cdot \text{S.D.}(Y_2)}.$$

If the entire Northern Hemisphere is taken instead of an area north of 20°N as the verification domain, the *standard deviation* will be decreased because of the small variability of the geopotential in the Tropics, and the *correlation coefficient* will be lower compared with that for the domain north of 20°N because of the inclusion of the uncorrelated region.

Figure 24 shows how the standard deviations for 1000-, 500-, and 50-mb geopotential heights vary with time. In the same figure, the values for *persistence* are also plotted, which is a measure of the natural variability of the geopotential height. The standard deviation between Experiments 2 and 3 is shown for comparison.

Now, looking at these figures together with those for the 1966 case in Appendix III, we note that the standard deviation at 500 and 50 mb for Experiments 2 and 3 are smaller than the persistence until about 7 days, while the standard deviation at 1000 mb is as large as that of the persistence even at the 4th day. Literally interpreted, this could mean that the forecast of 1000-mb geopotential height is completely unacceptable at the 4th day.

But it is readily seen by visual inspection of the synoptic maps that the 1000-mb forecast at the 4th day is still similar to the observed. Presumably the standard deviation of error is a very severe measure. A judgment of prediction skill based on this quantity requires some caution. As a matter of fact, even the induced inertia-gravitational component, which appears sometimes as *wiggling* superposed on the basic geopotential field, increases the value of the standard deviation.

In this respect, the correlation coefficient seems to be less sensitive. Figure 25 gives the correlation coefficients for Experiments 1, 2, and 3.

We note that the values of correlation coefficient gradually decrease with time (except for the 1000-mb level in the 1966 case, which was lower at 8 days, see fig. 90). At the 14th day, the values are 0.4, 0.5, and 0.8 at the

1000-, 500-, and 50-mb levels. In both cases, the 1000-mb correlation coefficient is lowest. It is generally high for the 500-mb level. The coefficient for the 50-mb level in the 1964 case is persistently high, but it is lower in the 1966 case. In the latter case, a breakdown of the polar night vortex occurred during the forecast period, making the prediction more difficult. From the standpoint of the correlation coefficient, the results of Experiments 2 and 3 are quite similar even at the 11th day.

It is remarked, however, that the forecast changes corresponding to a return to normal may yield values significantly greater than zero for this type of correlation coefficient. Other kinds of verification scores are suggested and will be computed in the near future. It seems that no single verification score is universally accepted.

8. PRECIPITATION FORECAST FOR THE UNITED STATES

We now turn to the results of the precipitation forecast for middle latitudes. For a detailed verification we took the United States and the southern part of Canada, where high density data were easily accessible. Data of approximately 3,000 rain-gage stations were used.

The observed amounts of precipitation at these stations were averaged over the unit domain surrounding each gridpoint. All the results of the time evolution of forecast condensation for Experiment 3 of the 1964 case and the observed rainfall are contained in figure 53 of Appendix II. Figure 26 shows an example of the condensation patterns. It is the 2-day accumulation of the observed rainfall and the predicted condensation for Experiments 1, 2, and 3 for the 3d and 4th days.

In this figure, we note the following points:

1) The computed condensation in each experiment is diffused over a wider area than in the observed pattern. This tendency is more conspicuous for Experiment 3 than for the other experiments. The computed quantity is condensation, and it does not really correspond to precipitation. For instance, evaporation from falling droplets was ignored.

2) Earlier dynamical prediction studies of precipitation have usually concluded that the computed amounts were appreciably less than the observed amounts. This is not true of the present experiments, especially those in Experiments 2 and 3 for the middle latitudes. The reasons are that the primitive equations are used with a high resolution grid, the moist convection is accounted for, the feedback of heat released by condensation into the atmosphere is allowed, the effects of evaporation from the surface and radiation are included, and in Experiment 3, the condensation criterion is reduced to 80%.

3) In the observed rainfall patterns the area in the Northwest is limited to a small area near the coast. The computed area, however, spreads farther inland. It was concluded by Smagorinsky, Strickler, et al. (1965) that the mountain effect in the model is distorted by smoothing. Another factor may be that the surface drag coefficient
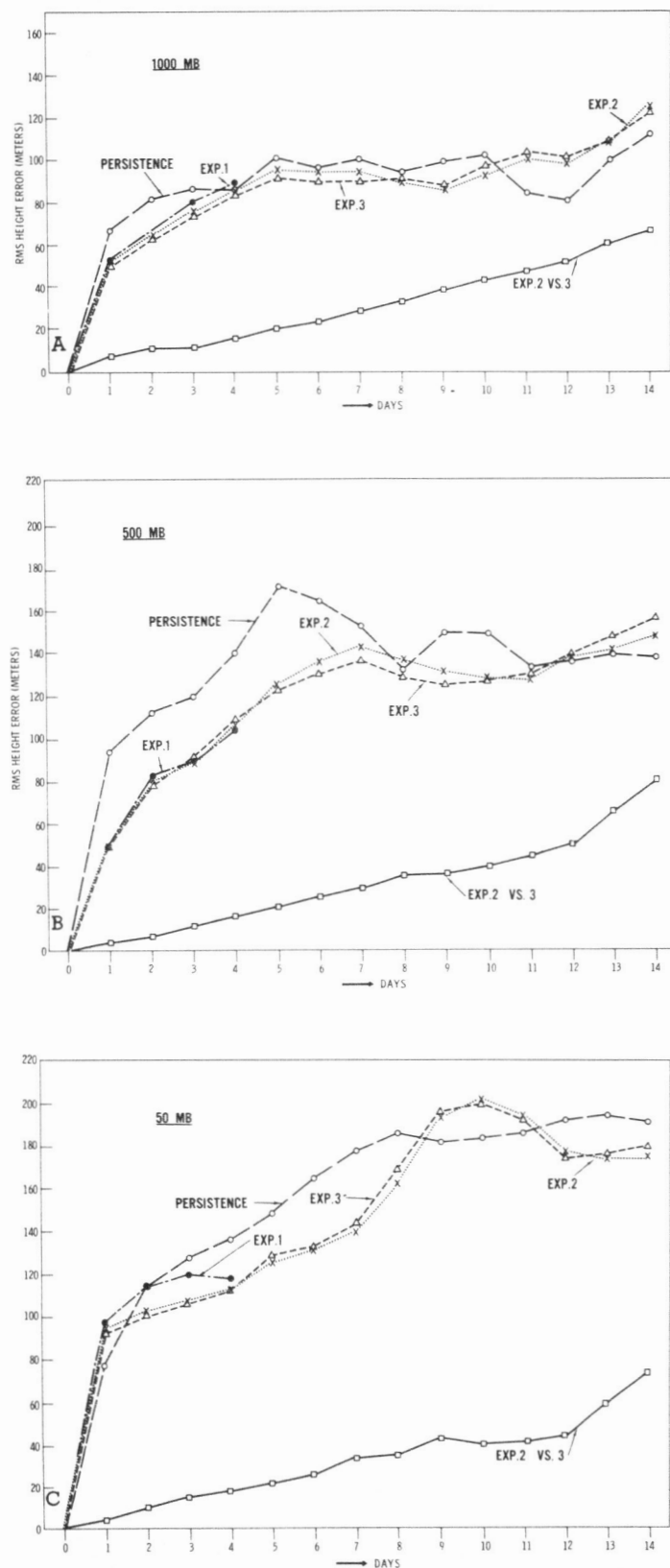
FIGURE 24.—Standard deviation of error in geopotential height between the observed and the predicted for the domain north of 20°N in units of meters. (A) the 1000-mb level, (B) 500-mb, and (C) 50-mb. The errors for Experiment 1, Experiment 2, Experiment 3, and a persistence forecast are shown as marked. The difference between Experiments 2 and 3 is also shown. The abscissa is time in days.

over land is too small and accordingly the air in the lower atmosphere tends to move inland too easily compared with reality (see the wind intensity at level 9 in fig. 12).

4) The patterns of the computed condensation in the middle latitudes do not differ much from one experiment to another during the 2-week forecast. Therefore, it is difficult to choose one experiment as superior in terms of the precipitation prediction.

Verification scores for the occurrence of precipitation greater than 0.10 in. were computed for both cases by D. L. Gilman, Extended Forecast Division, NMC, and were reported by Namias (1968) in his Harry Wexler Memorial Lecture. The scores were computed for 100 stations in the United States.

Figure 27 shows the average for the two cases. It appears that the skill was positive until about the 9th day. A random forecast should give an expected skill score of zero. Refer to Namias (1968) for further details and for the individual scores.

The scores were obtained by the usual skill score formula,

$$S = \frac{C - X}{T - X}$$

where $S=$ skill score; $C=$ number of stations with correct forecast, occurrence, or nonoccurrence; where 0.10 in. is the criterion for the forecast of occurrence (the 0.10-in. criterion was adopted arbitrarily and tentatively for the study); $X=$ number of stations at which correct forecast is expected by chance; $T=$ total number of stations.

In computing X, a special weighting was used to allow for the variable likelihood of precipitation at the stations considered. Derivation of this formula will be given in a forthcoming paper by Gilman (1968).

9. HEMISPHERIC AND ZONAL MEANS

Figures 28 and 29 show the kinetic energy integrated over the whole hemisphere, i.e.,

$$\int_0^\infty \iint \rho \tfrac{1}{2}(u^2 + v^2) dx \, dy \, dz,$$

and the internal plus potential energy, i.e.,

$$\int_0^\infty \iint (\rho C_v T + \rho g z) dx \, dy \, dz,$$

where the notation is conventional. As is seen, the kinetic energy level is highest in Experiment 3, and that in Experiment 2 is second highest. This is because the heat released by condensation is largest in Experiment 3, and it contributed to the increase of kinetic energy. The kinetic energy in Experiment 1 decreases very rapidly with time due to the lack of condensation in the Tropics, which, in turn, comes from the omission of radiation. The computed kinetic energies do not coincide closely
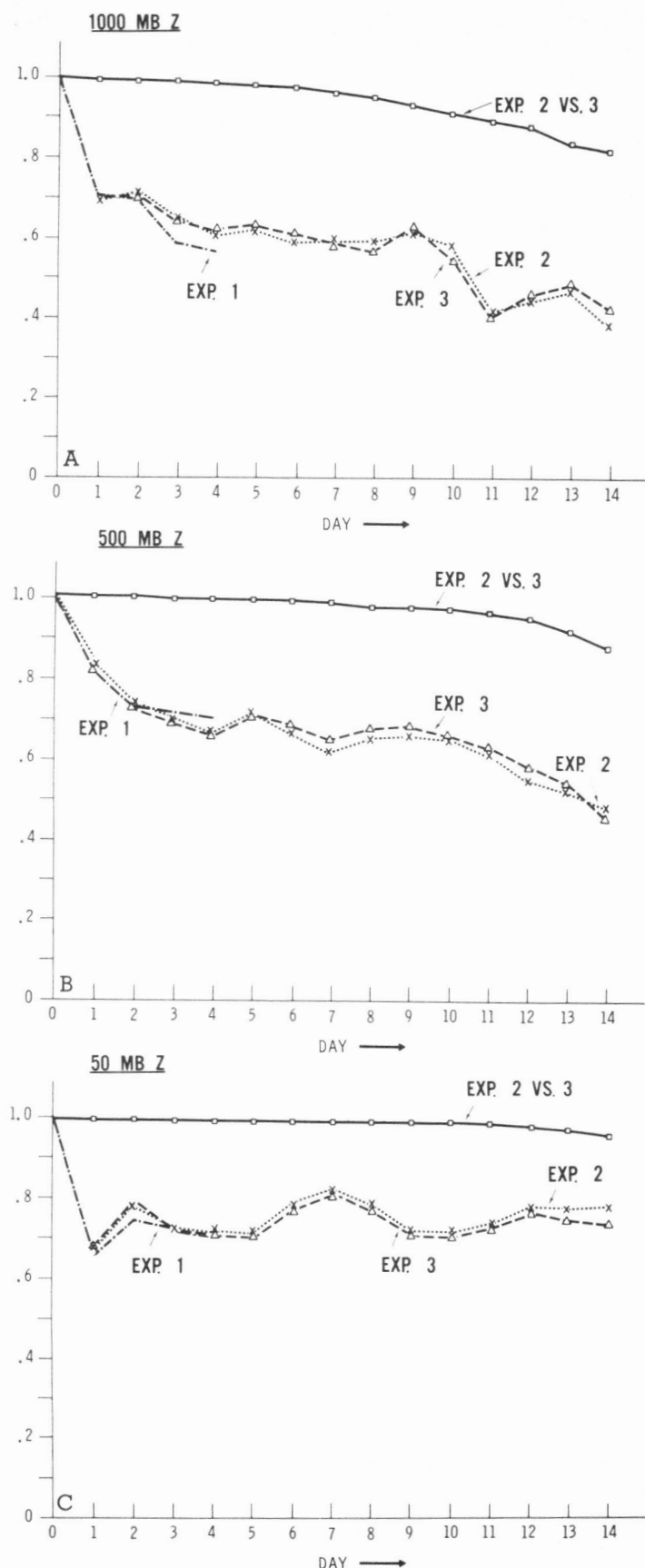
FIGURE 25.—Correlation coefficient between the observed and the forecast pattern of the change in geopotential height from the initial time for the domain north of 20°N. (A) the 1000-mb level, (B) 500-mb, and (C) 50-mb. The comparisons between Experiments 2 and 3 are also shown.

with the observed. Inertia-gravitational oscillations are observed in all three cases, and their variations with time are very similar in each case. The amplitude is large at the beginning of the forecast, probably due to imperfection in the initialization. They gradually fade with time, though the wiggling increases.

A comparison of the potential plus internal energy curves (fig. 29) reflects the temperature forecast. In Experiments 2 and 3, the potential plus internal energies are lower than the actual, since the computed atmosphere was too cold.

One important statistic in the atmospheric circulation is the *eddy* kinetic energy. In the general circulation study (Manabe et al., 1965), it was concluded that the eddy kinetic energy is appreciably smaller than the observed mean values. At that time, however, the general circulation model excluded orography and continentality. It was thought that by accounting for these effects one might correct the deficiency. In the present study, both effects have been included. Furthermore, the effective viscosity is smaller because of the smaller grid size.

Before looking at the eddy kinetic energy, let us turn first to the zonal kinetic energy. Figure 30 is the time variation of the vertical distribution of the hemispherically averaged zonal kinetic energy in Experiment 2, i.e.,

$$K_z = \frac{1}{2}\left(\bar{u}^2 + \bar{v}^2\right),$$

where the bar is the zonal average. The computed zonal kinetic energy appears to grow gradually in the troposphere, and it exceeds the observed values considerably at levels 3 and 4. This point will be discussed later.

Figure 31 is the eddy kinetic energy in Experiment 2, i.e.,

$$K_E = \frac{1}{2}\left(\overline{u'^2} + \overline{v'^2}\right),$$

where $u' = u - \bar{u}$, and $v' = v - \bar{v}$. The computed eddy kinetic energy decreases as the computation goes on, and it is much smaller than the observed value in the troposphere. So, despite the inclusion of the mountains and the land-sea contrast, a reasonable intensity of eddy kinetic energy has not evolved in this model. This feature may also be easily noticed in the synoptic patterns of geopotential height, as was shown earlier.

This characteristic may be measured in another form, i.e., the ratio of the zonal to the eddy kinetic energies, K_z/K_E at level 3 (fig. 32). The observed value of the ratio in the 1964 case ranges between 1.0 and 1.5, which is probably larger than in a normal year. On the other hand, the computed value is definitely larger than the observed, and it increases with time. In Manabe et al. (1965), this ratio was 3.5 at level 3. In connection with this problem, the following should be mentioned. The "moist" model produces much less eddy kinetic energy than the "dry" model does in the middle latitudes. This is probably because the role of water vapor in general, except in the Tropics, is to moderate the large-scale thermal contrast
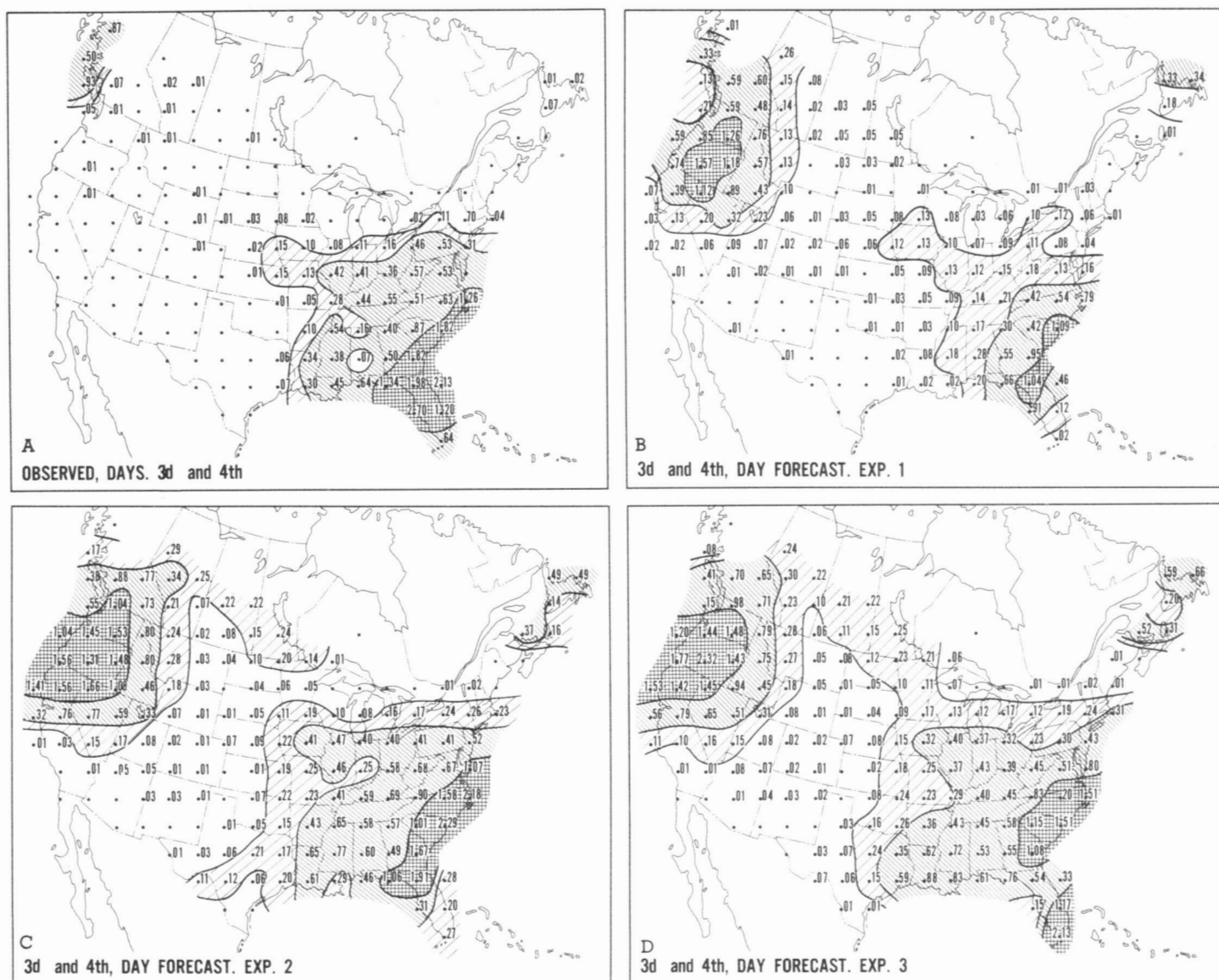
FIGURE 26.—Comparison of the observed precipitation and the predicted precipitation for the United States and a part of Canada. The examples are 2-day accumulations of precipitation for the 3d and 4th days in inches. The contours are at 0.1, 0.3, and 1.0 in. (A) the observed, (B) Experiment 1, (C) Experiment 2, and (D) Experiment 3.

(as shown by computation of the latitudinal temperature gradient in the moist model and the dry model (Manabe et al., 1965)).

It is likely that the deficiency in *eddy* kinetic energy might be due to the effective Karman constant governing the *internal viscosity* that we have employed. We made some exploratory experiments on this problem. A tentative conclusion is that a reduced Karman constant does improve the result, though it does not completely solve the problem.

Let us now turn to the zonal averages of the zonal wind and the 850-mb and 50-mb temperatures. It is perhaps useful to compare the three experiments. First, figure 33 shows the observed and the computed zonal wind at level 6, $p/p_* = 0.664$, and the *zonal index*.

In the general circulation study (Manabe et al., 1965), an important defect was that the center of the computed

westerlies was located at latitudes as low as 25°N in the moist model (as compared to 37°N in the dry model). This was a point of concern in the present study. Figure 33, however, indicates no such tendency for the jet axis to be shifted to the south during this 2-week period. The 1966 case (Experiment 61J) was extended for 3 weeks and the conclusion is the same. Conceivably, the inclusion of mountains and land-sea contrast is mainly responsible for the improvement. (Manabe, 1965, has mentioned that if the horizontal resolution is below $N=20$ the grid size has a large influence on the position of the jet stream.)

The agreement between the observed zonal wind and that for Experiments 2 and 3 is not particularly good. The axis of westerlies at 33°N at the beginning moves northward to about 45°N on the 7th day, and then is displaced southward. The north branch of westerlies at 69°N is present until the 3d day and then disappears. The weakest westerlies at 51°N moves northward and then become easterlies at 6, 7, and 8 days. These features were correctly

AVERAGE SKILL OF PRECIPITATION FORECAST
53J AND 61J
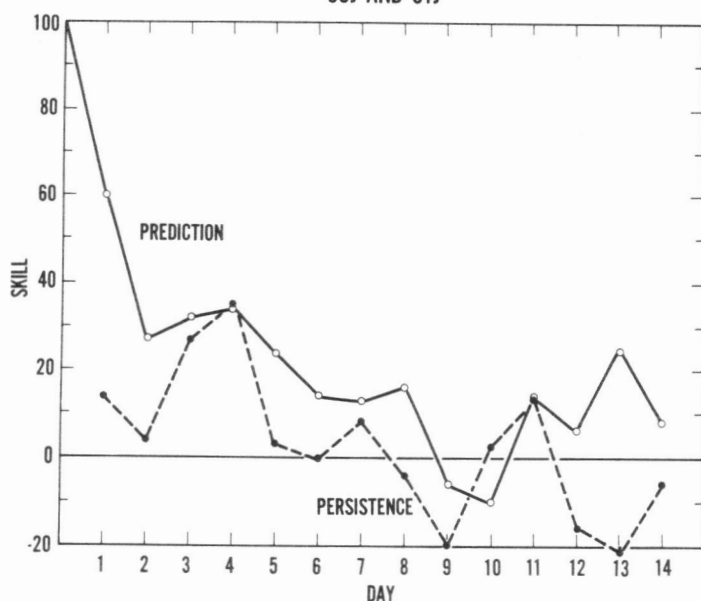
FIGURE 27.—Skill score for each day for the precipitation forecast for the United States and part of Canada. The average is shown for the 1964 and 1966 cases. (Solid line) forecast and (dashed line) persistence (after D. L. Gilman, 1968).

computed but the splitting of the westerlies into two branches on the 11th day was not successfully forecast. The same defect is noticed in the 1966 case (see fig. 69 in Appendix III).

Figure 34 is the time evolution of the zonally averaged temperature at 850 mb. It may be seen that the temperature in Experiment 2 is lower than the observed at high latitudes, but that the deficiency is not as great in Experiment 3. This improvement was achieved, as was mentioned earlier, by including the effect of sea ice, and possibly by the 80% condensation criterion.

Figure 35 is the zonally averaged temperature at 50 mb. It is very clear that the well-known warmer region in the middle latitudes around 51°N gradually disappears as the computation proceeds. Associated with it, the zonal wind in the lower stratosphere weakened, and furthermore the region of westerlies extended southward. Also, the stratospheric westerlies tend to connect with the tropospheric westerlies. Because of these defects, the stratosphere in the present forecast looks different from the actual as the integration goes on.

10. STATISTICAL QUANTITIES

When characterizing the atmospheric structure and motion on a hemispheric and climatological scale, certain
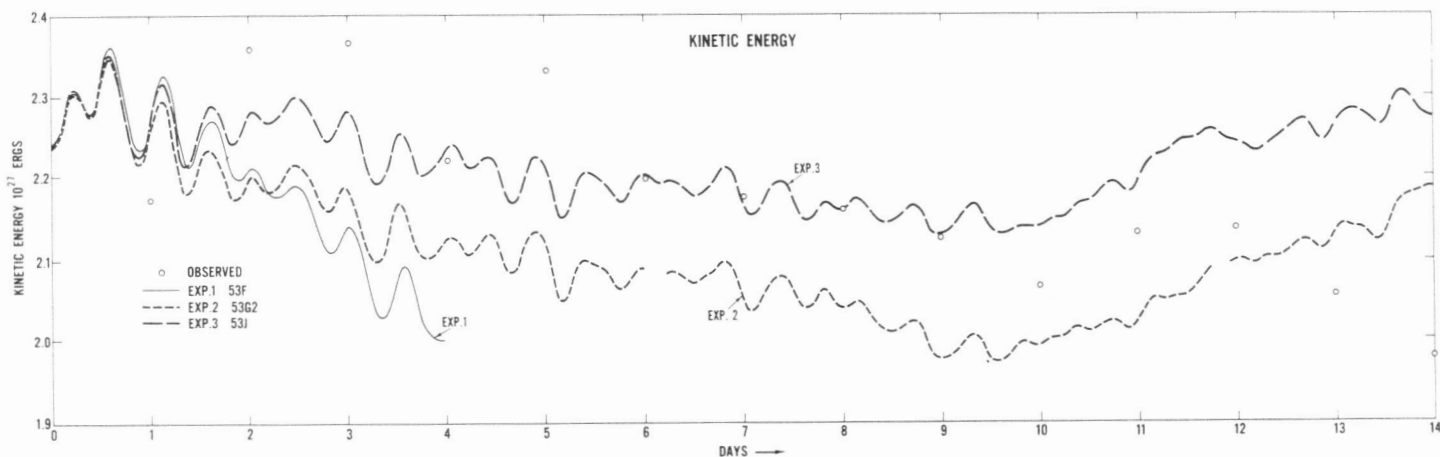
KINETIC ENERGY

FIGURE 28.—Time variation of kinetic energy integrated over the whole hemisphere for Experiments 1, 2, and 3 in units of 10^{27} ergs. The observed values are shown by small circles.
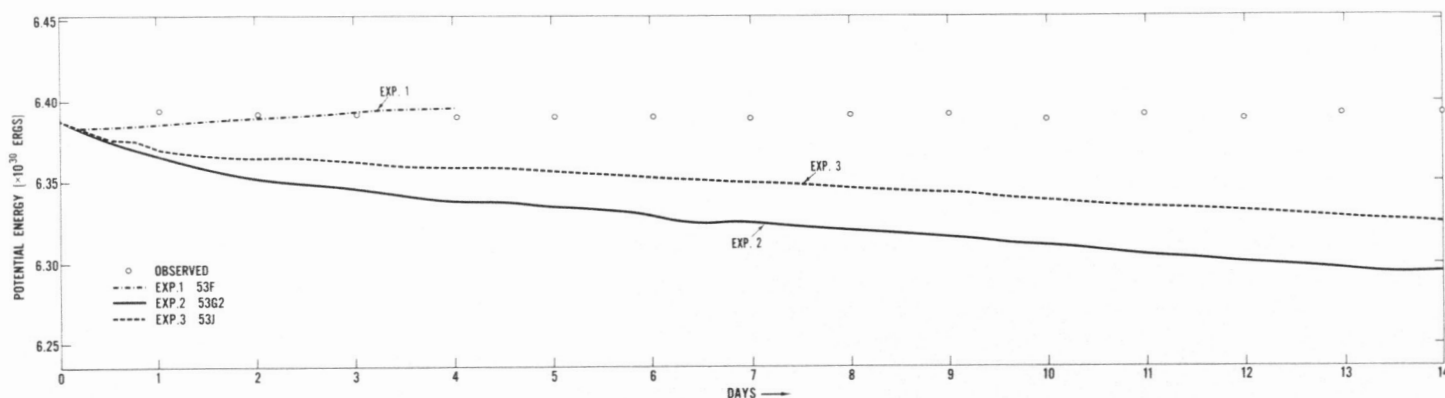
FIGURE 29.—Time variation of the internal plus potential energy integrated over the whole hemisphere for Experiments 1, 2, and 3 in units of 10^{30} ergs. The observed values are shown by small open circles.

KZON IN $10^7 CM^2/SEC^2$, 53G2
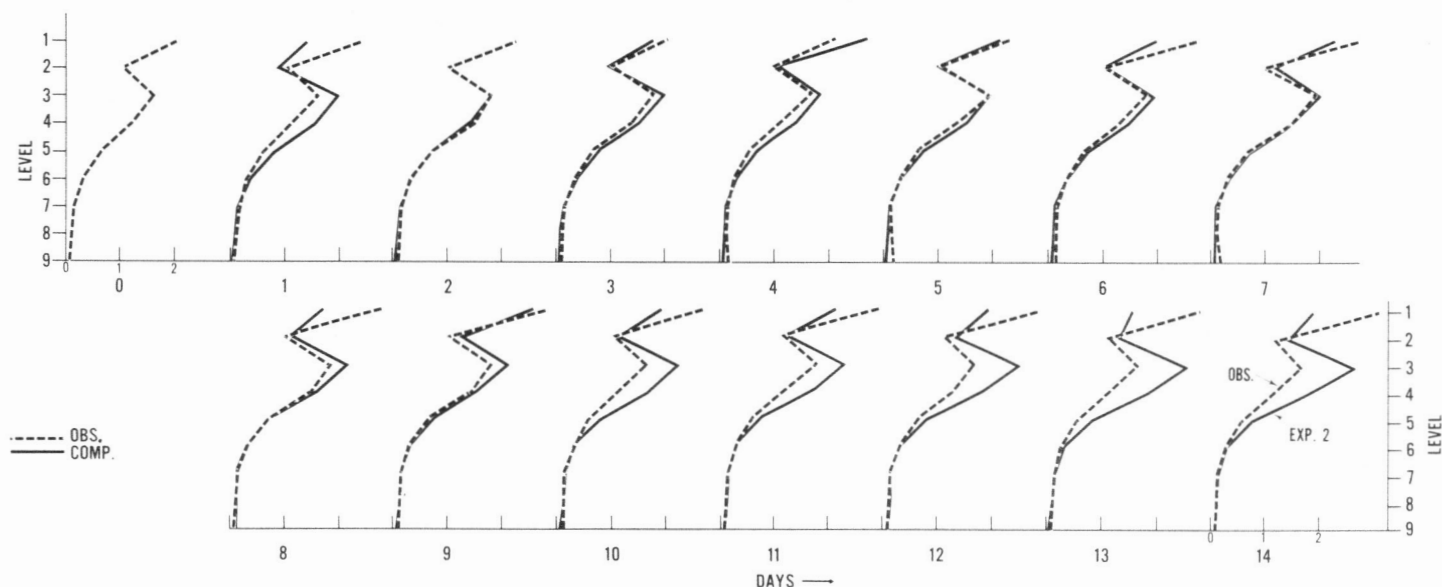
FIGURE 30.—The vertical distribution of the zonal kinetic energy in Experiment 2, which is hemispherically averaged, in units of 10^7 cm²/sec². The solid and dashed curves are the computed and observed results, respectively.

KEDD IN $10^7 CM^2/SEC^2$, 53G2
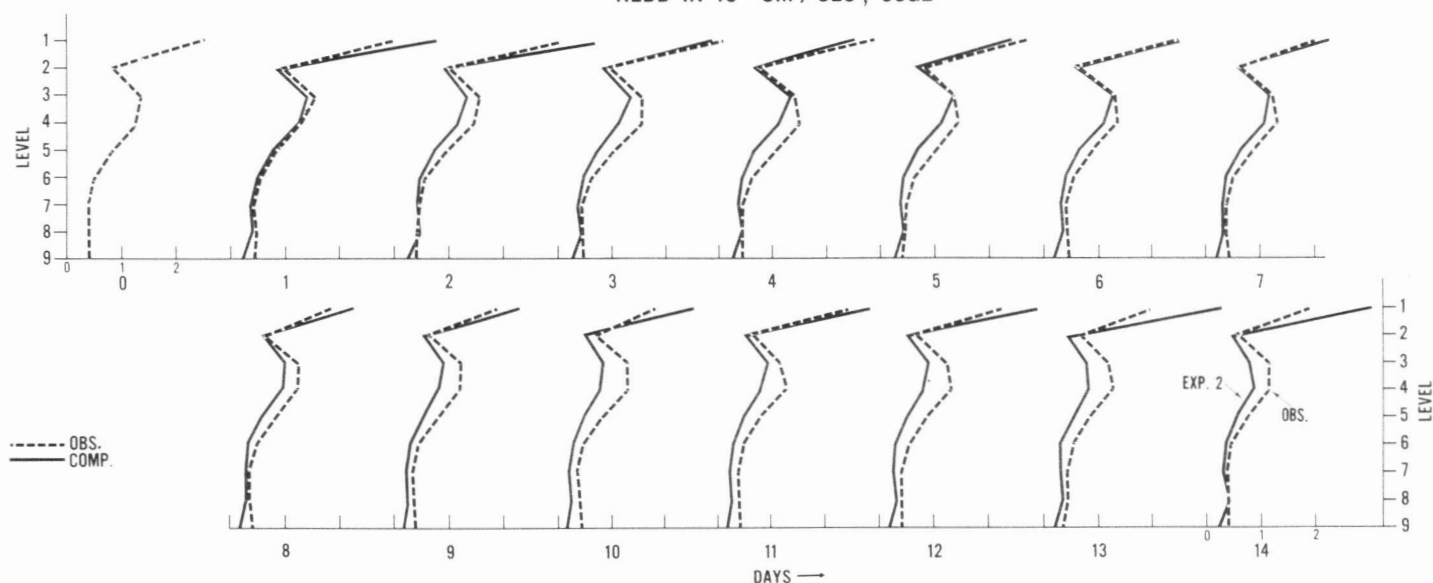
FIGURE 31.—The vertical distribution of the eddy kinetic energy in Experiment 2, which is hemispherically averaged, in units of 10^7 cm²/sec². The solid and dashed curves are the computed and obesrved results, respectively.

statistical quantities are often used in general circulation studies. These quantities are computed by taking time averages for a certain span of time and also by taking zonal averages around the hemisphere. They are computed for the basic meteorological variables, wind, temperature, and humidity, and also for derived quantities such as the angular momentum and the kinetic and potential energies.

In the work by Smagorinsky, Manabe, and Holloway (1965) and Manabe et al. (1965), these statistical quantities

were computed for each simulation and were compared with independently computed results for the real atmosphere, i.e., the climatology. These comparisons were essential in interpreting the results. Although the present experiments are not general circulation studies, these statistical quantities were computed for the prediction results (averaged from 3 to 14 days) as well as for the observed data (averaged from 0 to 14 days). This permits one to detect systematic degeneracies in the long-term behavior of the forecast.

To make this possible each of the observed 14 days has been subjected to initialization processing. The three-dimensional wind velocity was obtained by solving the so-called "balance equation" and the "ω-equation" (nonadiabatic) using the observed geopotential height and temperature for the 2-week period. The analysis was valid only north of 20°N.

As usual, the zonal mean quantities are expressed with the bar, i.e.,

$$\overline{X} = \int_0^{2\pi} X d\lambda / 2\pi,$$

where X is an arbitrary quantity and λ is longitude. Eddy quantities are expressed as primes, i.e., $X' = x - \overline{X}$.

In the following meridional sections, the ordinate is the vertical coordinate at equal geometrical heights in units of kilometers, and the abscissa is latitude at 6° intervals. The tropopause is shown by the dashed curve. In January the arctic tropopause is indefinite. The tropical tropopause in these charts is too high compared to climatological values which are normally at about the 100-mb level. It is because of the low resolution in the vertical in these charts (see the temperature distribution in fig. 54). The two columns at the right-hand side of the diagram show (*left*) the horizontal average of the quantity for the

FIGURE 32.—Time variation of the ratio of zonal to eddy kinetic energy at level 3 for Experiments 1, 2, and 3.
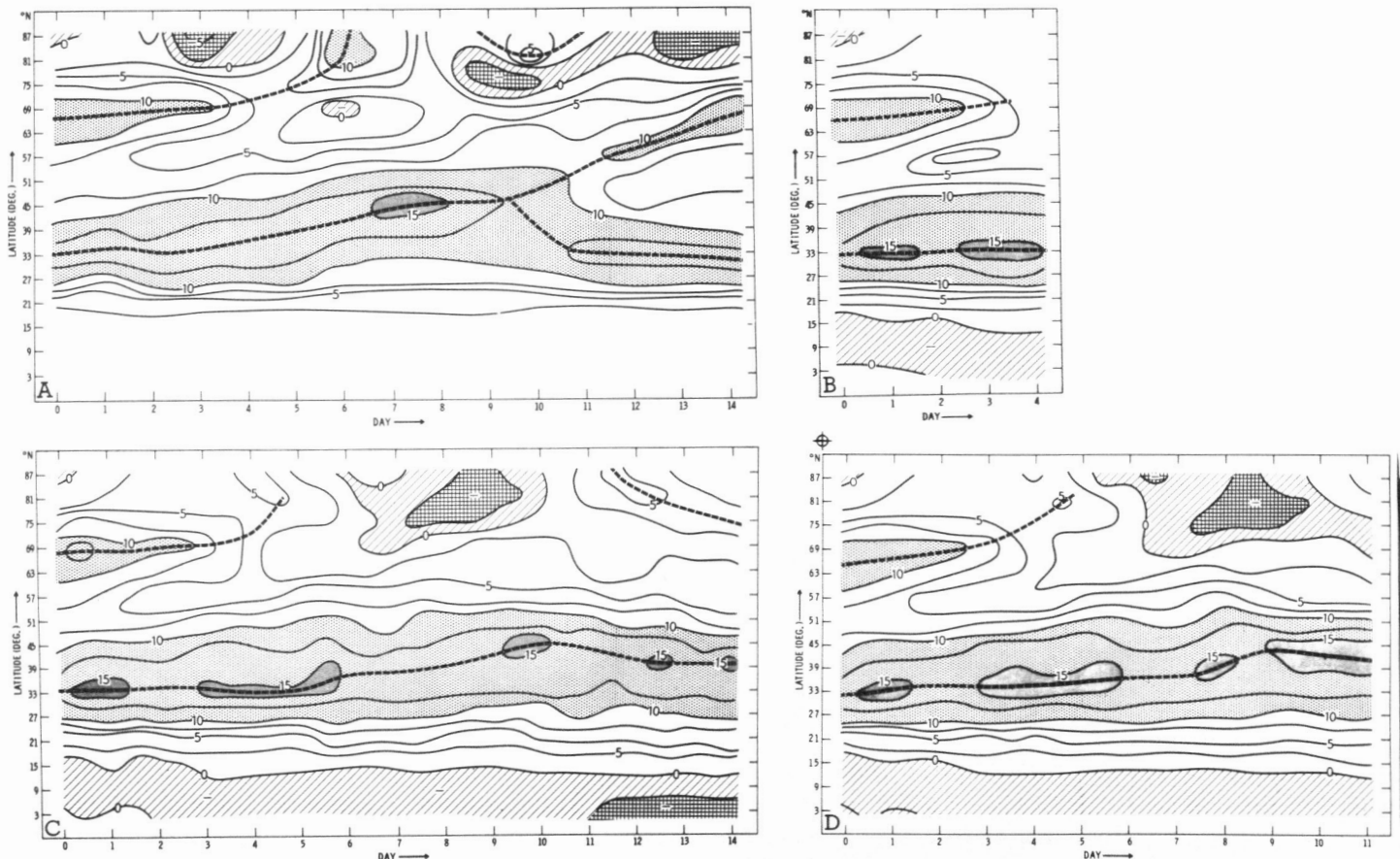
FIGURE 33.—The zonal average of zonal wind at level 6 in units of meters per second. The ordinate is latitude, and the abscissa is time. (A) the observed, (B) Experiment 1, (C) Experiment 2, and (D) Experiment 3. The westerlies are indicated by plus, and the easterlies by minus. The maxima of the westerlies are connected by the thick dashed lines.
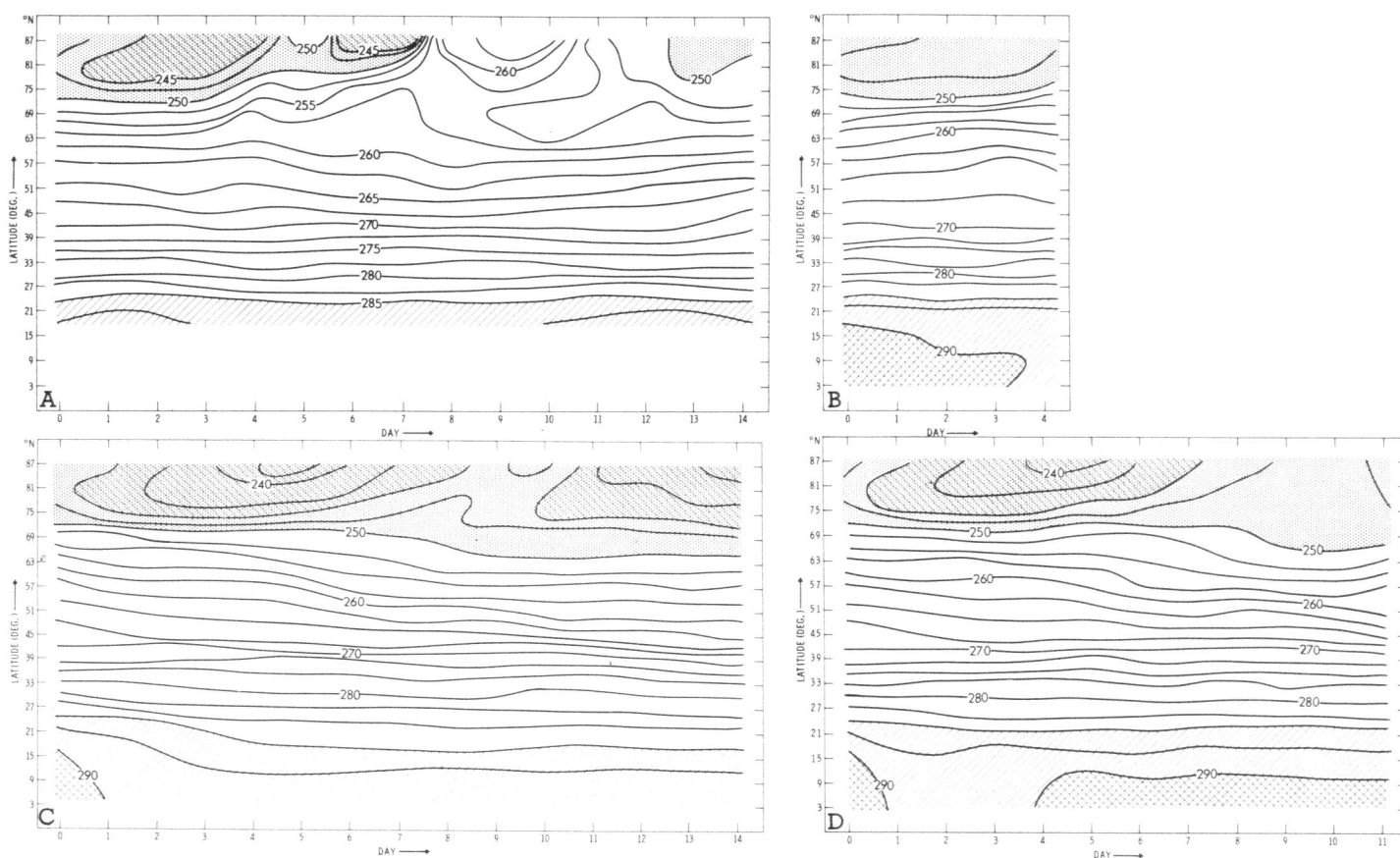
FIGURE 34.—The zonal average of temperature at the 850-mb level in units of °K. The ordinate is latitude, and the abscissa is time. (A) the observed, (B) Experiment 1, (C) Experiment 2, and (D) Experiment 3. The area where temperature is higher than 285°K is hatched, and that where it is lower than 250°K is stippled.

whole Northern Hemisphere and (*right*) the horizontal average for the area north of 20°N. For observed charts only the second column is included.

THE ZONAL WIND

In the observed data there are two marked centers of westerlies, i.e., the tropopause jet and the polar-night jet in midstratosphere. (See fig. 36.) In Experiments 2 and 3, these two areas of westerlies tend to join and the latitudinal splitting of the tropospheric westerlies disappears (see also fig. 71 in Appendix III). The tendency for the westerlies to join is closely related to the erroneous cooling of the midlatitude zone in the lower stratosphere, and it is also related to the southward extension of the stratospheric westerlies. Indications from other studies (Manabe and Hunt, 1968) suggest that it is mainly due to vertical truncation error and that higher vertical resolution is needed to remedy it.

The computed tropospheric westerlies are stronger than those for the observed data. The partitioning of kinetic energy into zonal and eddy parts may be affected by the internal viscosity and surface friction.

The computed lower level tropical easterlies appear to be rather shallow (Manabe and Smagorinsky, 1967).

It is interesting to note that Mintz (1965) obtained a reasonable intensity of westerlies in both winter and summer hemispheres in his global general circulation study, even though the calculations were at two levels and vertical extrapolations were made for the westerlies. He suggested that "when a smooth wall is placed at the Equator, no mean easterly wind is generated at any level over the Equator." Our model has a smooth wall at the Equator, but the easterlies are present. It has been speculated that the shallowness of the layer of easterlies in the Tropics might be due to inadequate diffusion of momentum in the Ekman boundary layer.

EDDY KINETIC ENERGY

This quantity is defined by

$$\rho(\overline{u'^2} + \overline{v'^2})/2,$$

where ρ is the density. (See fig. 37.)

The computed eddy kinetic energy is much smaller than the observed, as has been mentioned in section 9. However, both the observed and the computed data have two midlatitude maxima of eddy kinetic energy in the vertical distribution. One is at level 4 and the other at
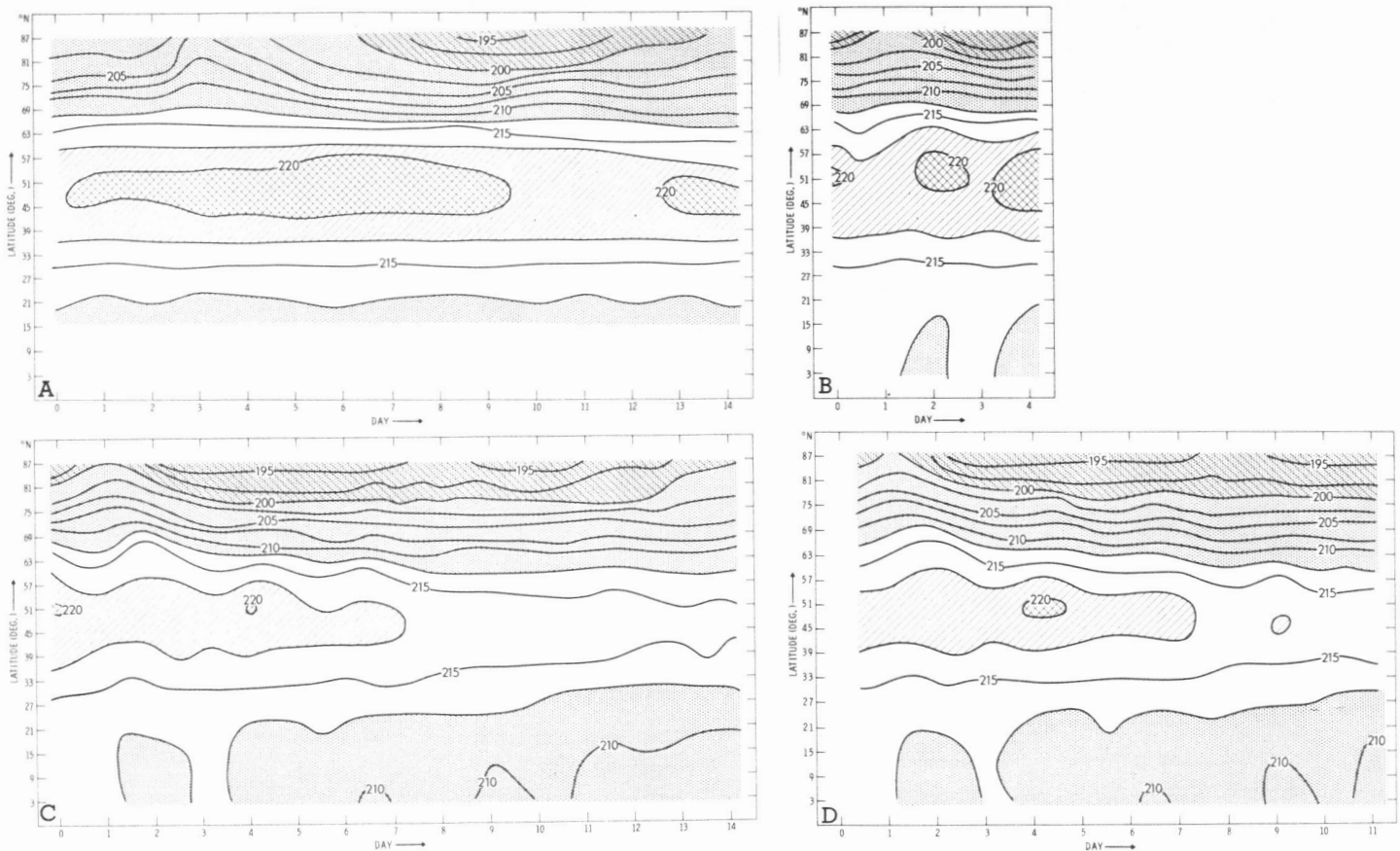
FIGURE 35.—The zonal average of temperature at the 50-mb level in units of °K. The ordinate is latitude, and the abscissa is time. (A) the observed, (B) Experiment 1, (C) Experiment 2, and (D) Experiment 3. The area where temperature is higher than 217.5°K is hatched, and that where it is lower than 212.5°K is stippled.

level 8 or 9. The vertical spacing of the centers is consistent with the vertical flux of geopotential, which is given by $\overline{\omega'\phi'}$, where

$$\phi' = \phi - \overline{\phi}, \quad \phi = gz,$$

z being the geopotential height (fig. 57 in Appendix II). This quantity is known to play a role in the vertical propagation of eddy kinetic energy. The source of eddy kinetic energy $(-\overline{\omega'\alpha'})$ is located at level 6 or 7 as in figure 40. The flux $\overline{\omega'\phi'}$ largely redistributes the eddy kinetic energy upward above level 4.5 or 5.5, and downward to the lower levels.

In the 1964 and the 1966 cases, the observed eddy kinetic energy has two maxima; one is at 45°N and the other at 75°N. On the other hand, Experiments 2 and 3 for the 1964 case have two maxima, but they are not widely separated. In the experiment for the 1966 case, there is only one maximum, which is at 39°N.

VERTICAL VELOCITY

It may be rather surprising that the distribution of vertical velocity computed from the ω-equation and from the prediction computation are not very different from each other, except in the Tropics, of course. (See fig. 38.) However, as is to be expected, the vertical velocities calculated by the ω-equation (which excludes heating) are

weaker than those taken from the prediction computation, which is based on the time dependent primitive equation.

Comparing the vertical velocities between Experiments 2 and 3, it is seen that the intensity of the tropical Hadley circulation is weaker in Experiment 3 than in Experiment 2. This is consistent with the fact that condensation in the Tropics is relatively large in Experiment 2 compared with that in the middle latitudes. On the other hand, the intensity of the middle latitude Ferrel circulation in the troposphere is stronger in Experiment 3 than in Experiment 2.

MERIDIONAL CIRCULATION

The meridional circulation was constructed using $\overline{W}$ and $\overline{v}$ determined by first applying the ω-equation to the observed data and then computing it by the model in Experiment 3. (See fig. 39.) The vectors were drawn exactly, and the streamline analyses were done subjectively. These circulations were computed for the domain of the Northern Hemisphere below an altitude of about 30 km. A distortion of circulation pattern may be included due to the restriction of the domain.

In the troposphere, we see the typical three-cell circulation. The tropical cell extends into the lower stratosphere, where it expands polewards.
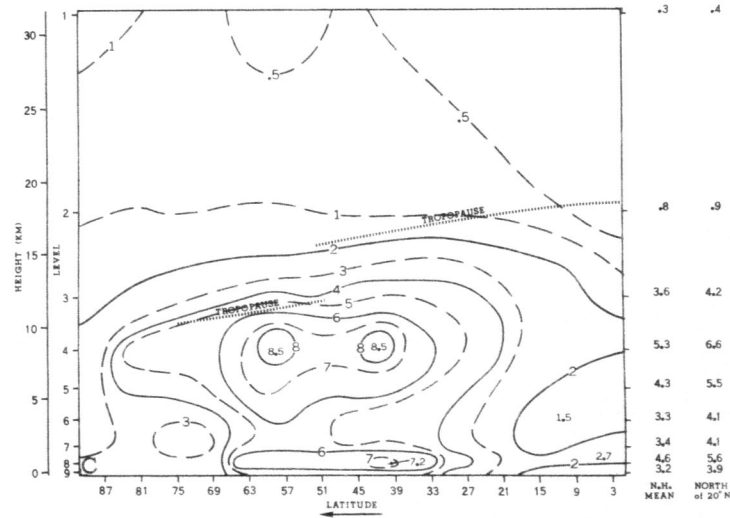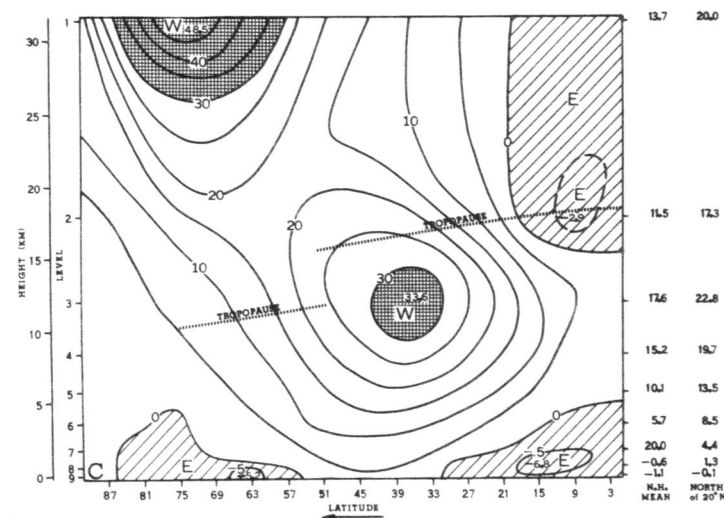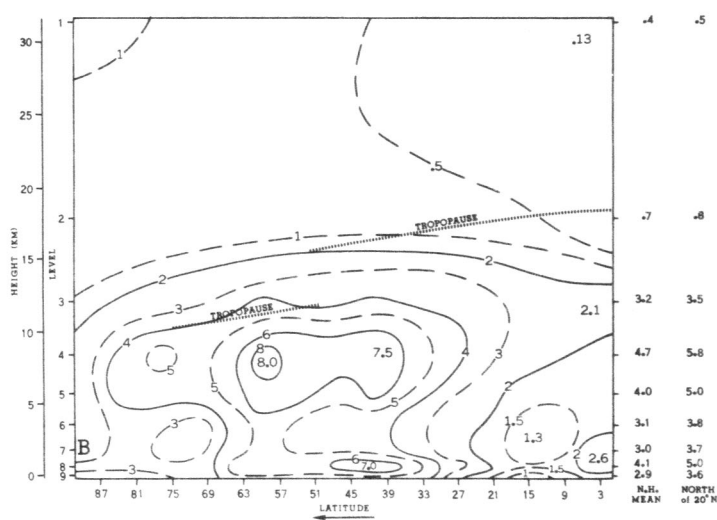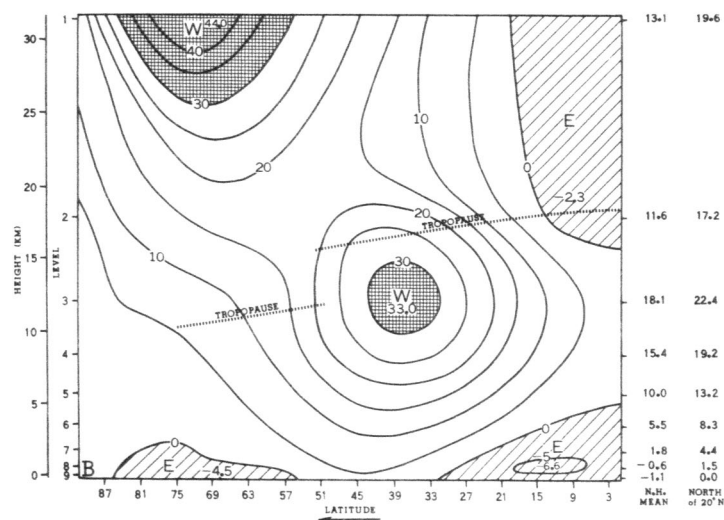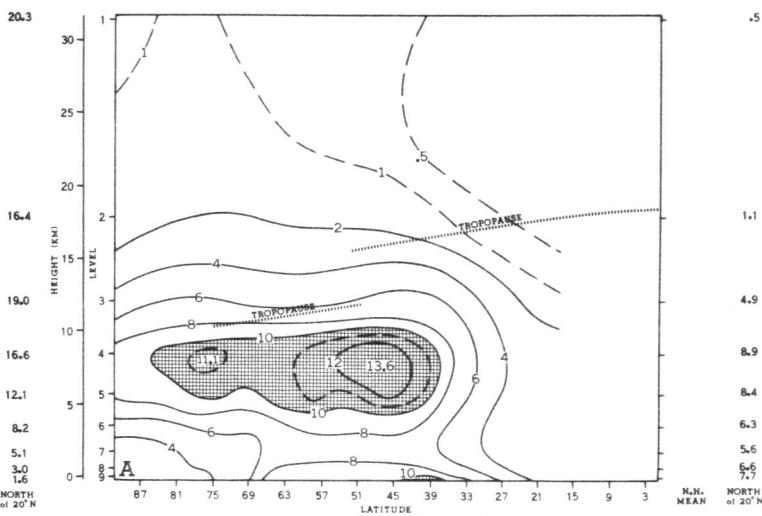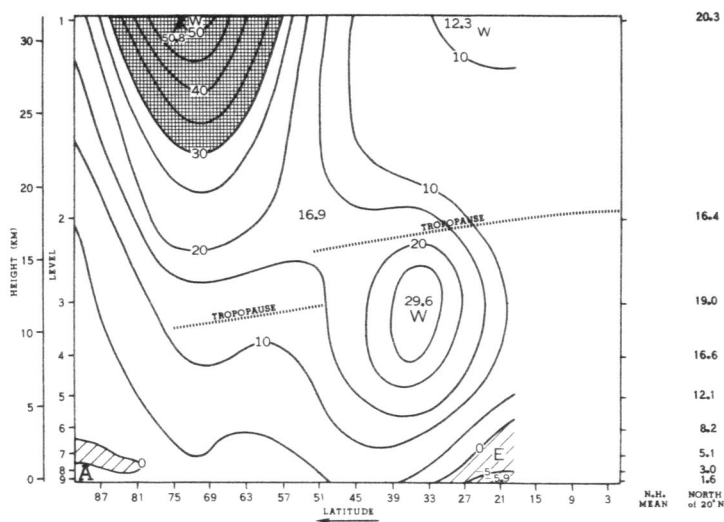
FIGURE 36.—Meridional section of zonal wind $\overline{U}$ in units of meters per second. The regions of westerlies (W) where wind intensity is larger than 30 m/sec are stippled, and the easterlies (E) are hatched. Extreme values are plotted. (A) the observed (time averaged for the period 0 to 14 days), (B) Experiment 2, and (C) Experiment 3 (the latter two are averaged for the period 3 to 14 days).

FIGURE 37.—Meridional section of the eddy kinetic energy $\rho(\overline{u'^2} + \overline{v'^2})/2$ in units of 10^2 ergs/cm³. The regions where the intensity is larger than 10^3 ergs/cm³ are crosshatched. The maxima are plotted. (A) the observed (time averaged for the period 0 to 14 days), (B) Experiment 2, and (C) Experiment 3 (the latter two are averaged for 3 to 14 days).

In the lower stratosphere in January, there is a two-cell circulation with a strong downward current at about 45°N to 63°N. This type of stratospheric circulation predominated during January for the years 1957, 1958, 1963, 1964, and 1966.

CONVERSION OF EDDY POTENTIAL TO EDDY KINETIC ENERGY

The rate of conversion is defined by $-\rho\overline{\omega'\alpha'}$, where $\alpha = \rho^{-1}$ is the specific volume. (See fig. 40.) If this quantity is positive, it means that eddy available potential energy is converted into eddy kinetic energy (see Oort, 1964, for a general discussion).

The distribution of this quantity in the predicted result corresponds fairly well with its observed distribution as determined from the solution of the ω-equation. However, the intensity of the rate of conversion is much greater in the prediction.

In both the 1964 and the 1966 cases (fig. 76), there are four large positive regions. Two are located in the middle latitudes, i.e., about 39°N to 45°N and 57°N to 75°N at level 7 (prediction) or level 6 (ω-equation). The third is in the lower stratosphere at level 1 at about 63°N. The fourth is just under the tropical tropopause at level 4. This last one was first found by Manabe and Smagorinsky (1967), though it is still not completely confirmed.

The region in the Tropics is of special interest, because it may be one of the source regions of eddy kinetic energy for the development of easterly waves. It should be said, however, that the location and intensity of the region as well as the shallowness of the tropical easterlies are yet to be confirmed by other models.

Other statistical quantities are also given in Appendixes II and III.

11. PRECIPITATION FORECAST FOR THE NORTHERN HEMISPHERE

It is almost impossible at present to collect worldwide observations of precipitation, expecially over the oceans. Televised cloud pictures of recent meteorological satellites could provide the basis for estimating the distribution of the global weather. However, for these present cases, daily satellite coverage of the whole globe was not available.

Figure 41 is the climatological cloudiness for January. The data were taken from TIROS satellite analysis by Clapp (1964) and Sadler (1968). Since the satellite pictures did not cover the polar region, Landsberg's (1945) cloud data based on surface observations were also used. Figure 41 was constructed by using Sadler's result between 0° and 25°N, Clapp's between 25° and 55°, and Landsberg's between 55° and 90°N.

The northern hemispheric precipitation predicted in Experiment 3 of the 1964 case and averaged for the period 3 to 14 days (fig. 42) (the 1966 case is in fig. 91 of Appendix III) is compared with the total cloudiness (fig. 41).
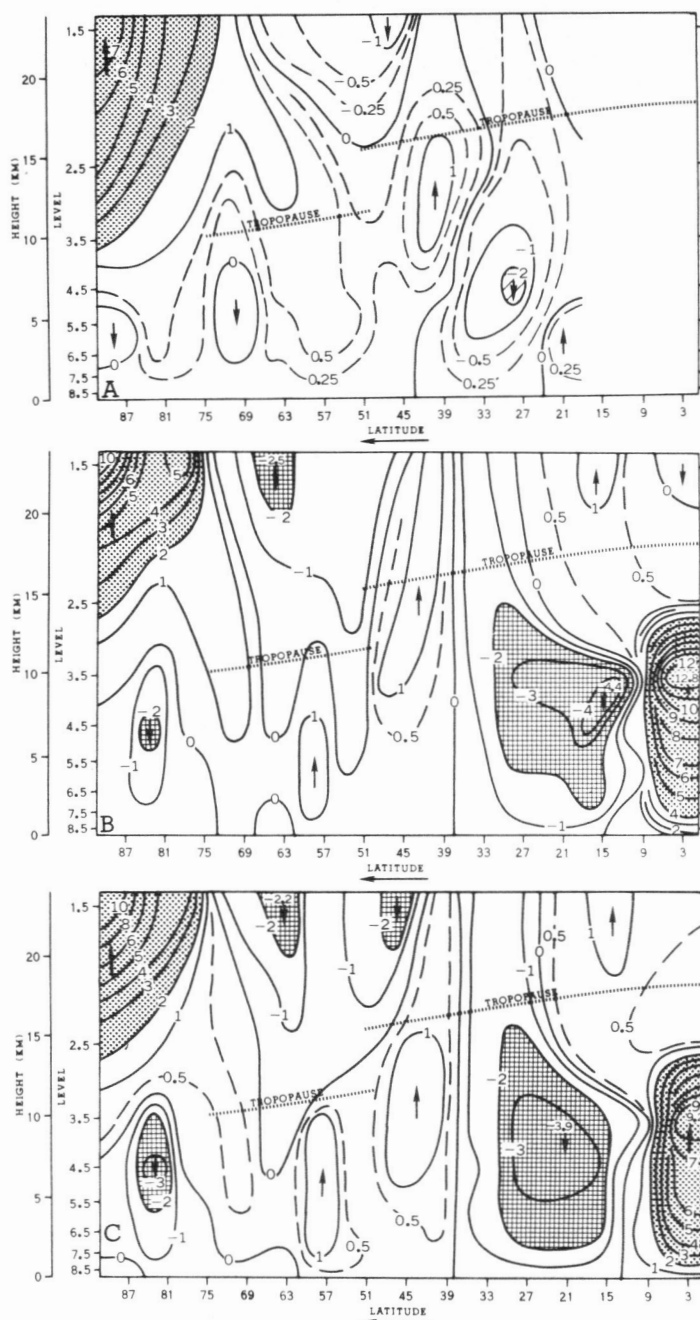
FIGURE 38.—Meridional section of the vertical velocity $\overline{W} = \overline{dz}/dt$ in units of 10^{-1} cm/sec. The direction of velocity is indicated by arrows. The regions where the upward velocity is larger than 0.2 cm/sec are hatched, and the regions where the downward velocity is larger than 0.2 cm/sec are stippled. (A) computed by applying the ω-equation to the data for each of the 14 days and then averaged, (B) Experiment 2, and (C) Experiment 3. The latter two are averaged for 3 to 14 days.

It is noted by comparison that 1) in the middle and high latitudes the agreement is fairly good, but 2) the computed precipitation over western Russia appears too small, and 3) the tropical precipitation in the prediction departs very definitely from the speculated reality through the observed cloudiness.
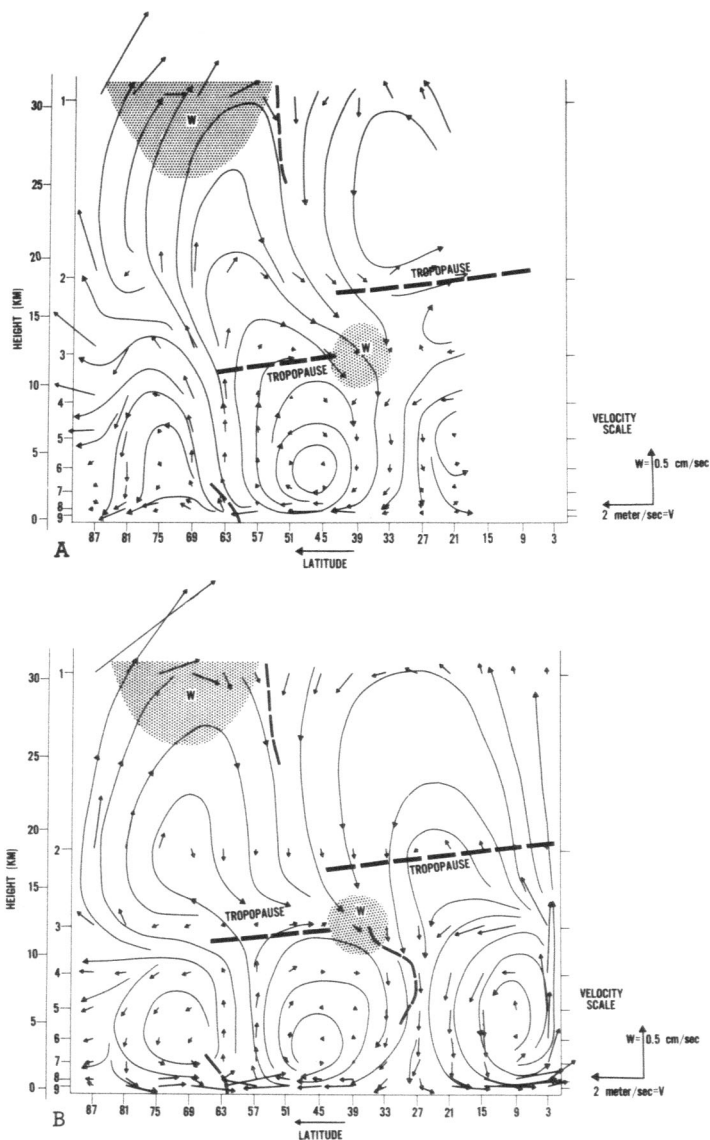
FIGURE 39.—Meridional circulation. The arrows plotted at the gridpoints are drawn according to the scales shown in the lowest right corner. The centers of the tropopause jet and polar-night jet are indicated by shading and by (W). (A) obtained by solving the ω-equation (see fig. 38) and (B) Experiment 3 (time averaged for 3 to 14 days).

The tropical discrepancy is especially pronounced over equatorial Africa and the middle Pacific Ocean. In these areas, there were few clouds in reality, whereas there was a large amount of precipitation in the prediction. In view of this serious error, it would be interesting to know how much damage was done to the middle latitude flow forecast.

12. CONCLUSIONS

The 2-week prediction of synoptic-scale weather systems in January by hydrodynamical methods appears promising. Of course, we cannot make a definitive state-
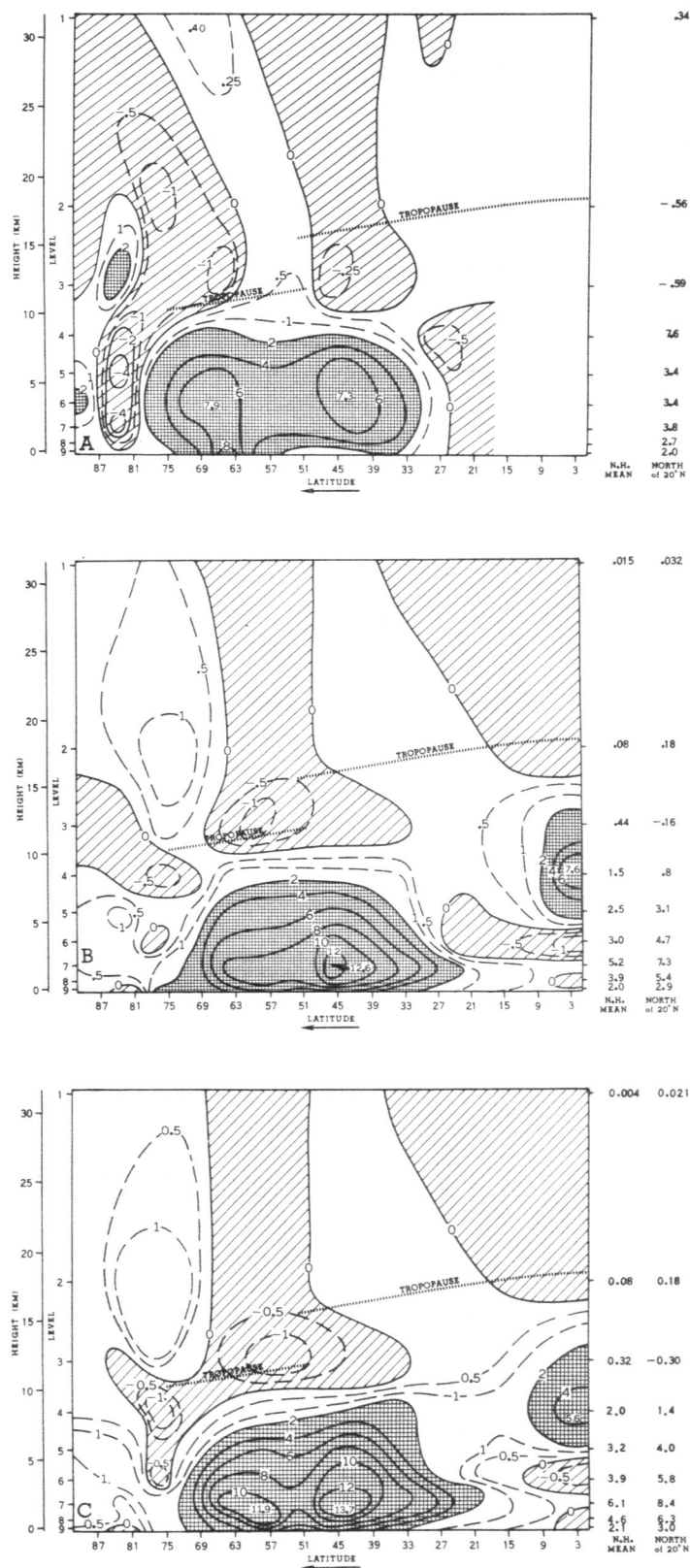
FIGURE 40.—Meridional section of the conversion of eddy available potential energy to eddy kinetic energy, $-\rho\overline{\omega'\alpha'}$ in units of 10^{-3} ergs cm^{-3} sec^{-1}. The regions where the intensity of $-\rho\overline{\omega'\alpha'}$ is greater than 2×10^{-3} ergs cm^{-3} sec^{-1} are crosshatched. Negative regions are hatched. (A) obtained by solving the ω-equation and using the observed temperature, (B) Experiment 2, and (C) Experiment 3; the latter two are averaged for 3 to 14 days.
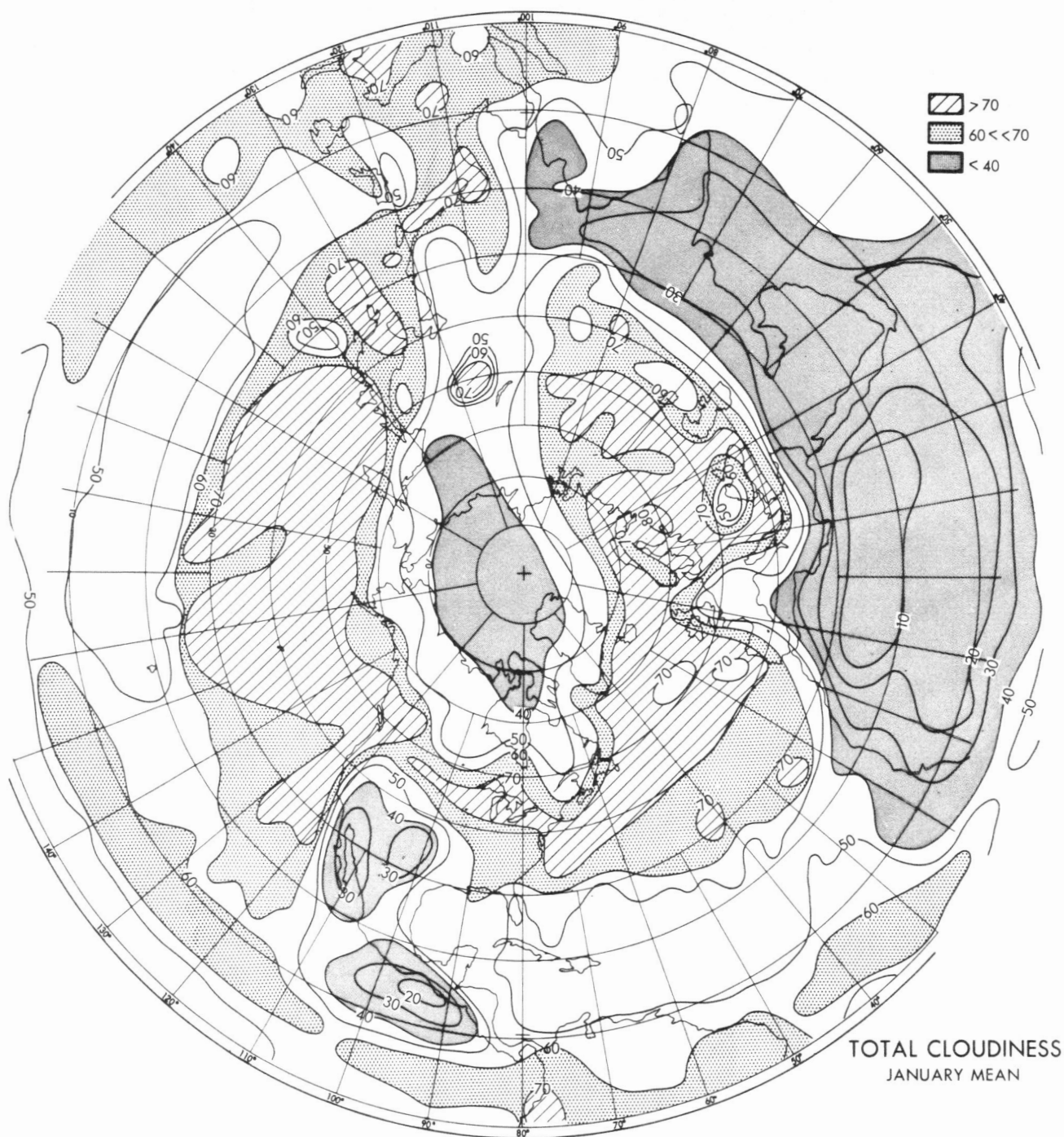
FIGURE 41.—Mean total cloudiness for January. The data are taken from Landsberg (1945), Clapp (1964), and Sadler (1968), and given in percent of cover. The areas where cloudiness is higher than 70% are hatched, and those where cloudiness is less than 40% are stippled.

ment because of the small sample size. In the present study, the trough and ridge diagrams show a correspond-ence between forecast and observed, and the correlation coefficients of the *height change* of the 500-mb surface from the initial time between the observed and the fore-cast were 0.5 in the 1964 case and 0.4 in the 1966 case at the 14th day. The coefficients decreased with time, but

the deterioration was not as rapid as one might have thought.

The 1000-mb forecasts were inferior to the 500-mb forecasts, but the fact that the 500-mb predictions were good is encouraging. Further improvements can be ex-pected in the foreseeable future through more adequate observations, more effective assimilation of the data, a
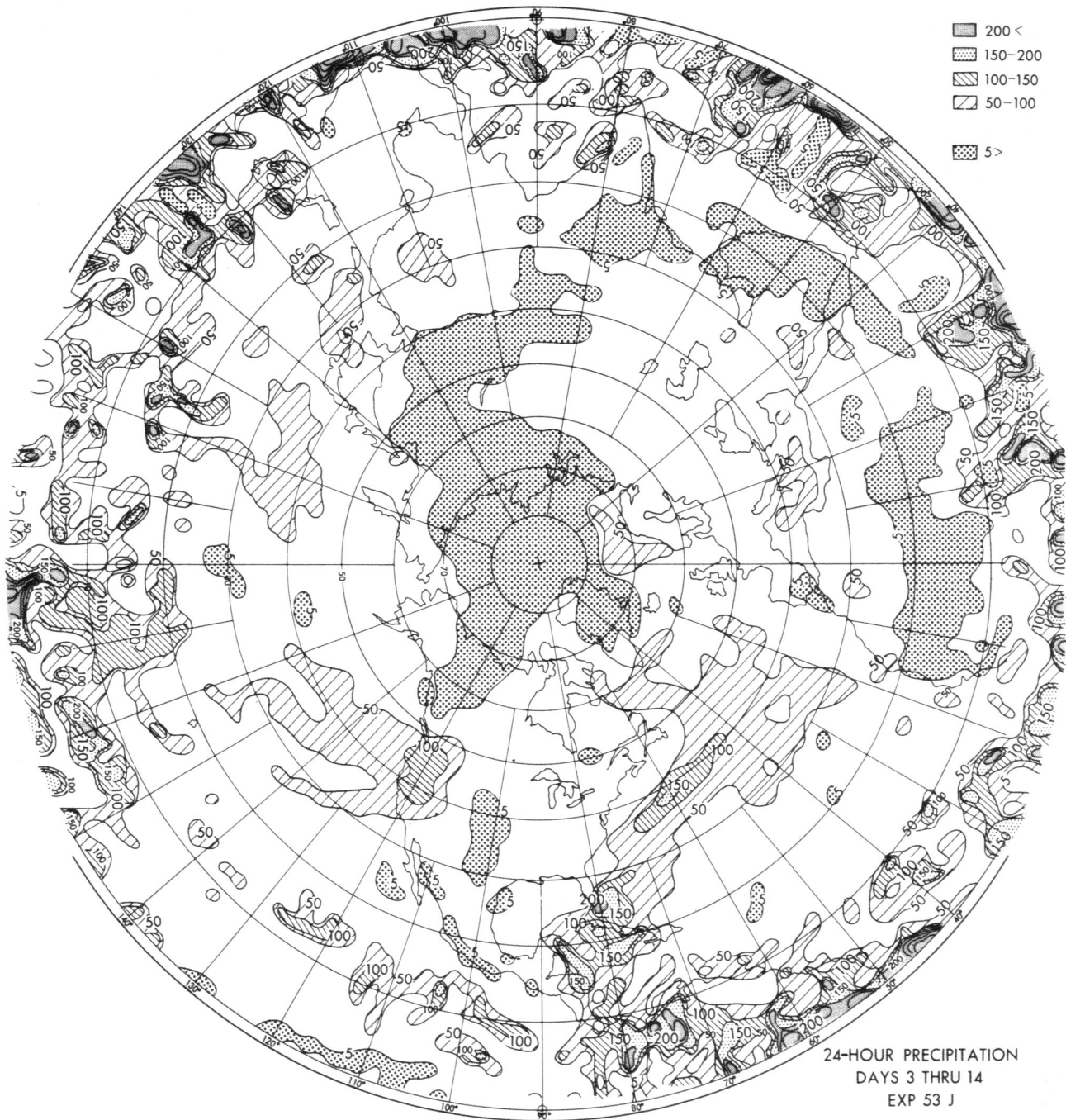
FIGURE 42.—Twenty-four hour rate of precipitation for Experiment 3 averaged for the period 3 to 14 days, units in 10^{-2} cm.

more realistic and sophisticated model, and reduced truncation error.

In particular,

1) It was possible to account for the formation and evolution of second- and third-generation extratropical cyclones.

2) The forecast beyond 3 days for the lower levels was greatly improved by allowing heat exchange with the ocean surface.

3) Because of the inclusion of radiative effects and moisture supply, the hemispheric precipitation is increased by a factor of 5, the main increase occurring in the Tropics.

4) The computed amount of condensation is comparable to the actual rainfall intensity, but the computed condensation covers a wider area than the real rainfall area. It is quite often not zero in areas where there is no rain reported.

5) The 80% condensation criterion leads to a considerable improvement in the forecast of water vapor especially at the 850-mb level, and it contributes to an increase in precipitation. With a reduction of the condensation criterion from 100% to 80%, the condensation remains almost the same at the Equator, whereas it increases farther north in the Tropics and in the middle latitudes.

6) The tropical Hadley circulation is more intense with a 100% criterion, while the middle latitude Ferrel circulation is more intense with 80%.

7) A distinction between the thermal properties of sea-ice and land-ice surfaces is necessary for the prediction of reasonable temperatures in the lower levels at high latitudes.

8) In all of the present experiments, the computed temperature is lower than the actual temperature.

9) When one allows for land-sea thermal contrast, a strong land breeze is created in winter. A large truncation error results because the horizontal resolution of the grid is too coarse.

10) The zonal kinetic energy in the forecast is systematically larger than observed, especially at the tropospheric jet level.

11) On the other hand, the eddy kinetic energy in the forecast is smaller than the observed in the troposphere. This is reflected in the pattern of geopotential height. The difference in height between cyclones and anticyclones in the forecast becomes considerably smaller than in the observed pattern in the troposphere as the forecast progresses. Likewise, in considering only the large-scale flow of the stratosphere, the computed flow pattern tends to become zonally symmetric.

12) The eddy kinetic energy in the troposphere and the intensity of the conversion of eddy potential energy into eddy kinetic energy is systematically larger with an 80% condensation criterion than with a 100% criterion.

13) In the latitude-time chart of zonal wind, the northern branch of the jet maximum disappears as the prediction proceeds.

14) In this hemispheric model, the tropical precipitation seems to deviate from reality especially in equatorial Africa and in the middle Pacific Ocean.

ACKNOWLEDGMENTS

APPENDIX I.—TABLES OF QUANTITIES USED FOR THE RADIATION COMPUTATION

TABLE 3.—*Cloud distribution in January (after Telegadas and London, 1954)*

Latitude	High			Middle			Low				
	Height (km)	Level	Amount	Height (km)	Level	Amount	Top height	Top level	Base height	Base level	Amount
0	9.4	4	.213	4.2	6	.080	3.0	6	1.6	7	.343
10	9.9	4	.159	4.2	6	.060	2.9	6	1.7	7	.261
20	10.2	3	.136	4.2	6	.055	2.7	6	1.7	7	.231
30	10.0	4	.157	4.0	6	.069	2.5	7	1.7	7	.291
40	8.9	4	.186	3.8	6	.095	2.3	7	1.5	7	.384
50	7.6	4	.203	3.7	6	.122	2.2	7	1.3	7	.441
60	7.0	4	.197	3.6	6	.121	2.0	7	1.2	8	.438
70	6.8	4	.157	3.5	6	.099	1.9	7	1.1	8	.375
80	6.8	5	.115	3.4	6	.083	1.8	7	1.0	8	.304
90	6.8	5	.085	3.4	6	.073	1.7	7	0.9	8	.250

TABLE 4.—*Mixing ratio of water vapor in January* (10^{-3} *gm/gm*)

Latitude	Level (k)						
	3	4	5	6	7	8	9
0	.034	.59	2.30	5.40	10.00	14.00	18.00
10	.032	.52	1.80	4.00	7.60	12.00	16.00
20	.022	.34	1.30	2.80	5.60	8.80	12.00
30	.011	.19	.78	2.00	3.80	6.20	7.50
40	.0070	.12	.50	1.40	2.60	3.60	4.20
50	.0054	.064	.31	.85	1.60	2.00	2.20
60	.0044	.036	.19	.50	.84	1.00	1.20
70	.0040	.024	.13	.34	.48	.53	.55
80	.0036	.016	.088	.22	.28	.30	.30
90	.0034	.011	.062	.14	.17	.18	.18

r ($k=1$)$=0.023\times10^{-3}$ gm/gm.
r ($k=2$)$=0.0028\times10^{-3}$ gm/gm for all latitudes.

TABLE 6.—*Surface albedo for January*

Latitude	Land	Sea
0	.072	.060
10	.105	.060
20	.180	.070
30	.167	.090
40	.244	.110
50	.410	.160
60	.443	.200
70	.662	.240
80	.765	.250
90	.800	.250

TABLE 5.—*Ozone in January* (10^{-5} *cm STP*)

Latitude	Level								
	1	2	3	4	5	6	7	8	9
0	17327	5158	660	347	203	120	94	46	14
10	17470	5833	647	347	201	127	98	56	21
20	17454	6794	731	413	252	161	125	71	27
30	16766	8829	1149	564	376	271	207	111	39
40	14964	11599	3165	922	495	341	280	160	60
50	14090	14378	4859	1394	486	319	248	142	53
60	13127	15540	6057	1425	463	296	216	123	46
70	12377	15297	6693	1665	388	265	196	109	40
80	11860	14548	6988	1800	487	287	207	112	40
90	11769	14436	6934	1786	483	285	206	111	39

APPENDIX II.—SUPPLEMENTING TABLE AND FIGURES FOR EXPERIMENTS 1, 2, AND 3 (1964 CASE)

TABLE 7.—*Hemispheric averages. Time averages are for the 3- to 14- day period for Experiment 2 and the 3- to 10-day period for Experiment 3.*

	Precipitation		Convective precipitation	
	Mean over land cm/cm²/day	Mean over sea cm/cm²/day	Mean over land cm/cm²/day	Mean over sea cm/cm²/day
Exp. 2	0.2032	0.3060	0.0970	0.1613
Exp. 3	0.2232	0.4416	0.0982	0.2329

Budyko's (1963) estimate of annual mean precipitation is 72 cm/cm²/yr=0.1972 cm/cm²/day over continents and 112 cm/cm²/yr=0.3068 cm/cm²/day over oceans.

RADIATION AT THE TOP AND BOTTOM OF THE ATMOSPHERE
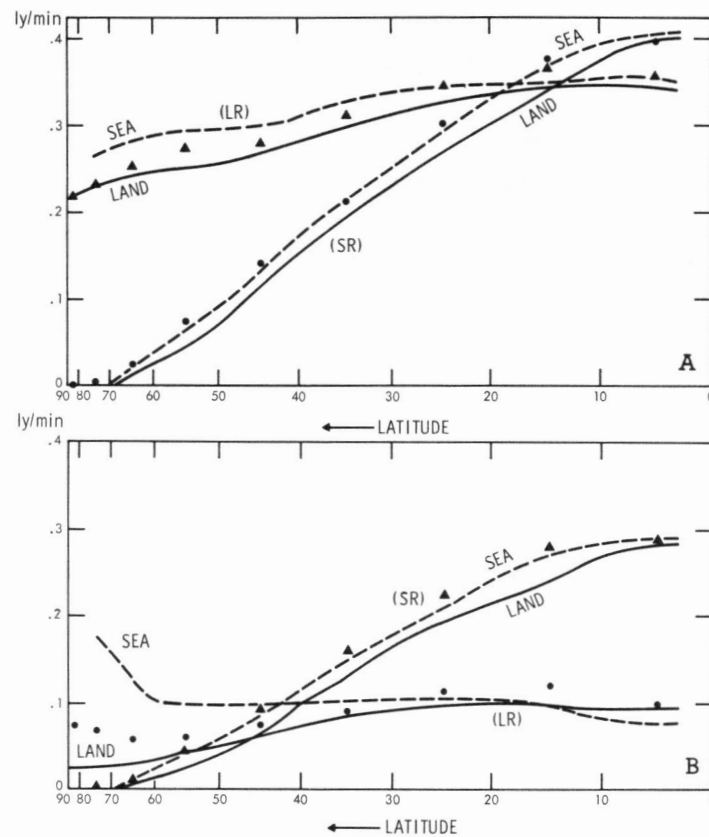
FIGURE 43.—The computed radiation averaged for 14 days in Experiment 2 for the 1964 case. (SR) is the net downward solar radiation, and (LR) the net upward longwave radiation. The quantities over land (solid lines) and over sea (dashed lines) are shown. The dotted curves (small solid circles and triangles) are SR and LR for winter by London (1957), with no distinction between land and sea. Figure (A) is at the top of the atmosphere, and (B) is at the earth's surface.

VERTICAL TEMPERATURE PROFILE
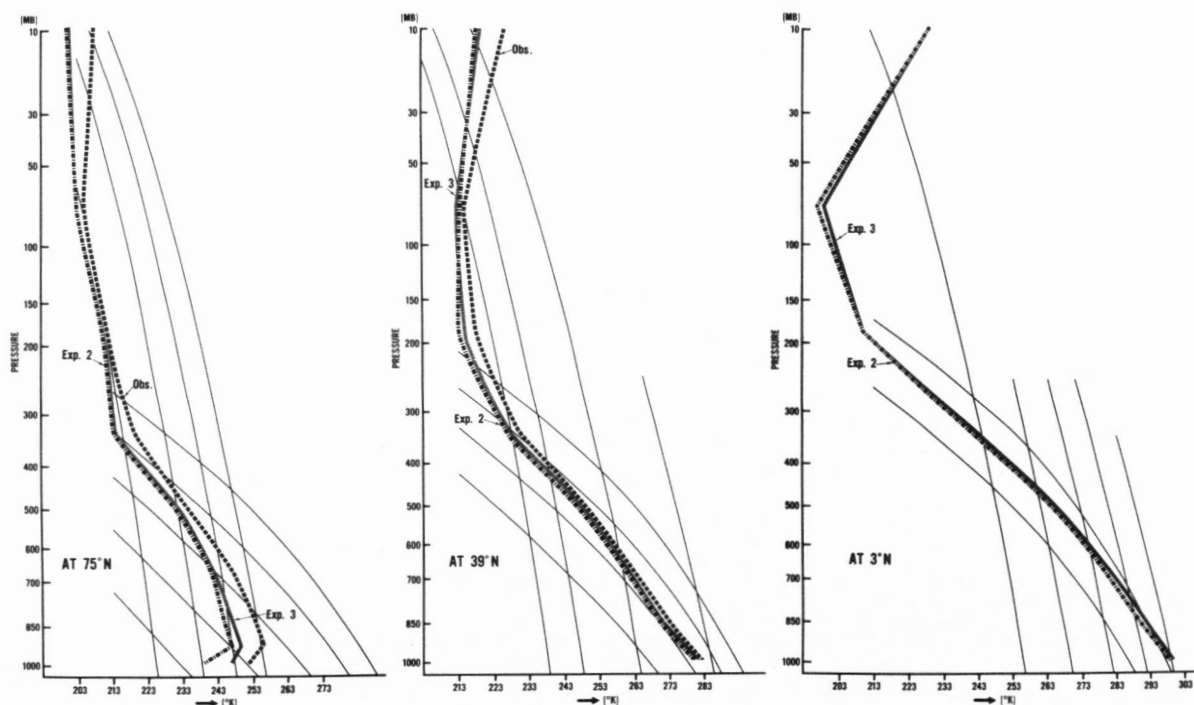
FIGURE 44.—The vertical distribution of zonally averaged temperature at 75°, 39°, and 3°N. The results for Experiments 2 and 3 are shown at the three latitudes, and those for the observed are at 75° and 39°. The thin lines are the moist and dry adiabatic lines.

HEMISPHERICALLY OR ZONALLY AVERAGED PRECIPITATION AND EVAPORATION
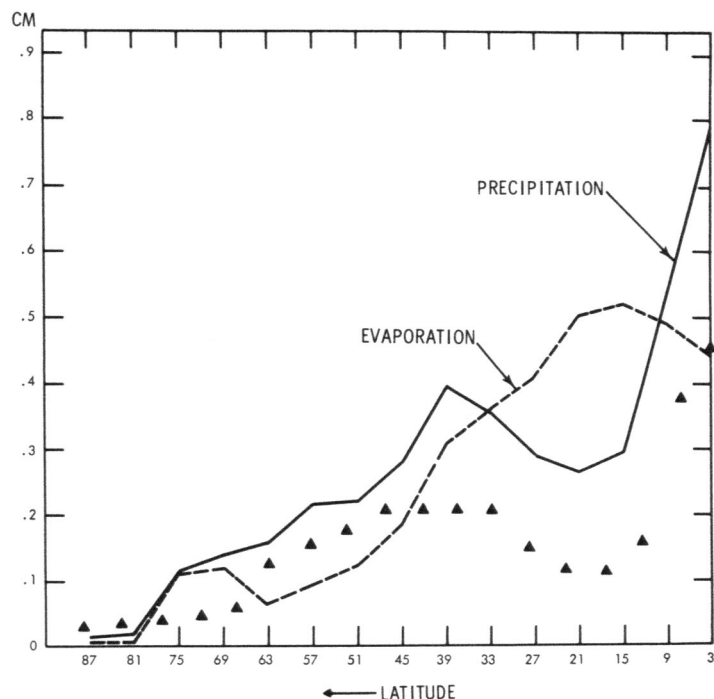
FIGURE 45.—Latitudinal distribution of the 24-hr rates of precipitation and evaporation for Experiment 3. These are zonally and time averaged for the period 4 to 10 days. Triangles are estimates of precipitation for winter by Möller (1951).
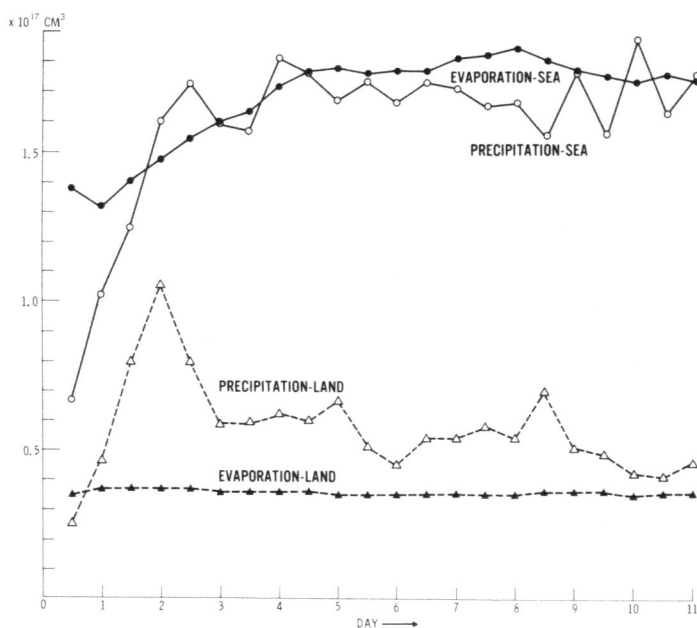
FIGURE 47.—The same as figure 46 but for Experiment 3 (80% condensation criterion).
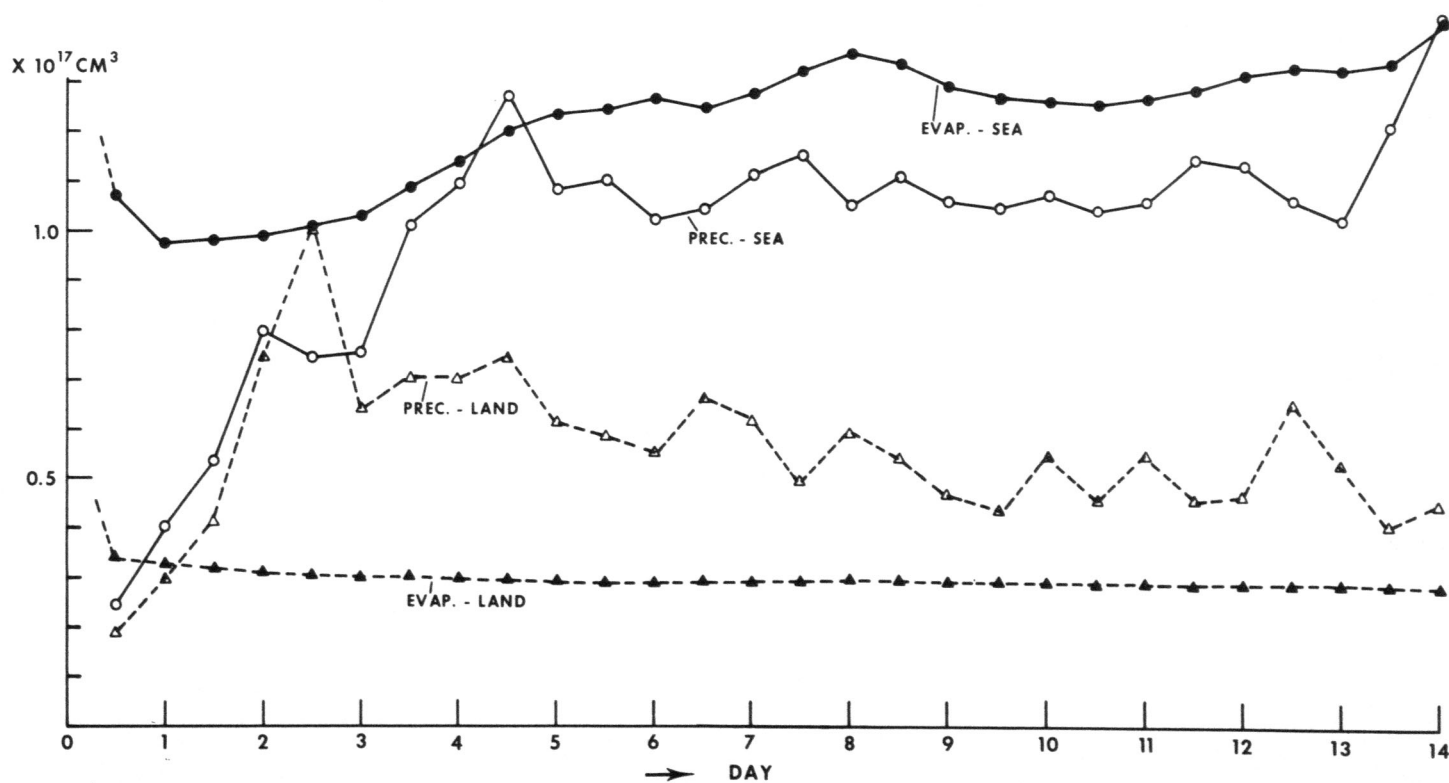
FIGURE 46.—The time variation of the 6-hr rates of precipitation and evaporation in Experiment 2. Both quantities are the total volumes over land and sea for the whole hemisphere. Note that the precipitation was maximum at 2.5 days over land.
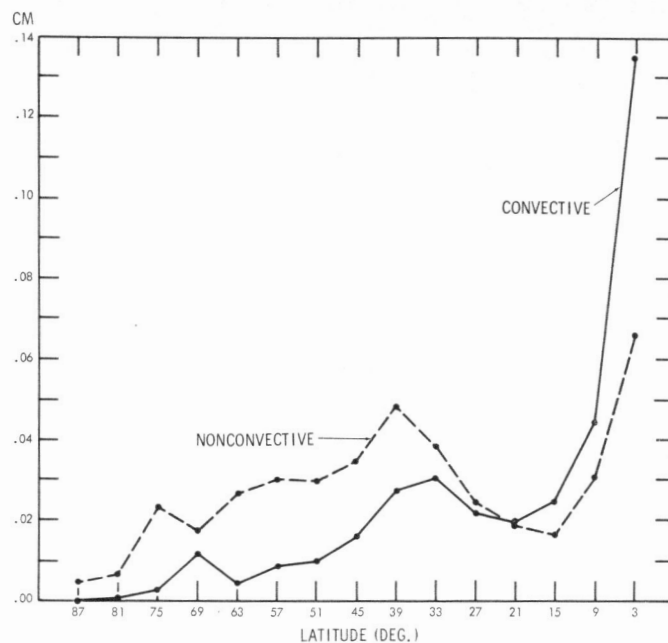
FIGURE 48.—Latitudinal distribution of *convective* and *nonconvective* precipitation in Experiment 2 averaged for the period 3–13 days As mentioned in section 2, the amount of condensation of water vapor was calculated in the following way. Within one time step, and at each gridpoint, the "moist adiabatic temperature adjustment" is first made, and next the large-scale condensation is computed (see detail in Manabe et al., 1965). In constructing this figure, the part of the condensation obtained in the first process is called "convective" type precipitation, and that in the second is the "nonconvective" type. Although this classification is artificial, it gives an approximate idea of the intensity of these quantities. The convective precipitation takes place mostly in the Tropics, whereas the nonconvective precipitation dominates in middle latitudes.

FIGURE 49.—The observed (0 day and left columns) and Experiment 3 (right columns) 1000-mb geopotential height patterns for the period 0 to 14 days commencing at 1200 GMT, Jan. 9, 1964. The contour interval is 60 m. The anticyclone areas with the geopotential value greater than 240 m are hatched, and the cyclone areas with the geopotential value less than 0 m are stippled. The mountains are blank areas enclosed by small segmented lines. The number in the lower right corner is the day of the forecast. "Blocking anticyclones" and "newly formed cyclones" are indicated by the respective letters and arrows. The letters A, B, C, etc. are used for identification.
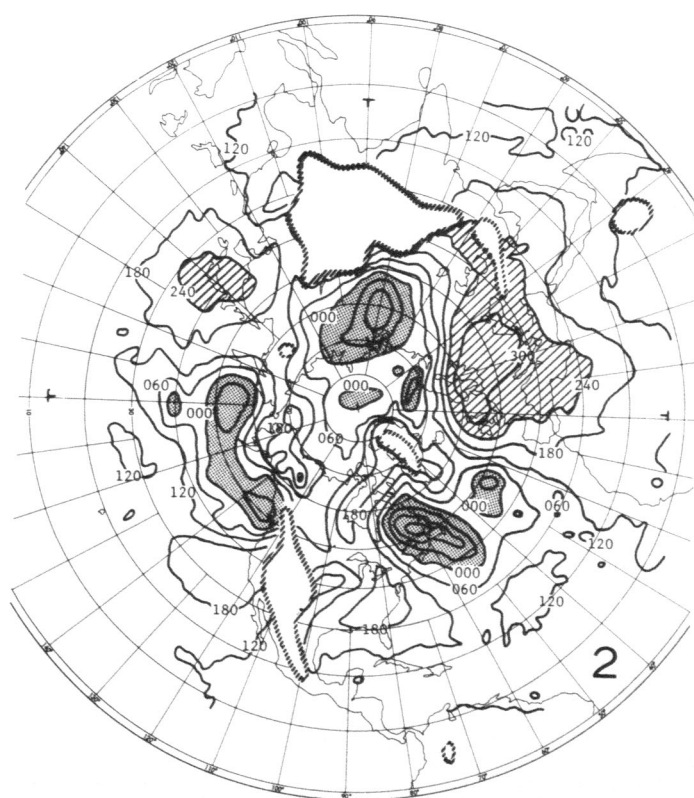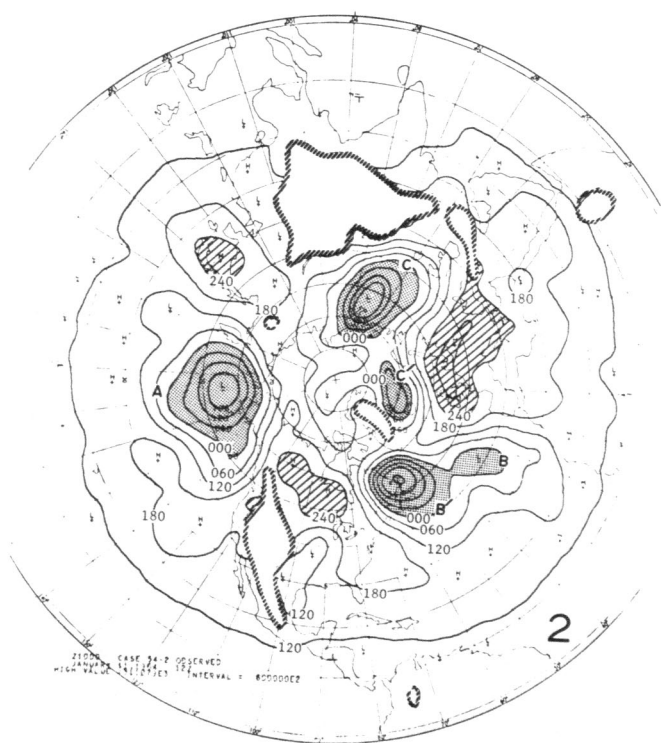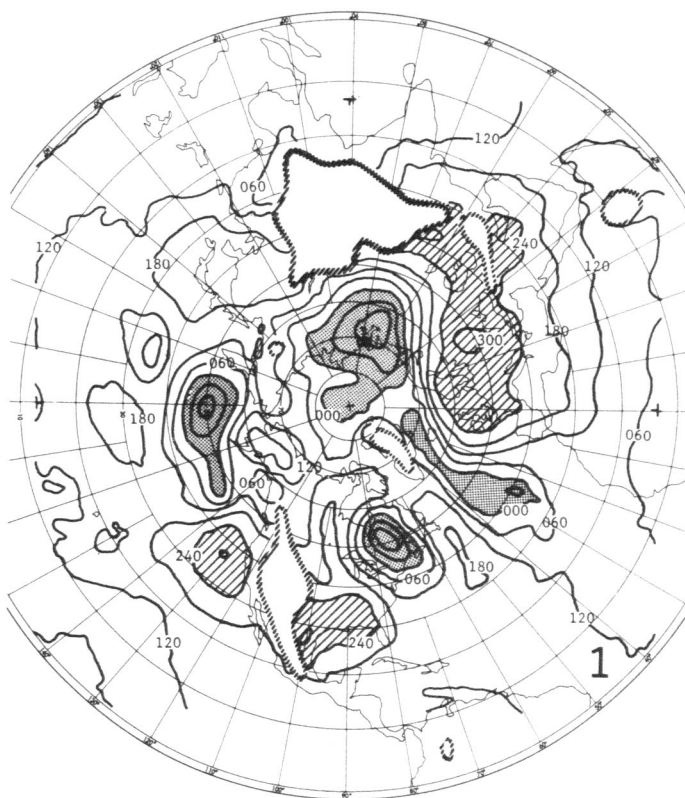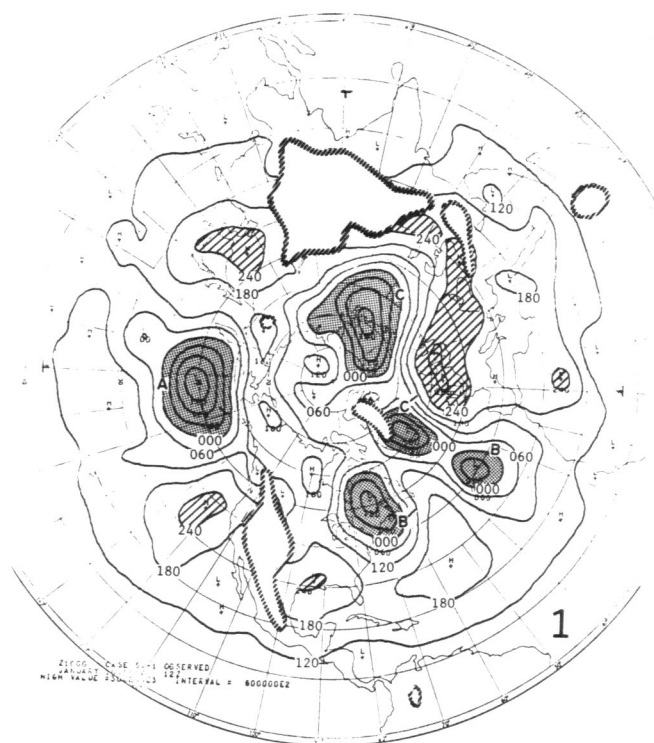
FIGURE 49.—Continued
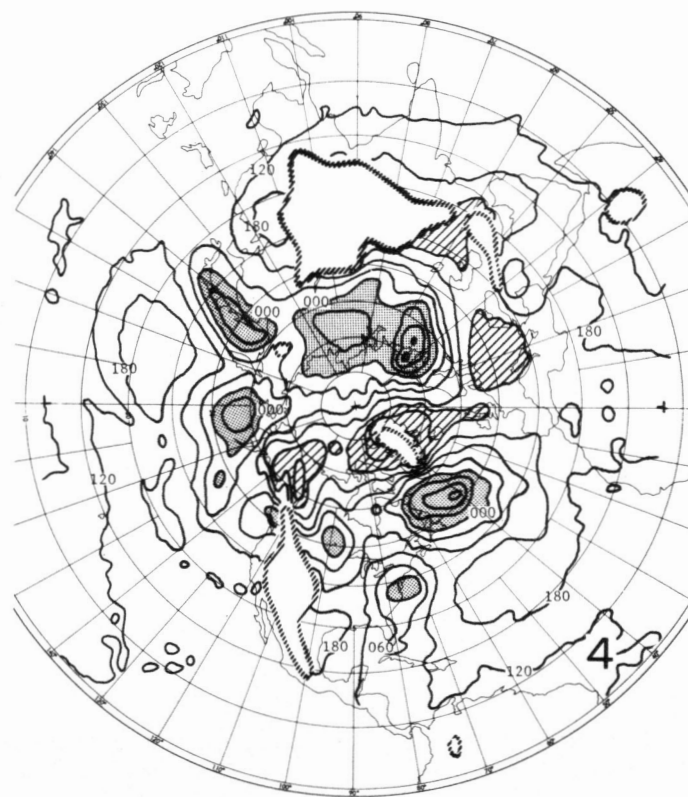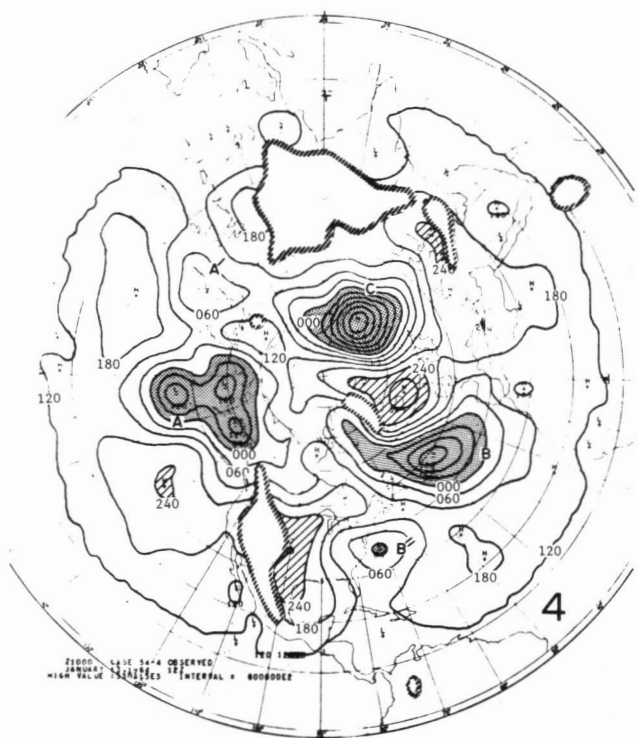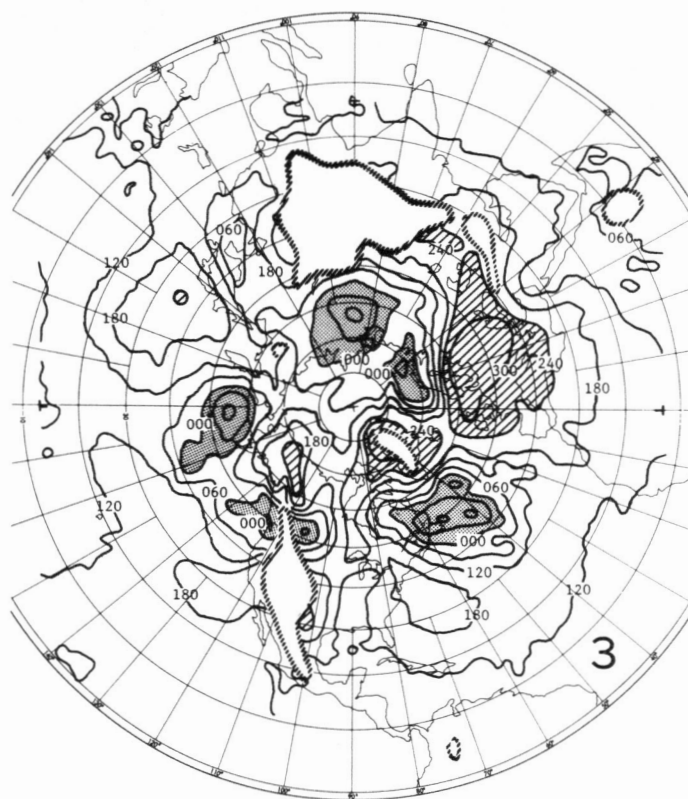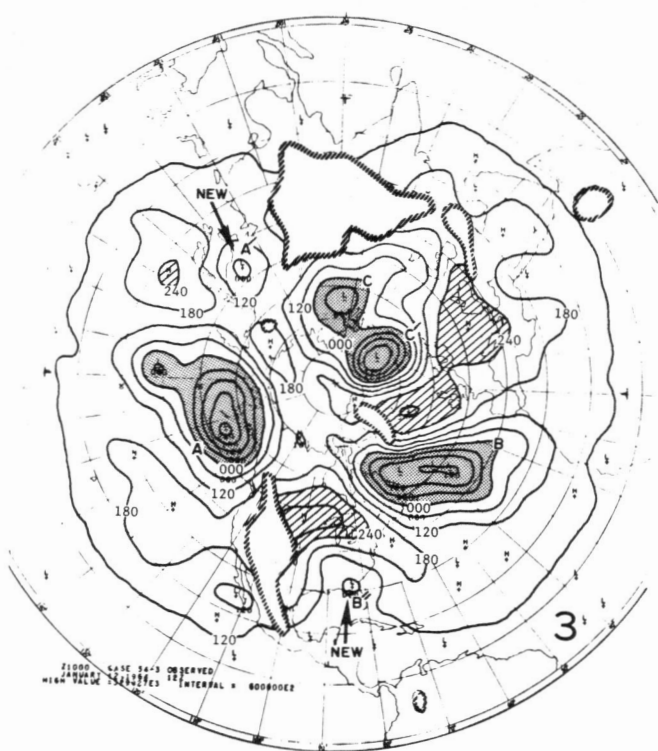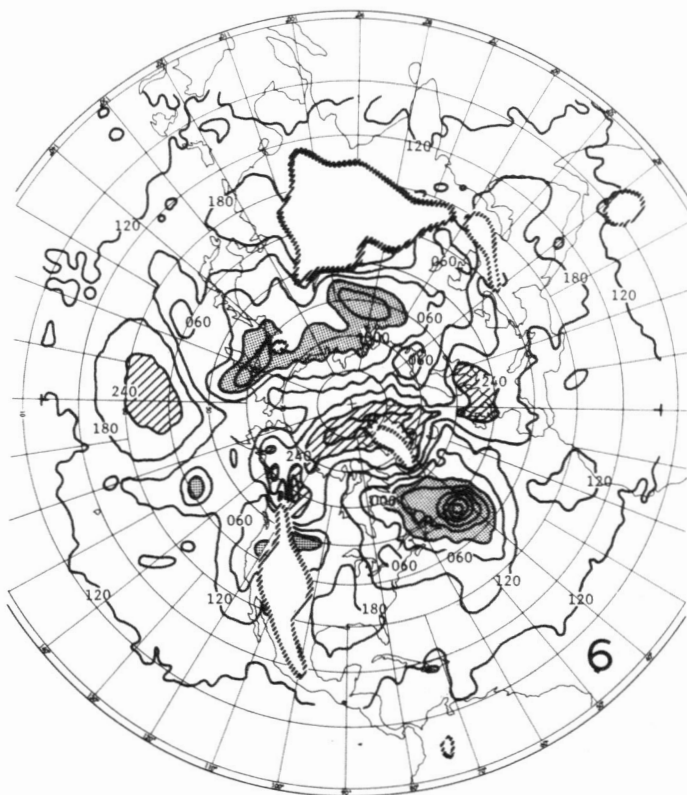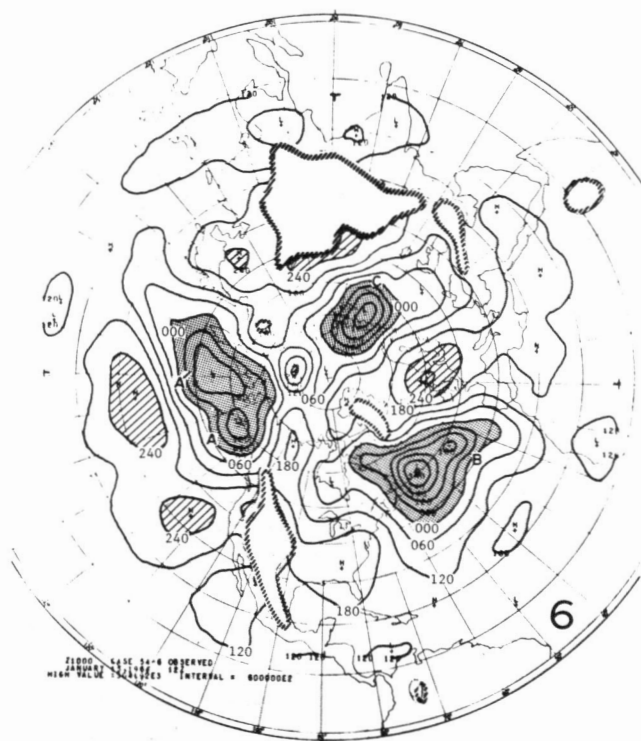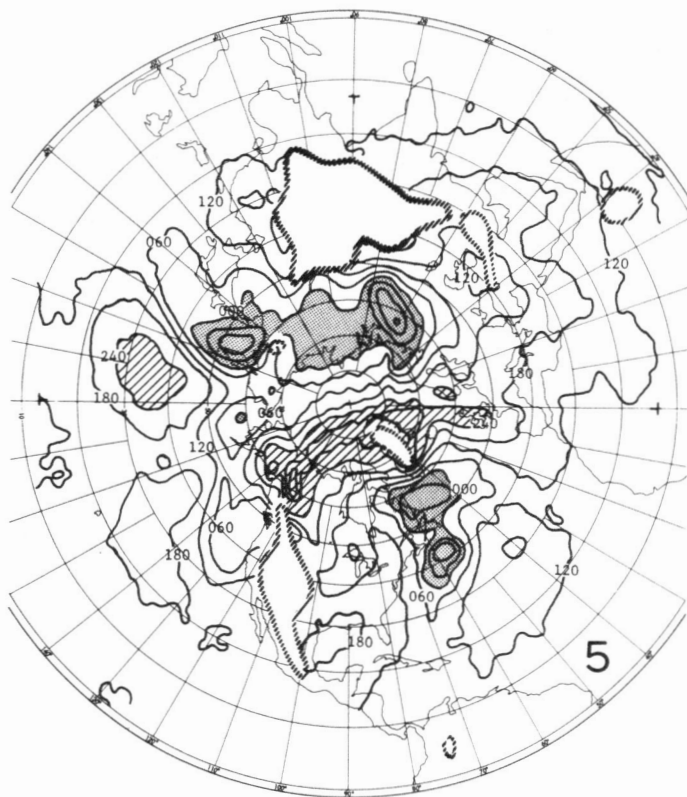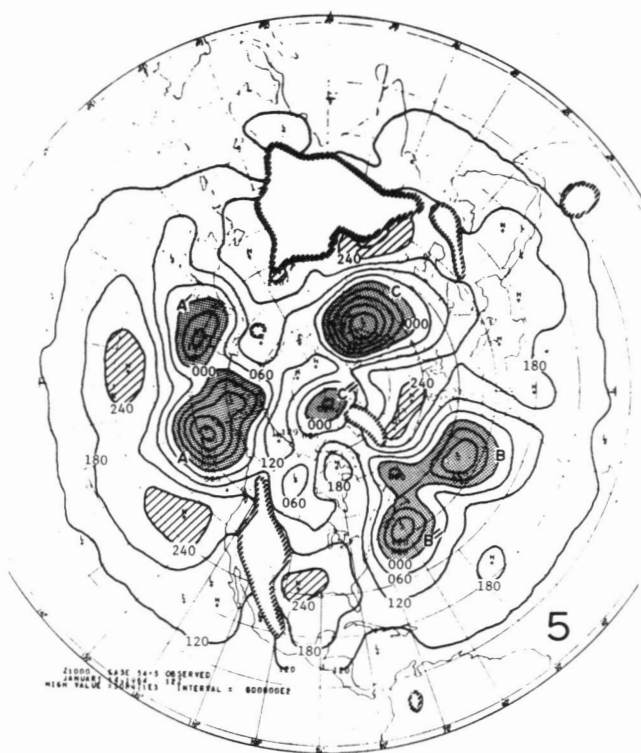
FIGURE 49.—Continued

FIGURE 49.—Continued
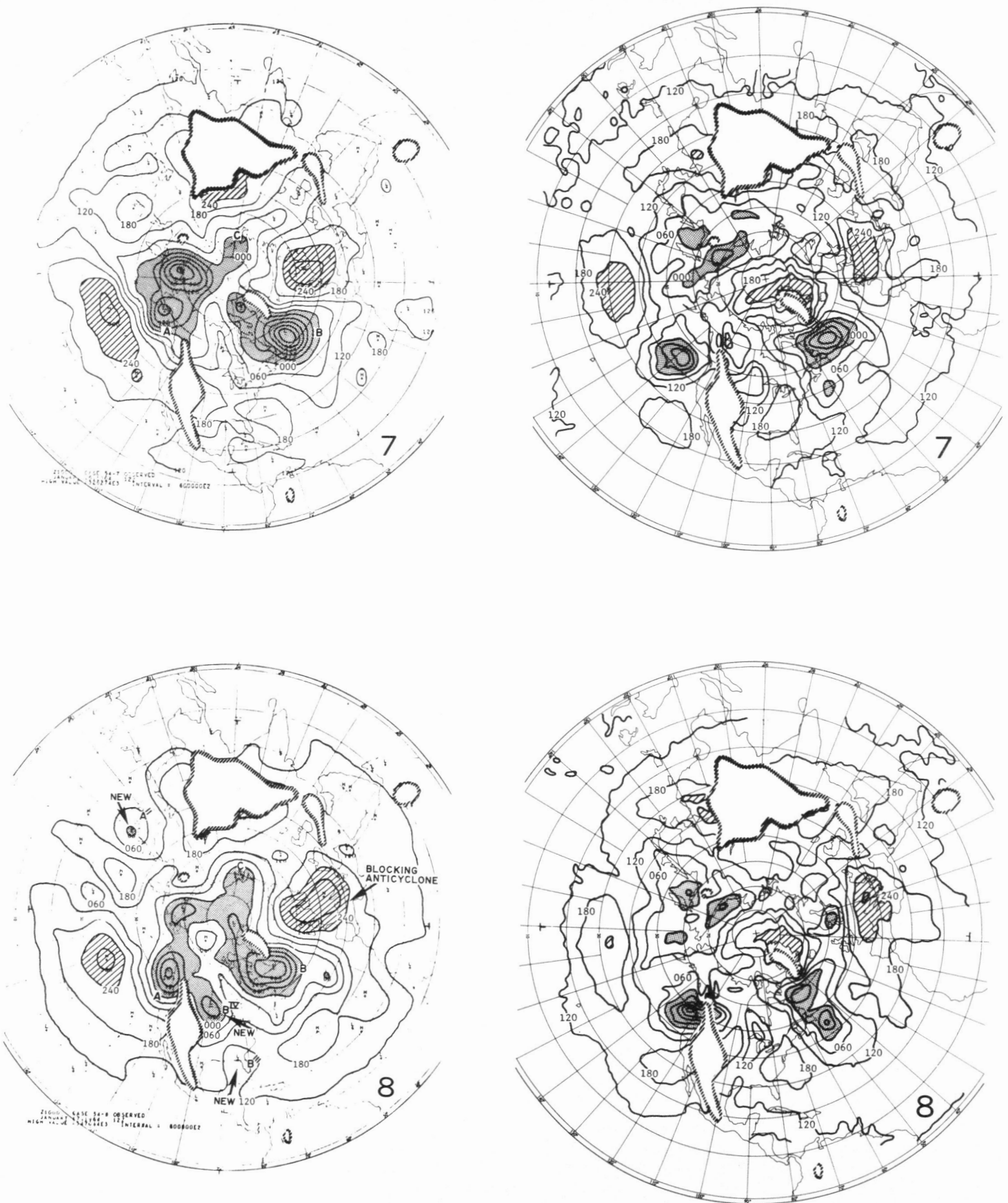
FIGURE 49.—Continued
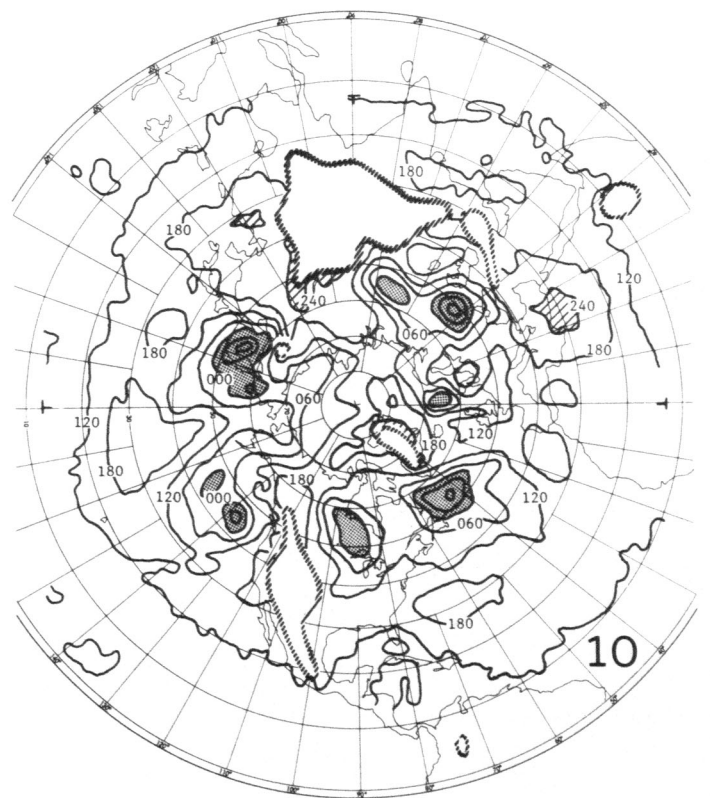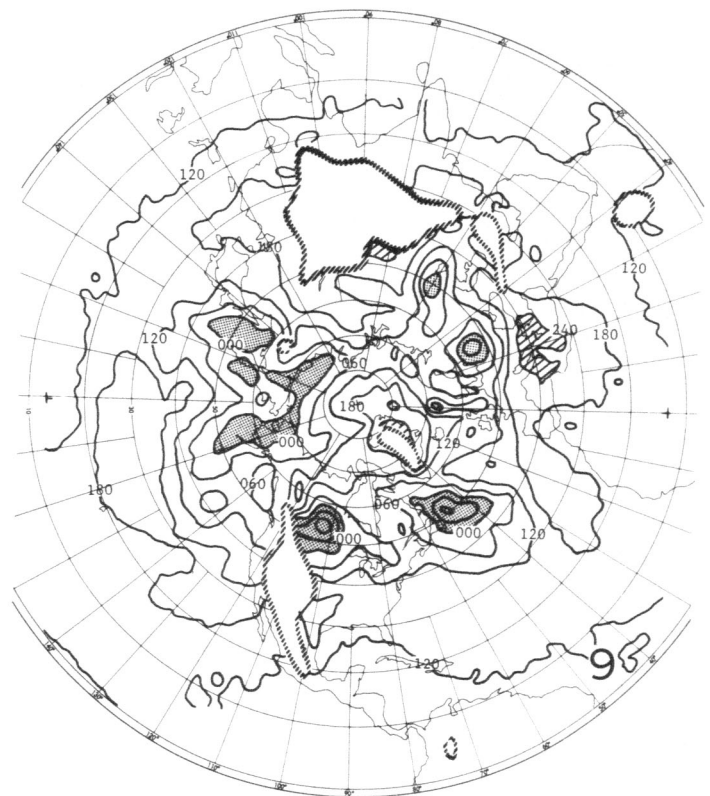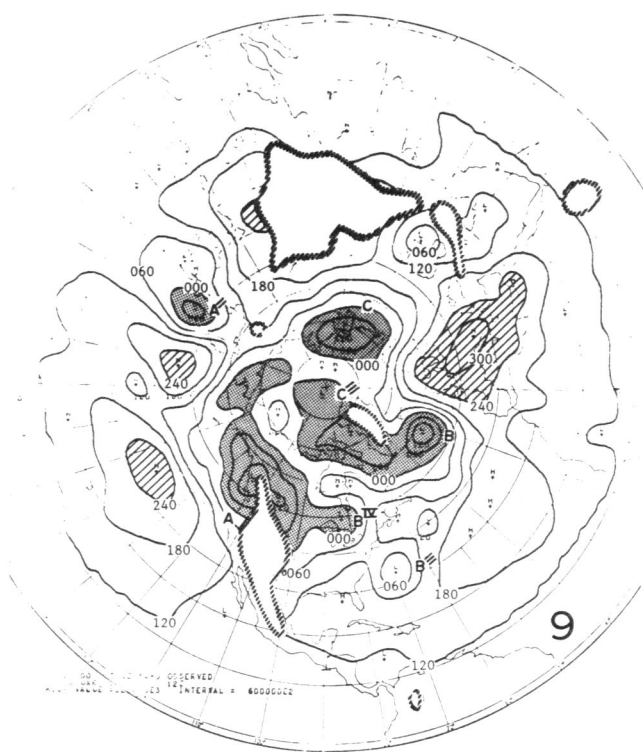
FIGURE 49.—Continued
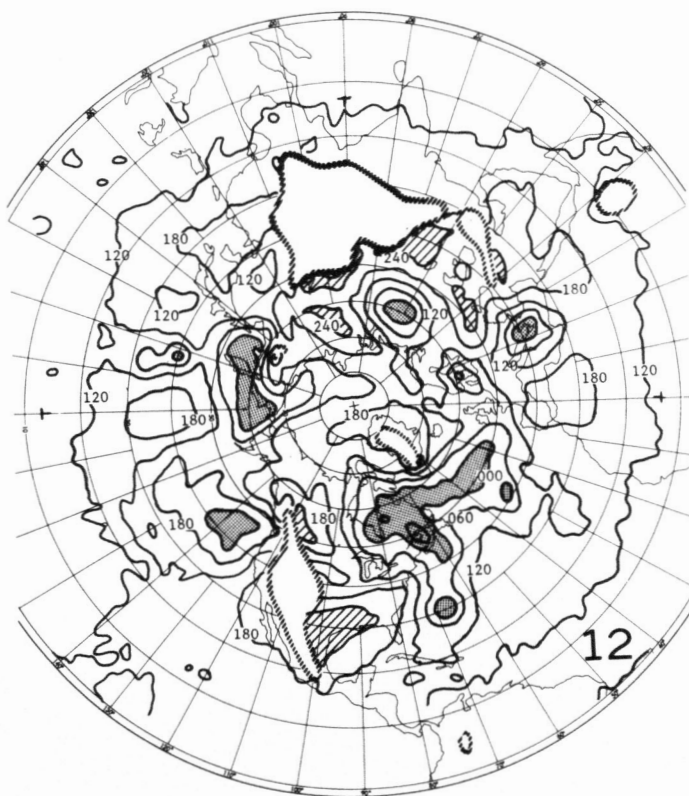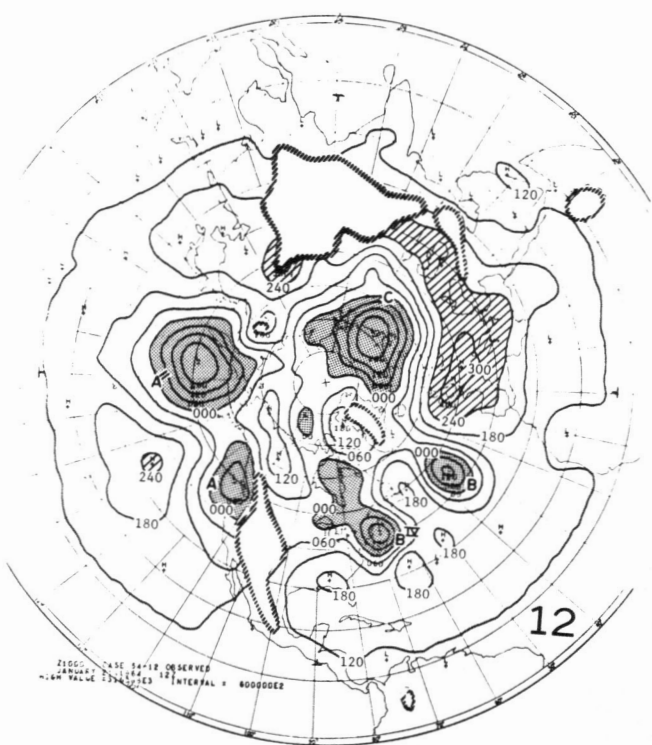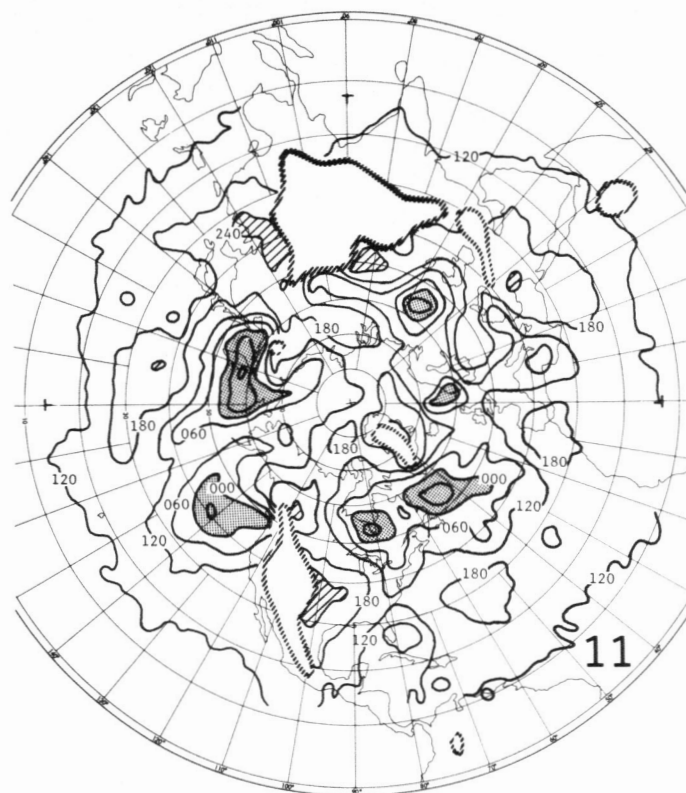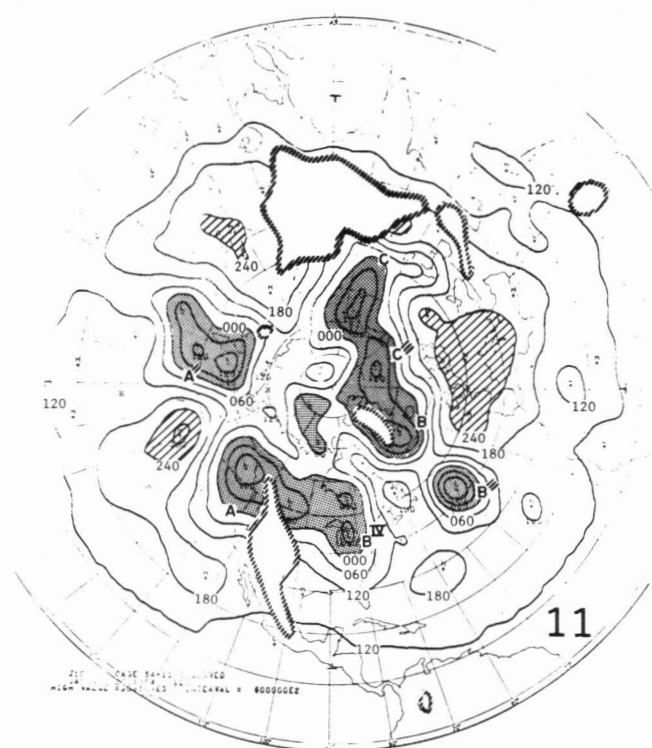
FIGURE 49.—Continued
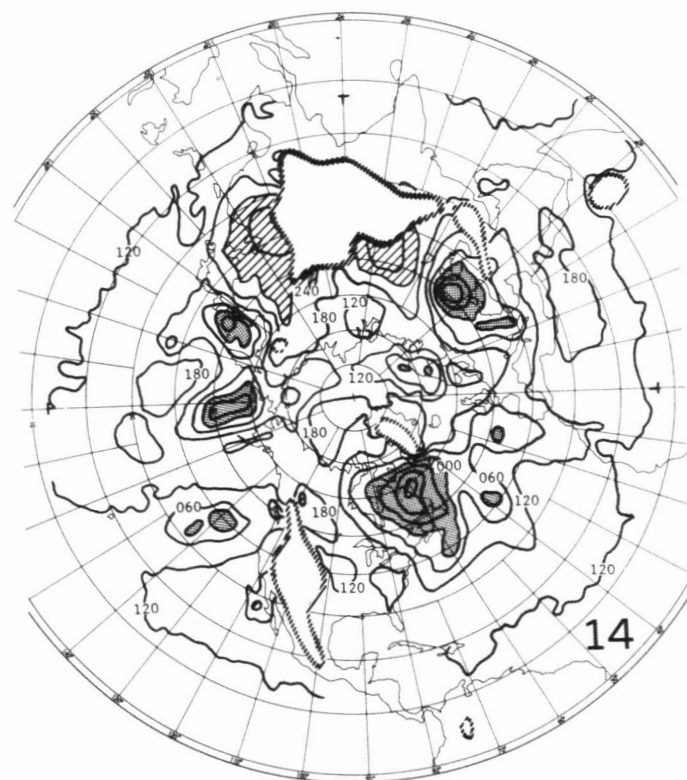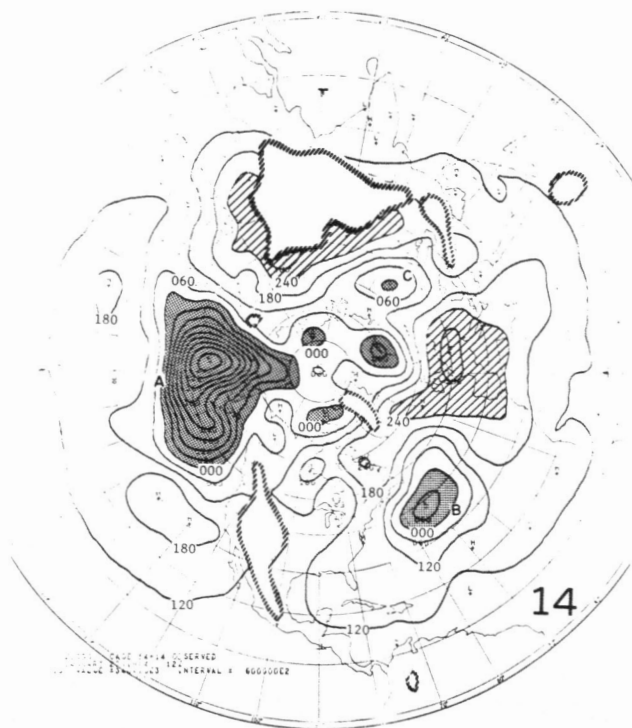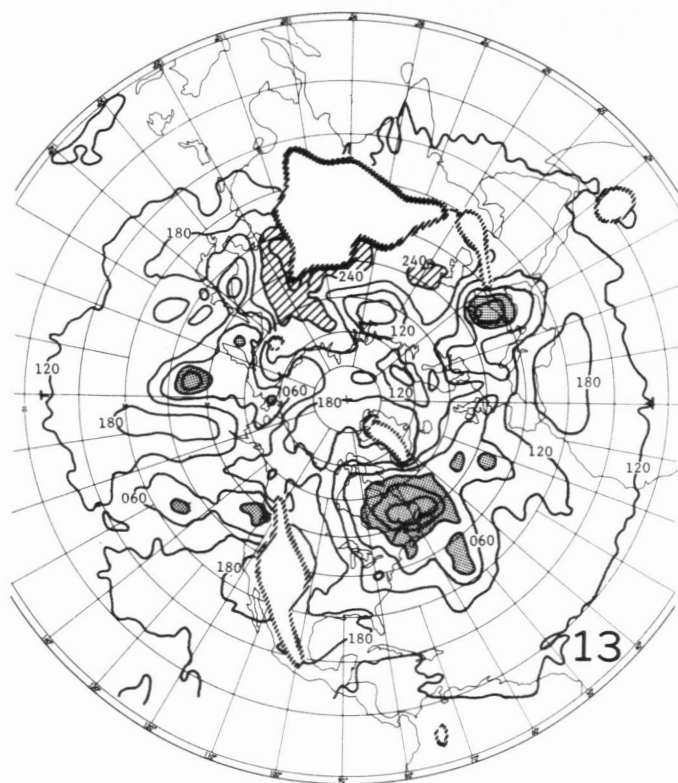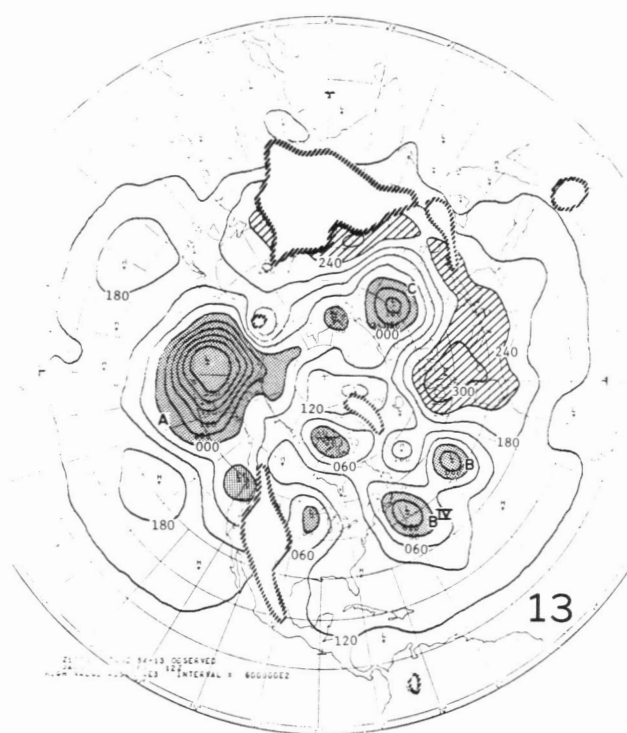
FIGURE 49.—Concluded
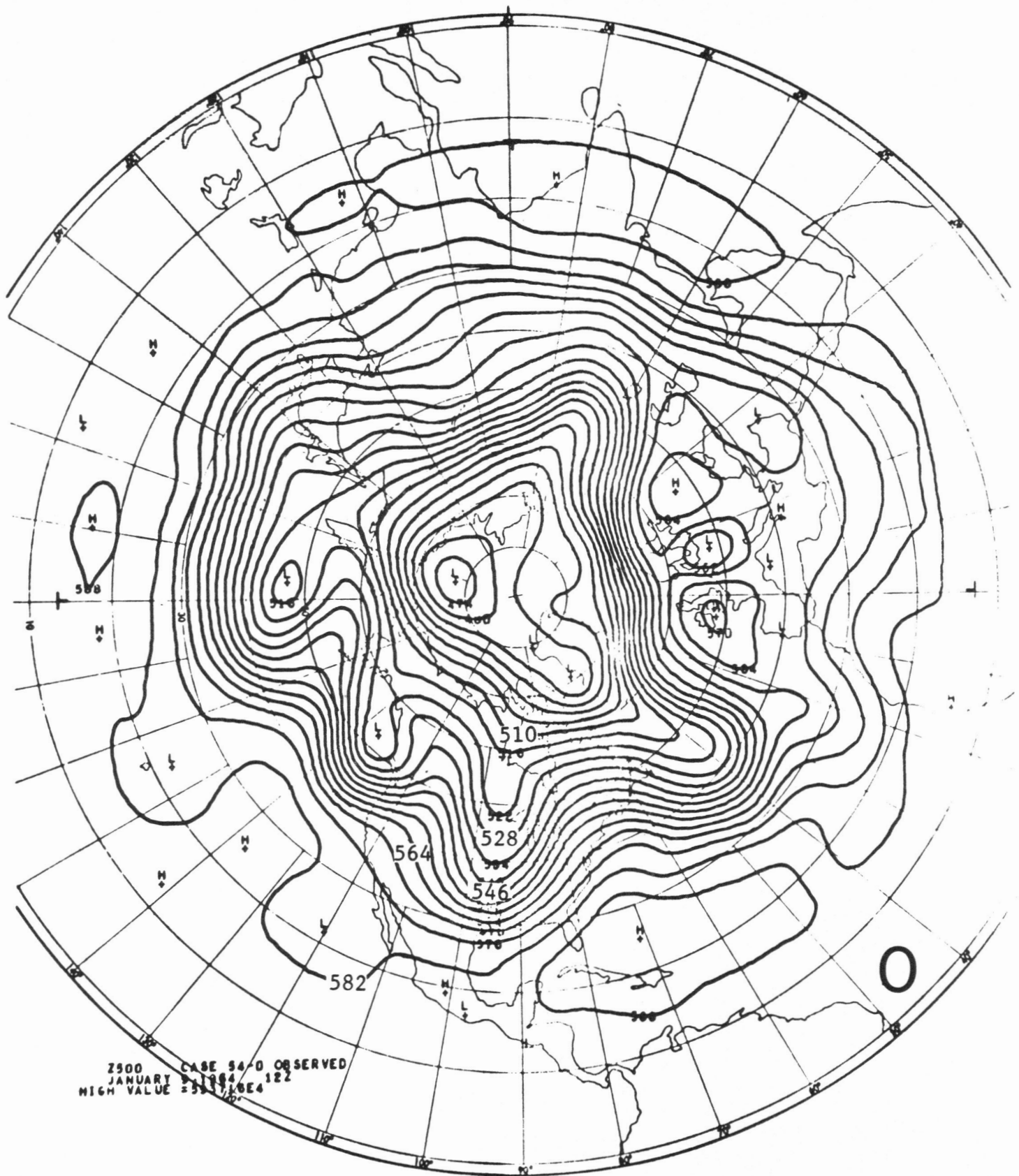
FIGURE 50.—The observed (0 day and left columns) and Experiment 3 (right columns) 500-mb geopotential height for every other day for 2 weeks commencing Jan. 9, 1964, in units of decameters. The contour interval is 60 m. The number in the lower right corner is the day of the forecast.
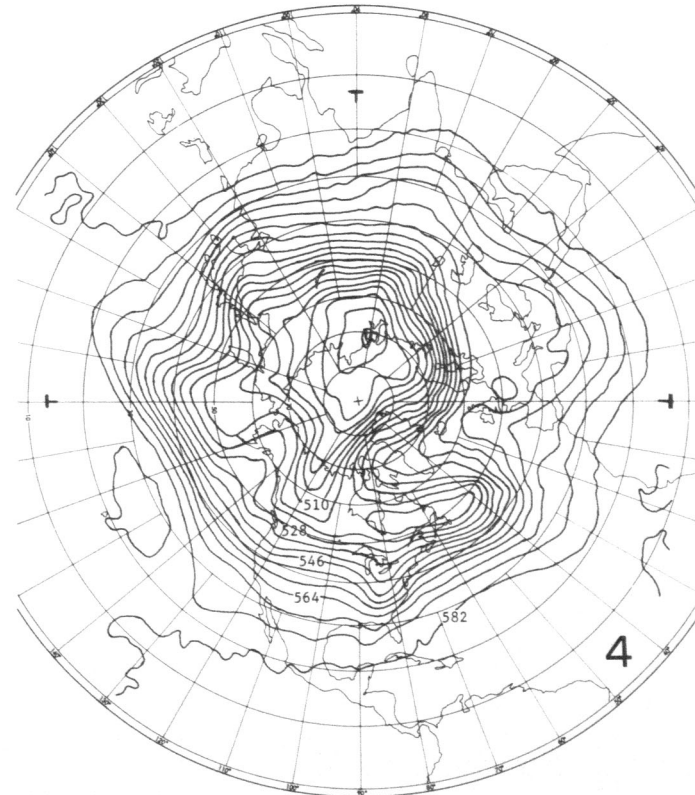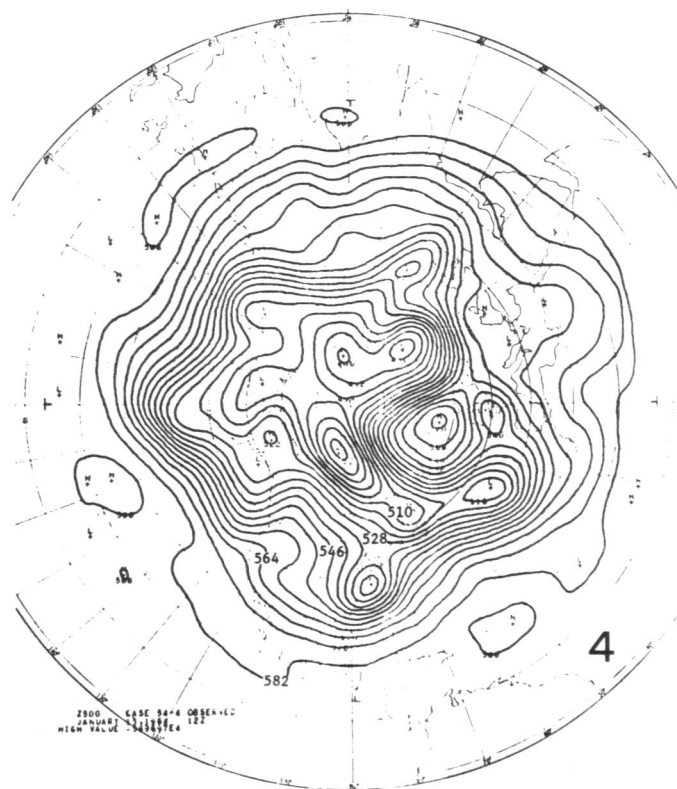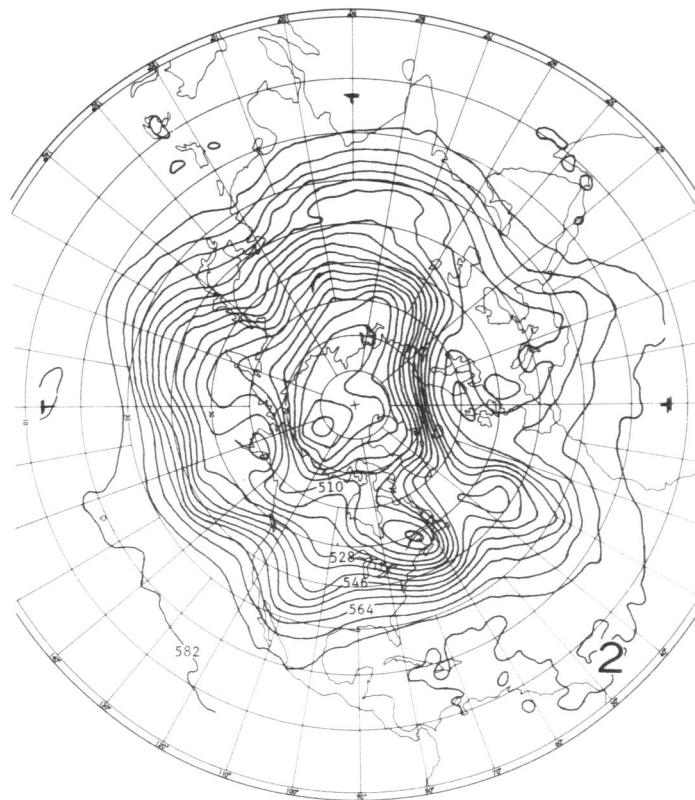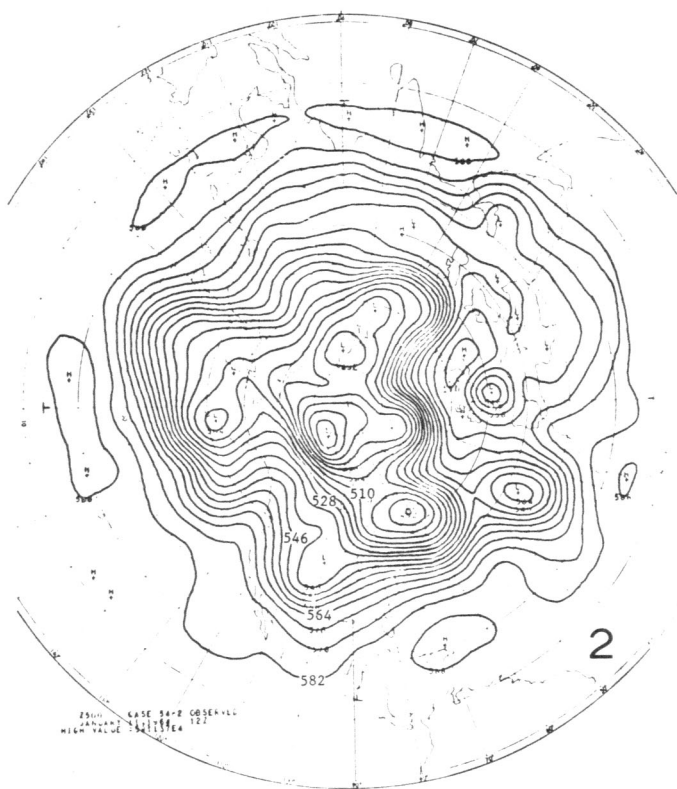
FIGURE 50.—Continued
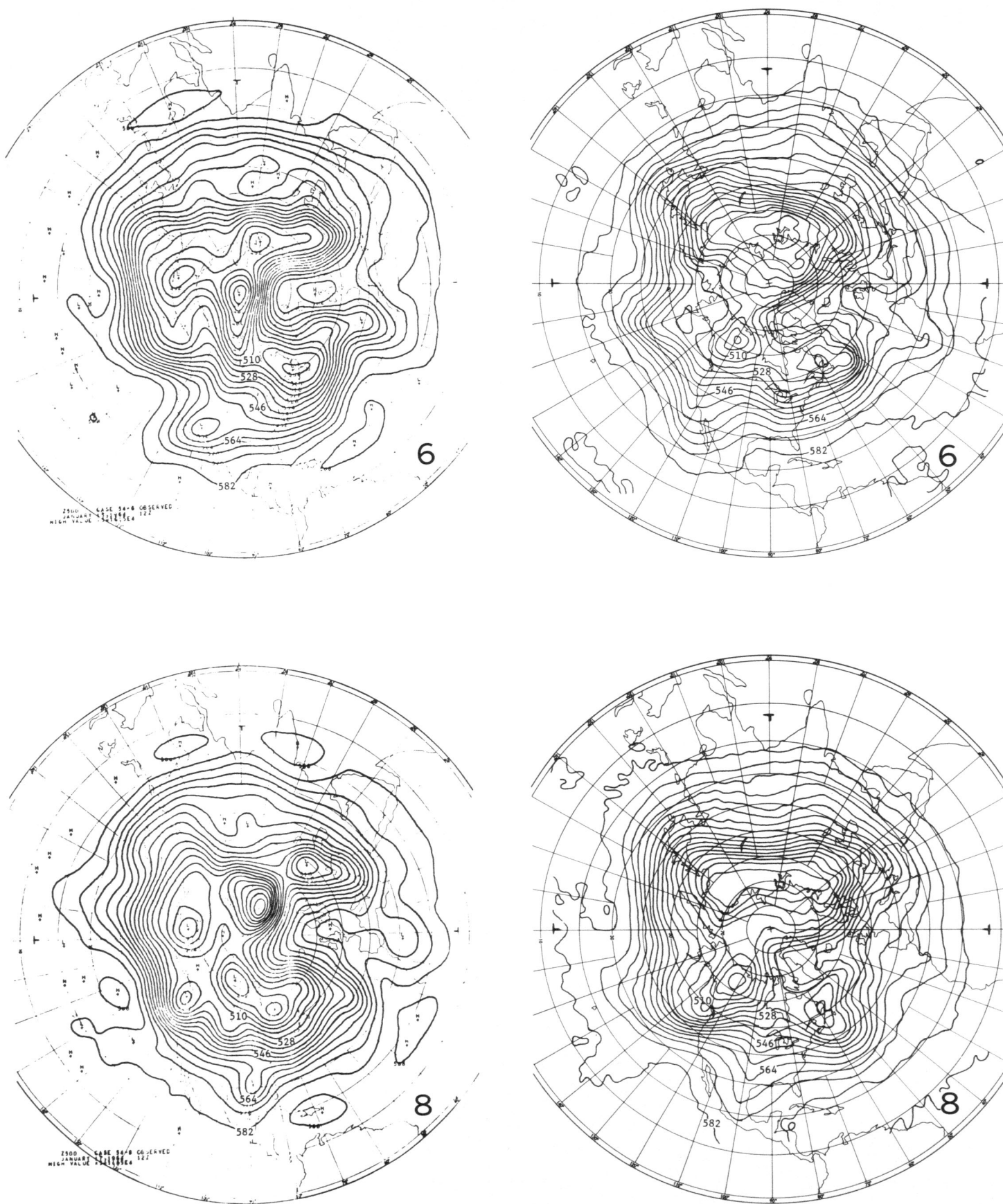
FIGURE 50.—Continued
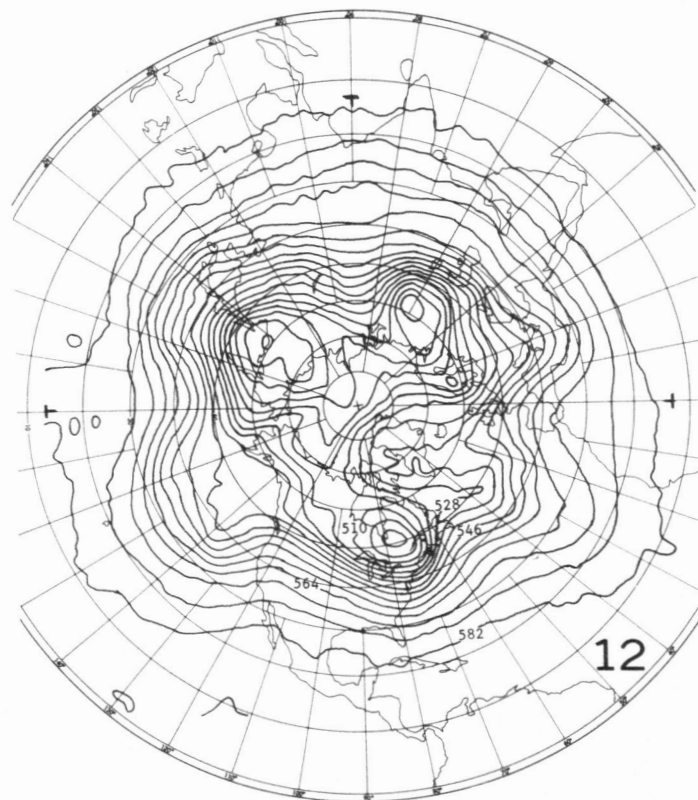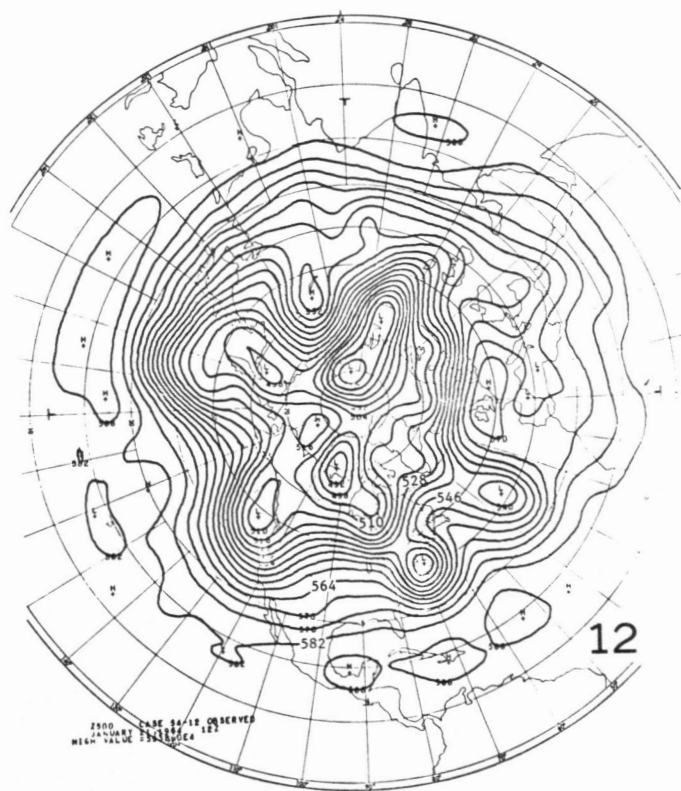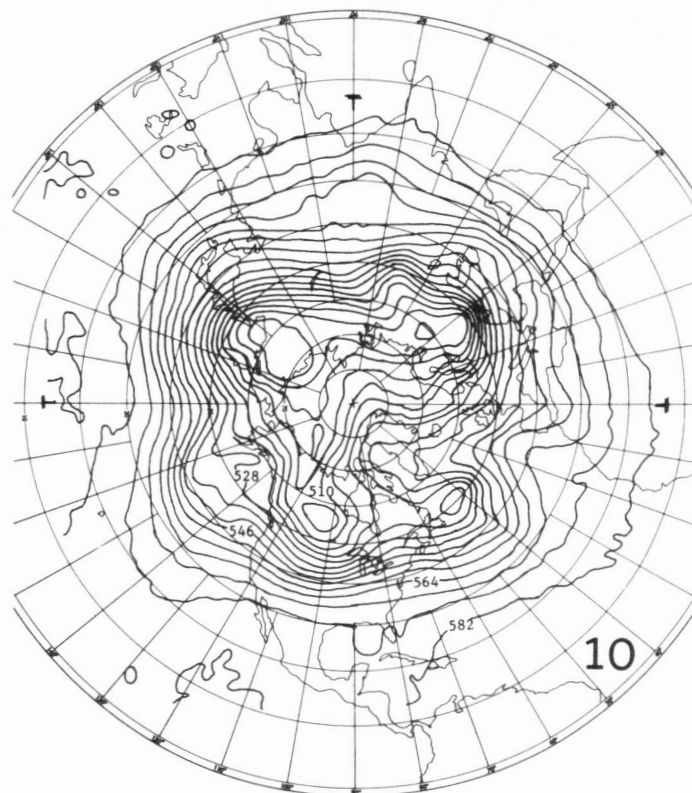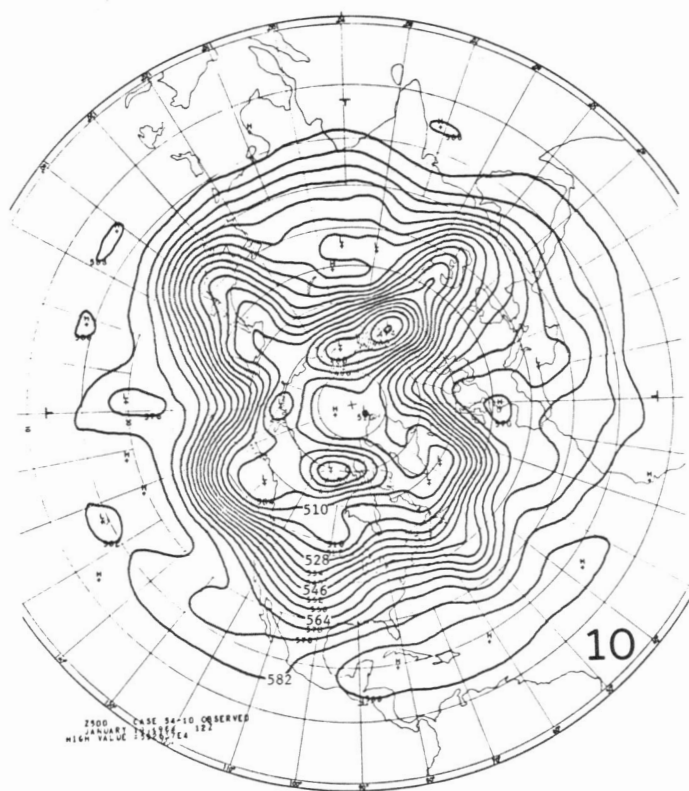
FIGURE 50.—Continued
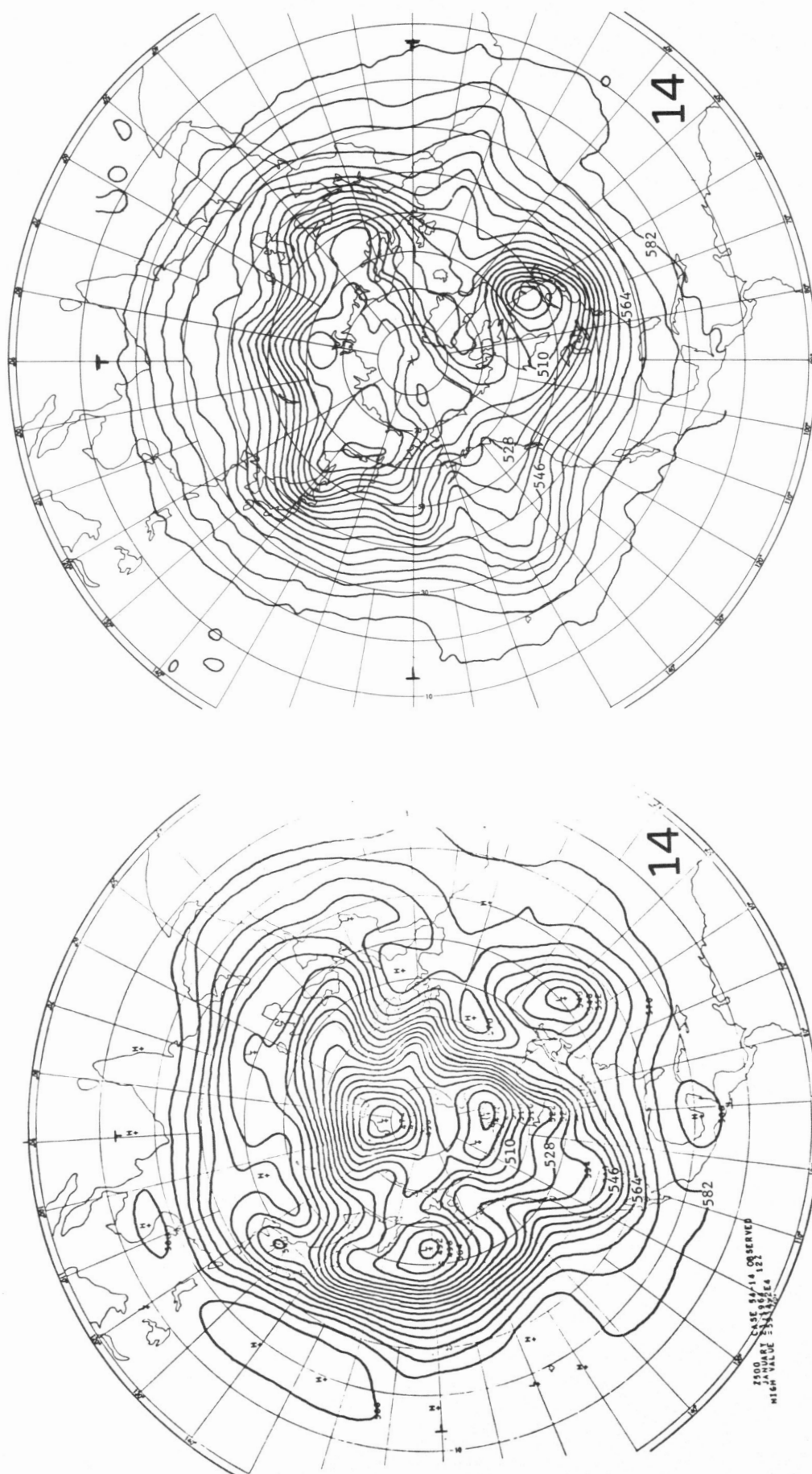
FIGURE 50.—Concluded
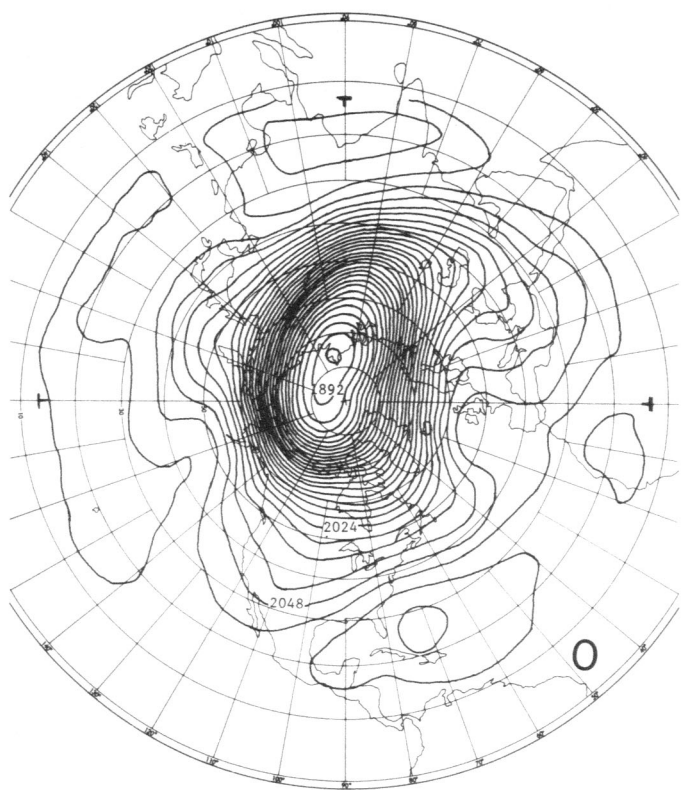
FIGURE 51.—The observed (left columns) and Experiment 3 (right columns) 50-mb geopotential height for 2 weeks commencing Jan. 9, 1964, in units of decameters. The contour interval is 60 m.
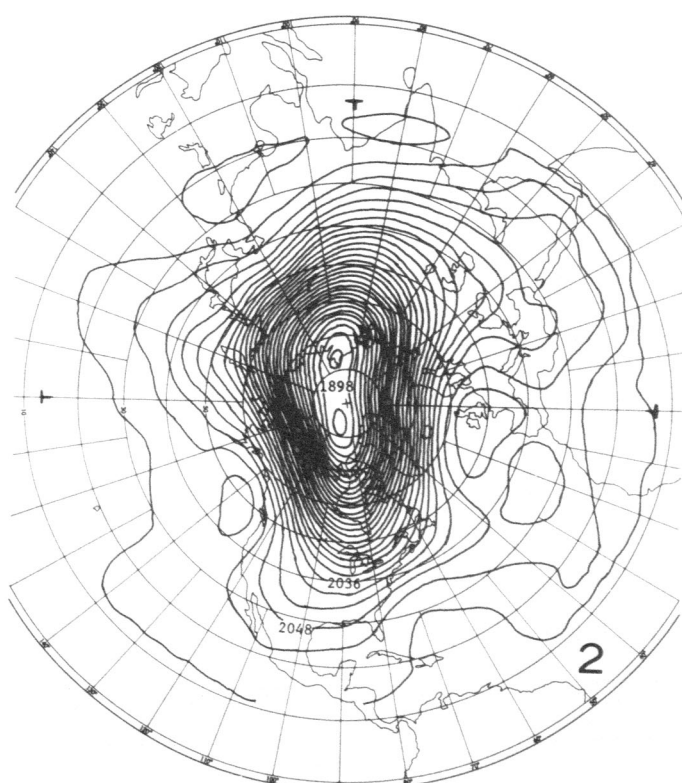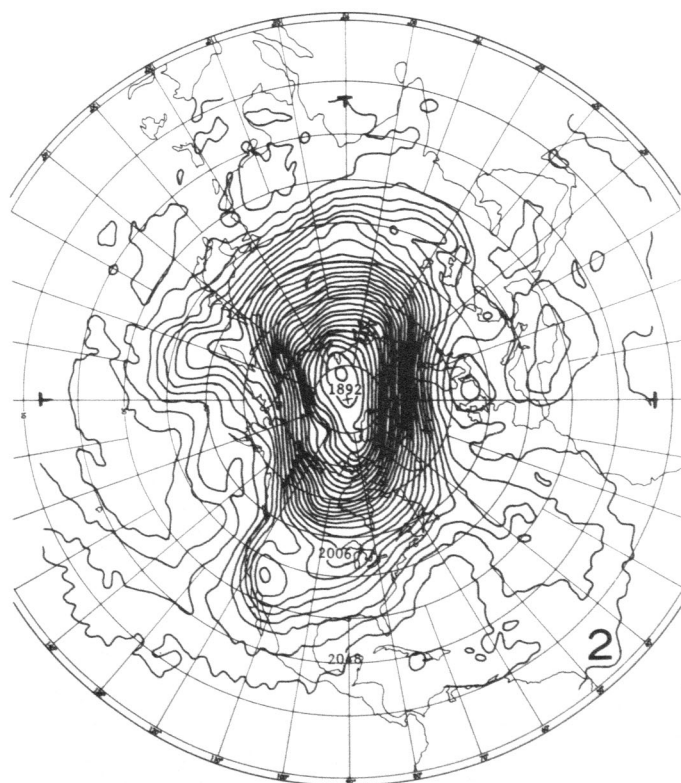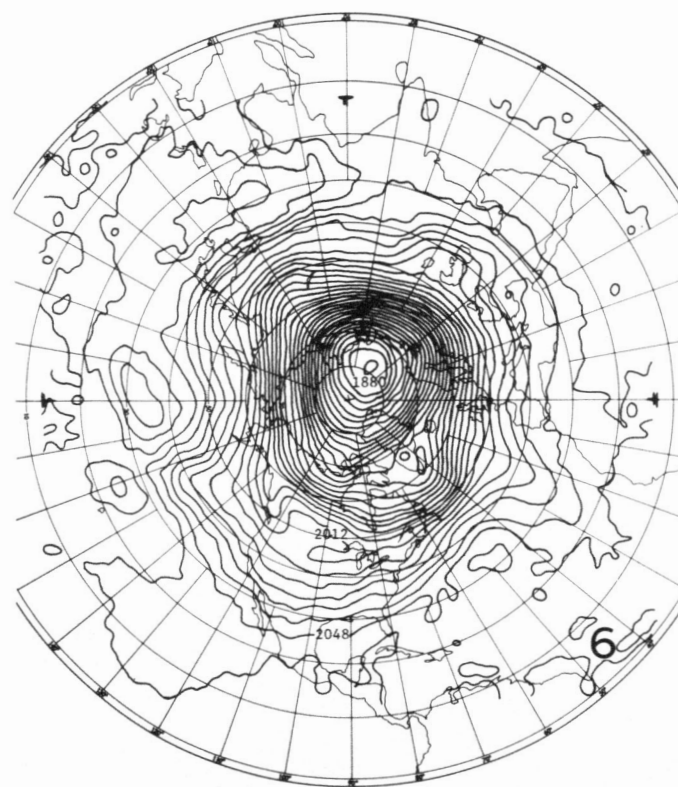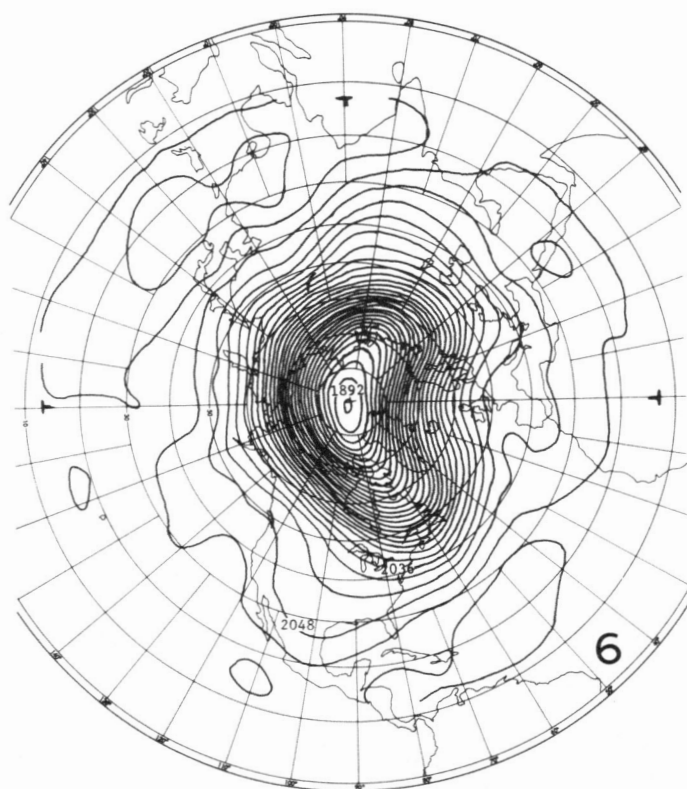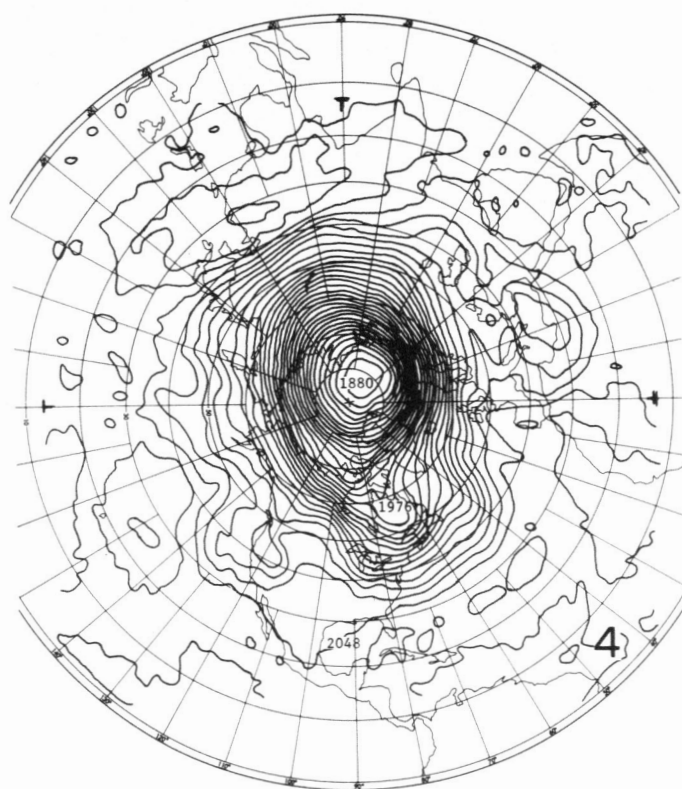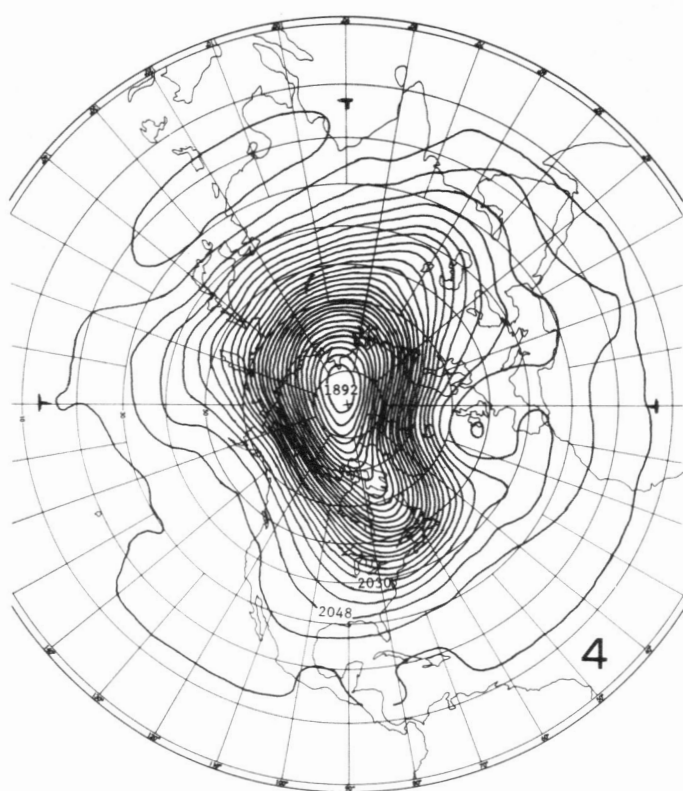
FIGURE 51.—Continued

FIGURE 51.—Continued
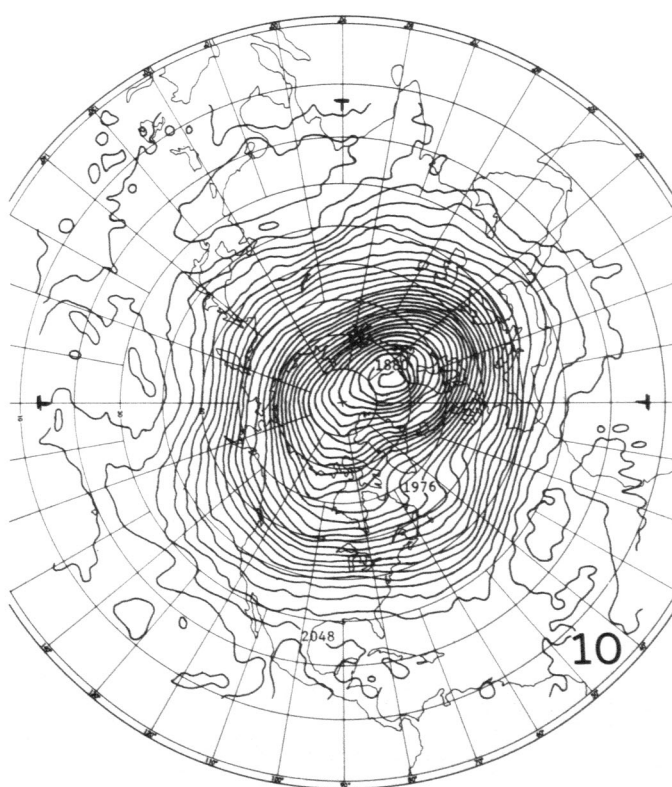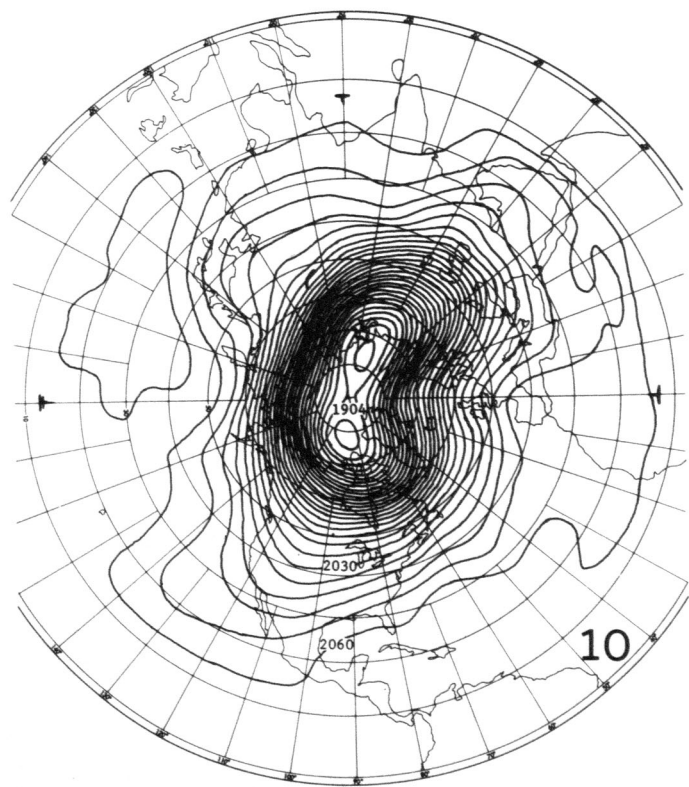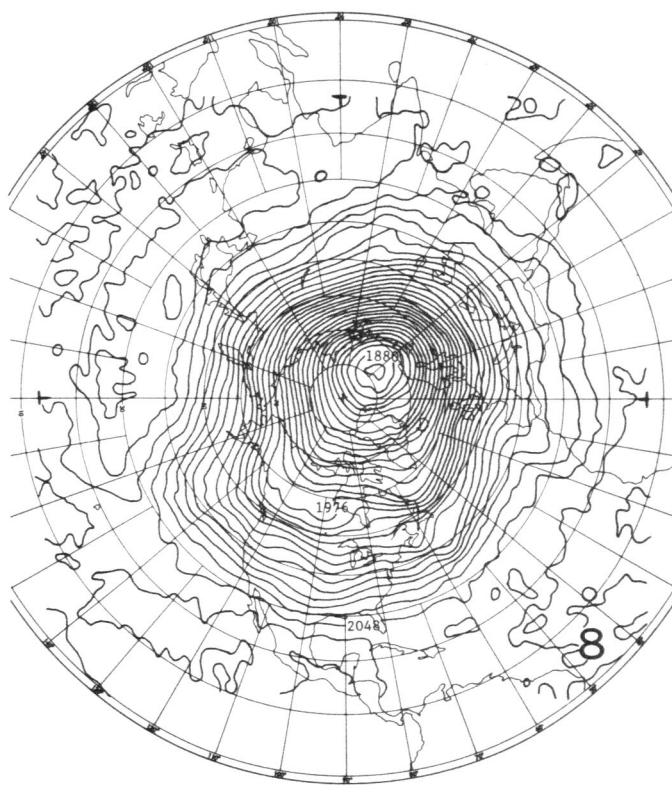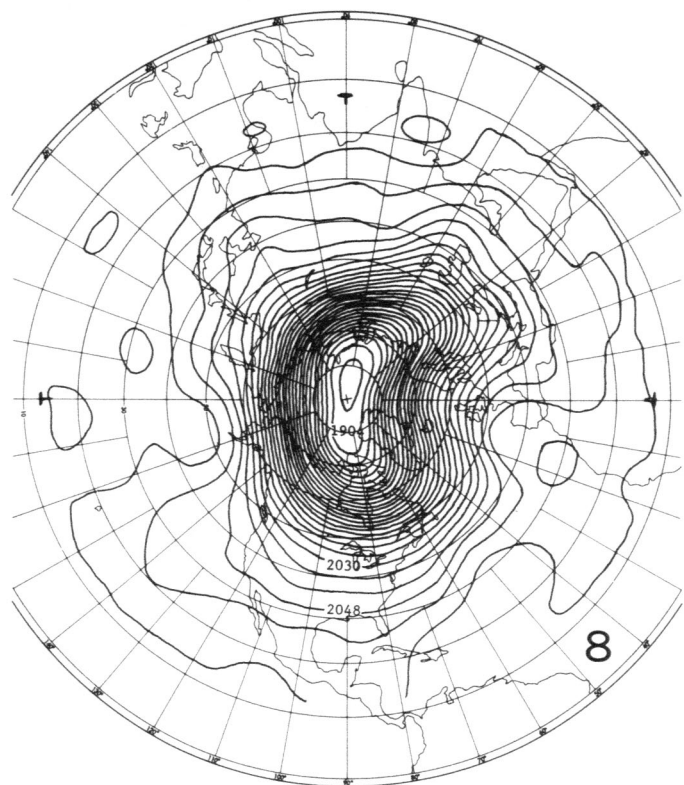
FIGURE 51.—Concluded

TIME VARIATION OF THE LATITUDINAL DISTRIBUTION OF 1000-MB GEOPOTENTIAL HEIGHT
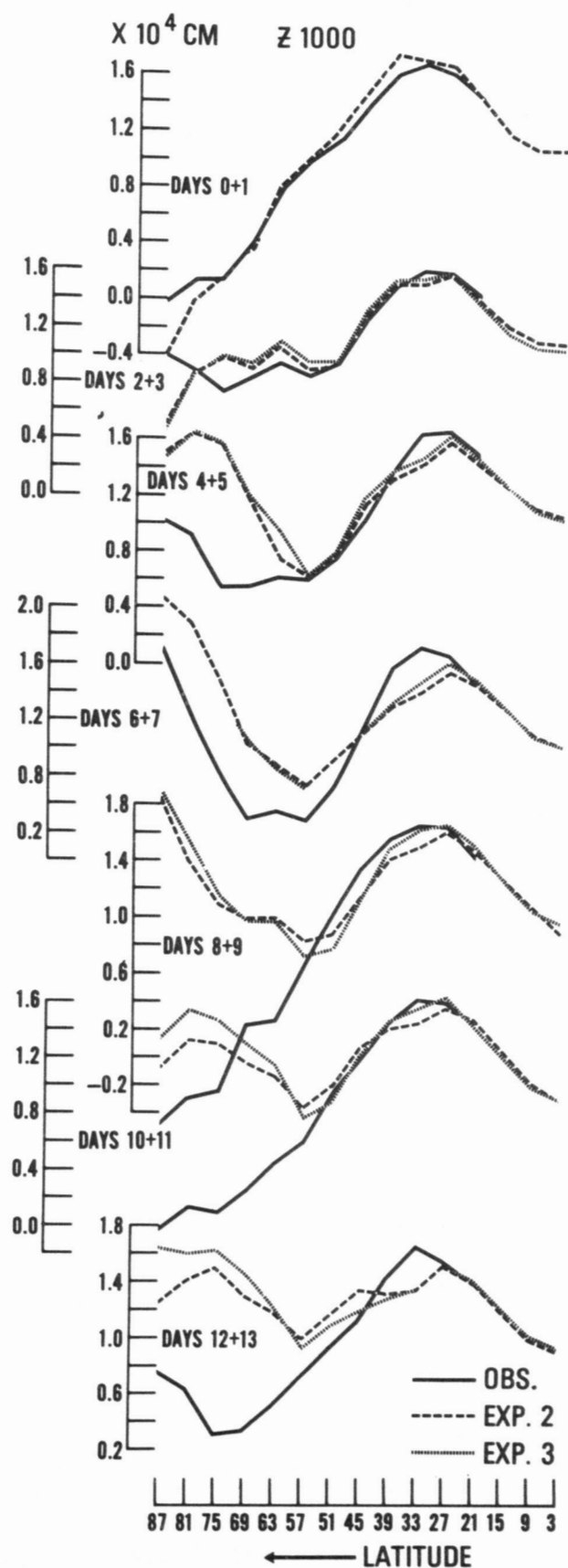
FIGURE 52.—Latitudinal distribution of 1000-mb geopotential height for the observed (solid lines), Experiment 2 and Experiment 3 for the 1964 case. Zonal averages and 2-day averages were taken. The computed results deviated largely from the observation especially at high latitudes.

PRECIPITATION OVER THE UNITED STATES
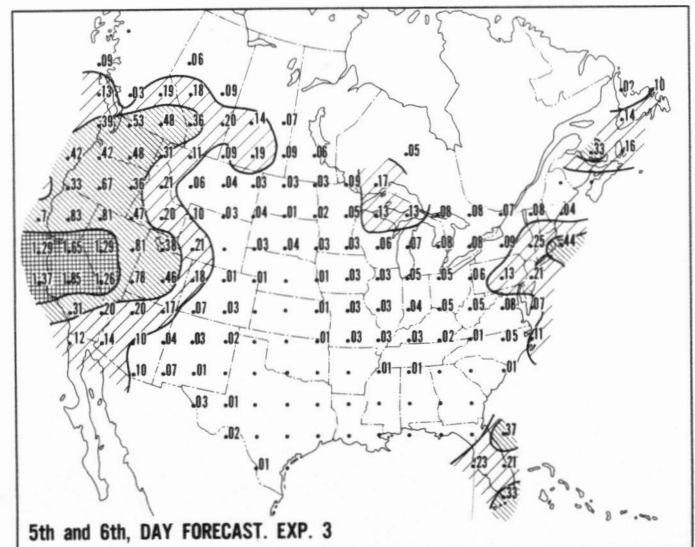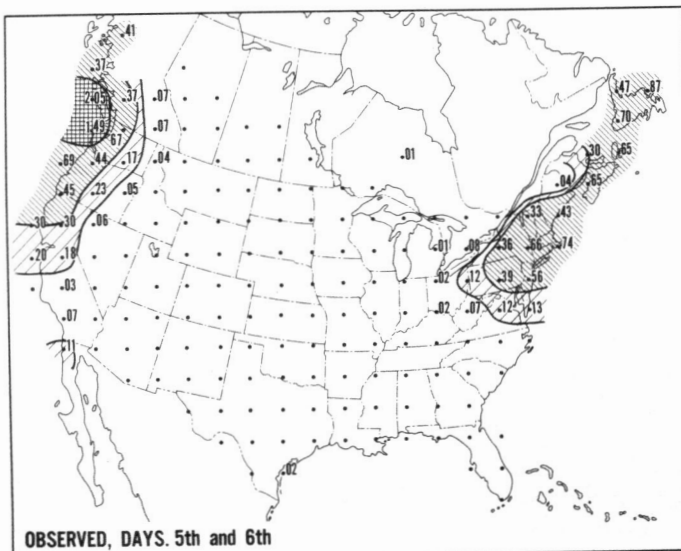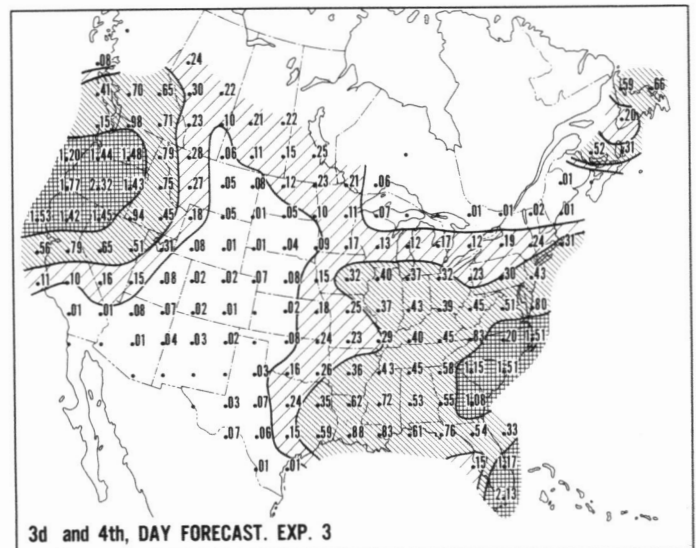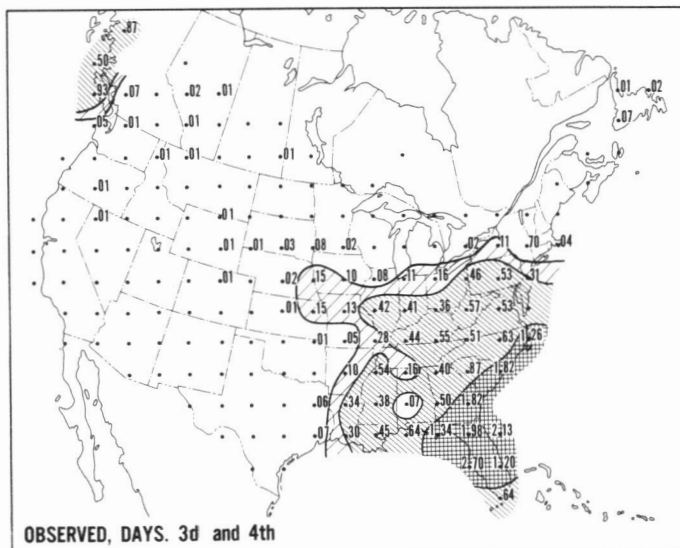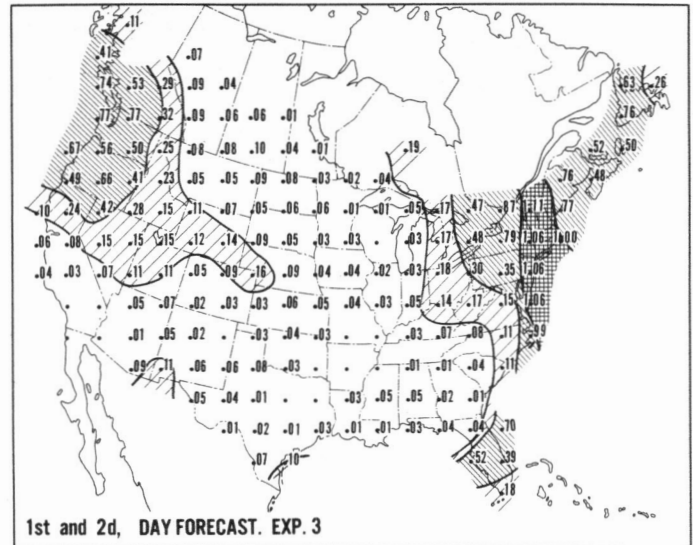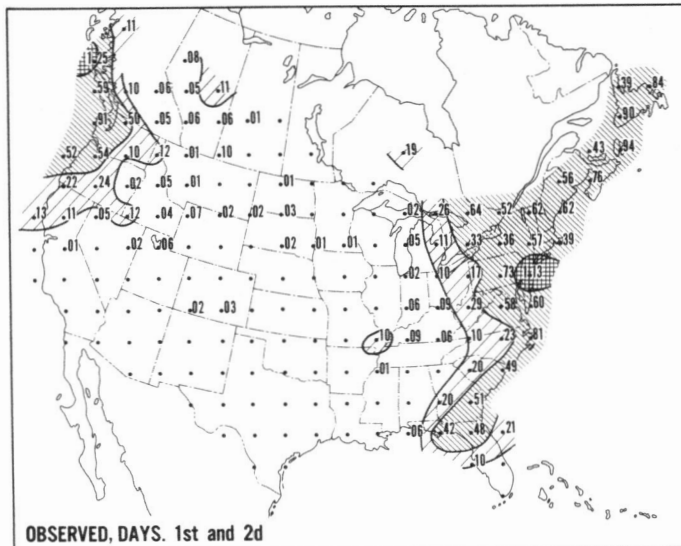
FIGURE 53.—Two-day accumulations of precipitation over the United States and part of Canada. The units are inches. The contours are at 0.1, 0.3, and 1.0 in. The dots are the gridpoints used for computation. Left columns, the observed, and right columns, Experiment 3, for the 1964 case.
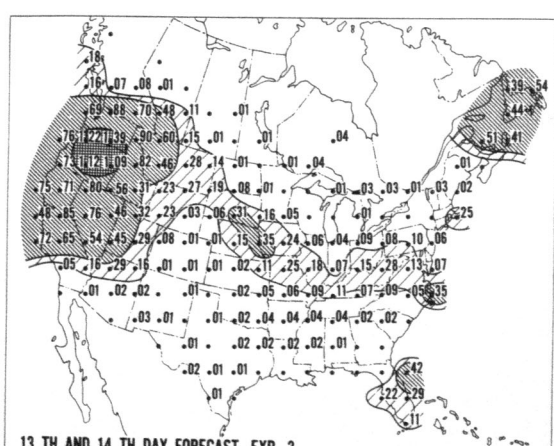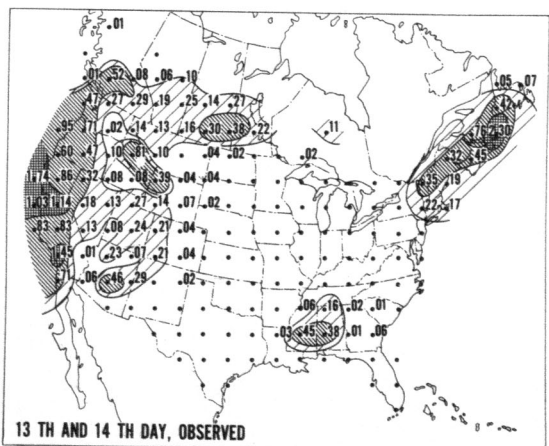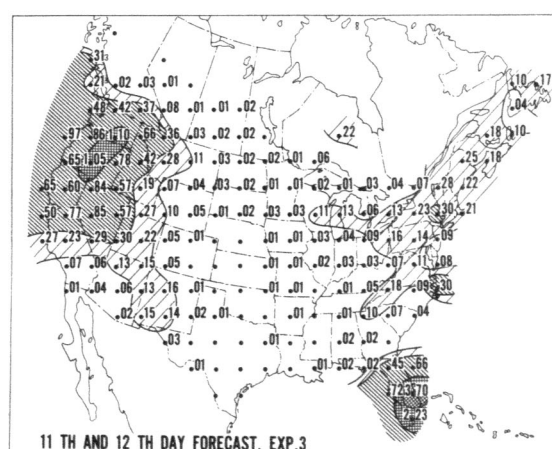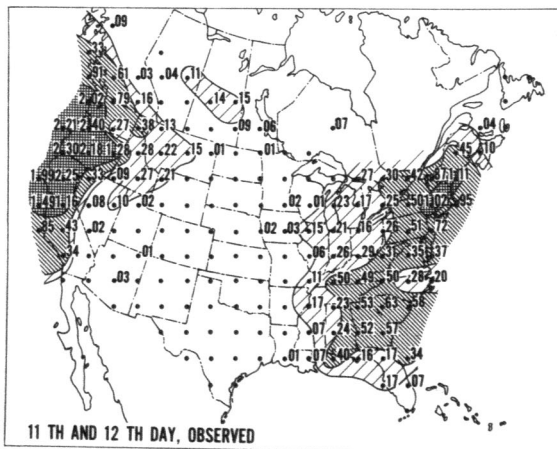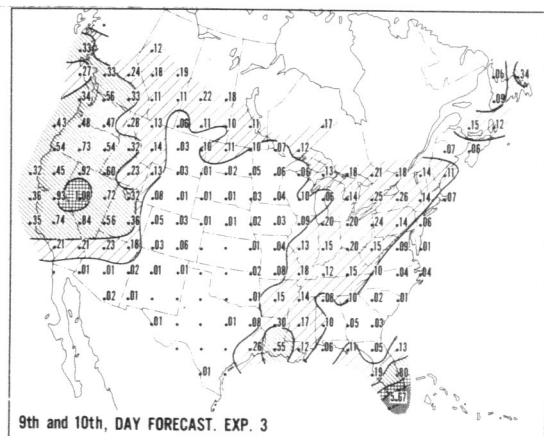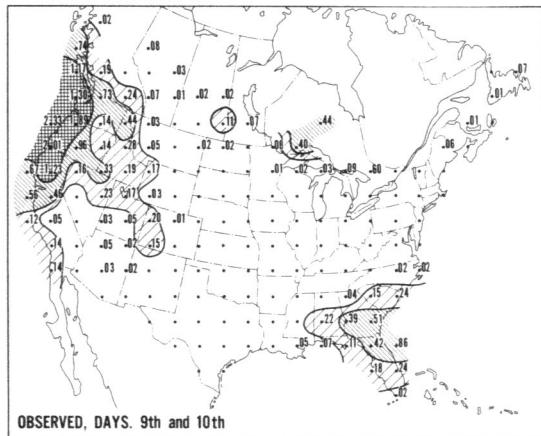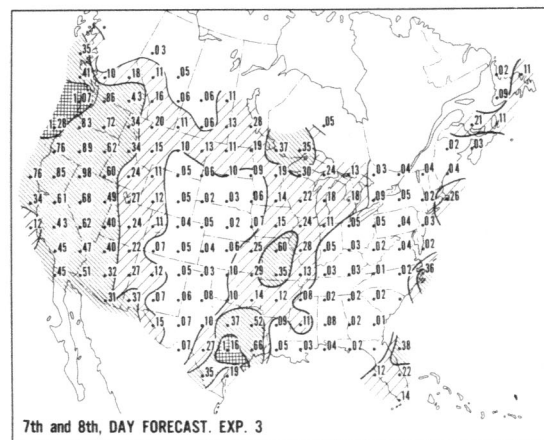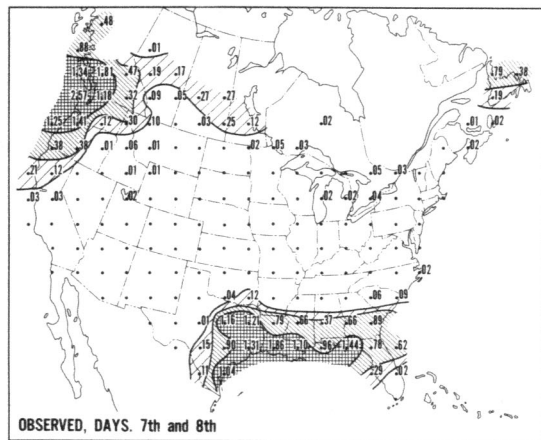
FIGURE 53.—Concluded

MERIDIONAL SECTION (EXPERIMENT 3)

Refer to section 10. The predictions are averaged for the period 4 to 14 days and the observed data for the period 0 to 14 days. The results for Experiment 3 are shown here.
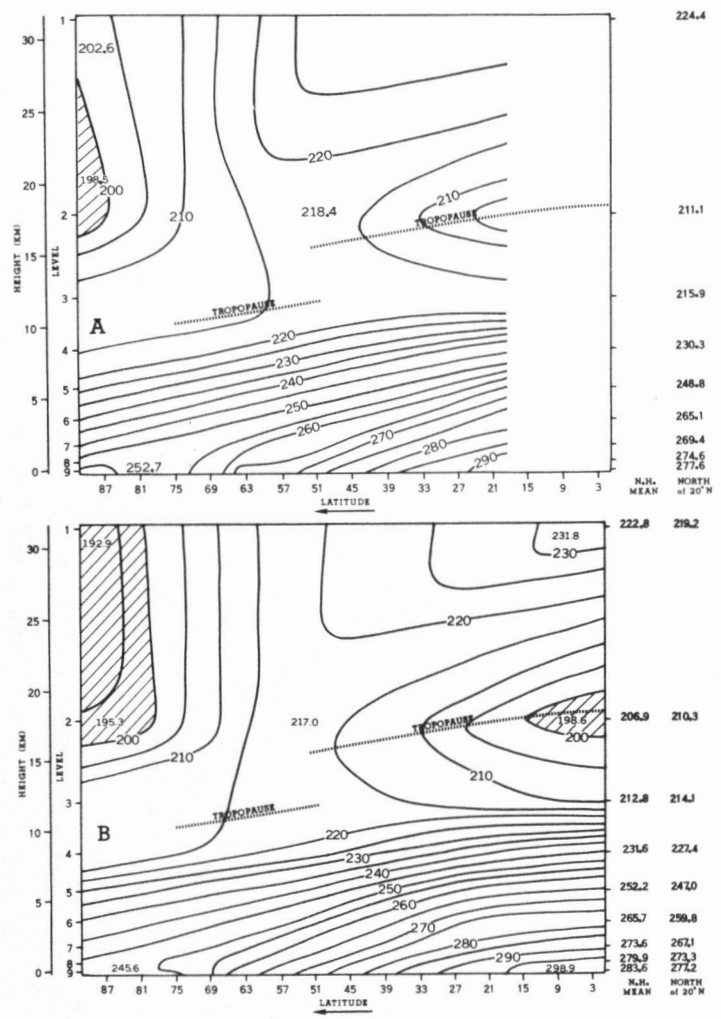
FIGURE 54.—Temperature $\overline{T}$ in units of °K. (A) the observed, and (B) the prediction.
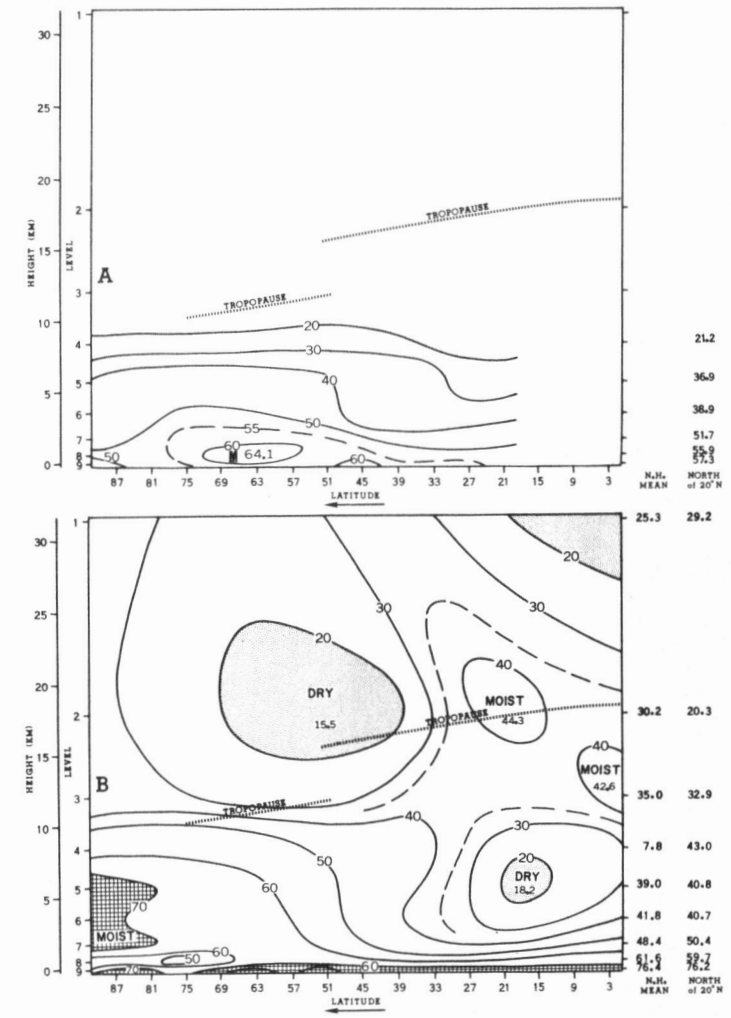
FIGURE 55.—Humidity $\overline{h}$ in units of percent. (A) the observed, valid between 850 and 500 mb, and (B) the prediction. In this experiment, the initial humidity above 300 mb was assumed to be 10%. It was noticed that the water vapor in the stratosphere is well maintained once it is there. So the initial stratospheric humidity above the tropopause in the prediction is too high. See the more reasonable result of the 1966 case (fig. 73) in which the initial stratospheric humidity was assumed to be 0%.
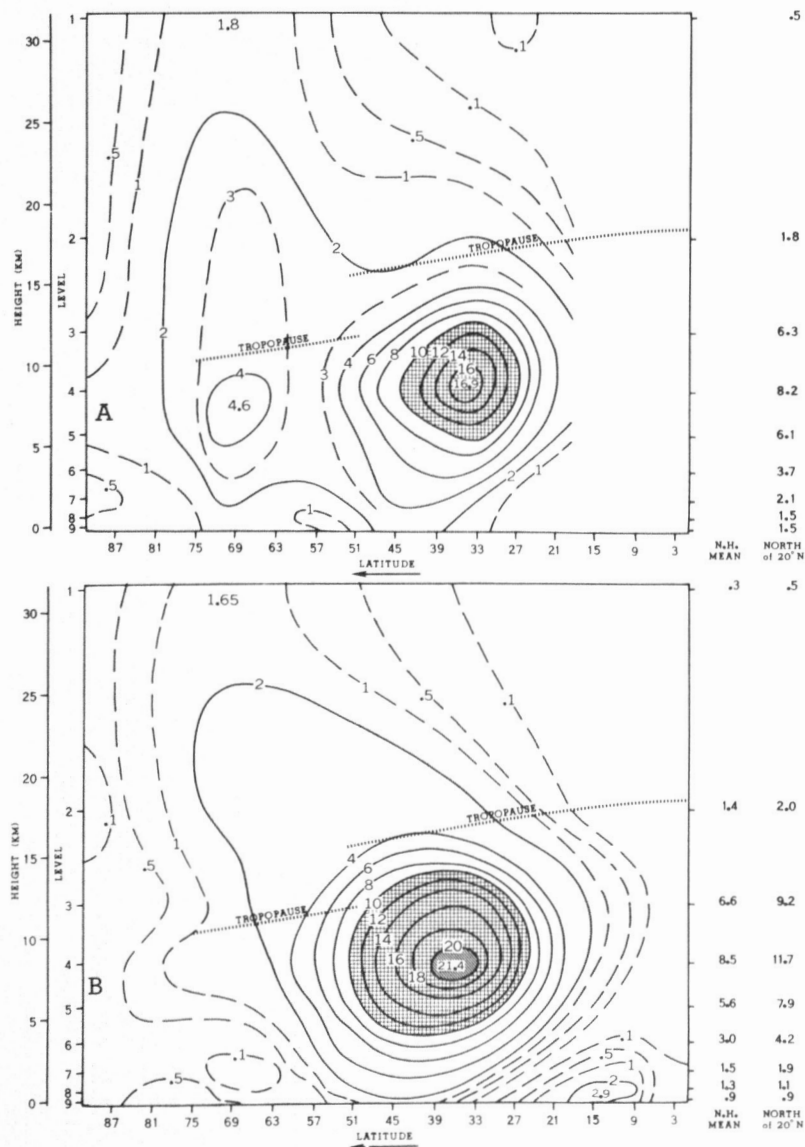
FIGURE 56.—Zonal kinetic energy ρKz, where $Kz = (\overline{u^2 + v^2})/2$ in units of 10^2 ergs/cm³. (A) the observed, and (B) the prediction. As mentioned, the computed zonal kinetic energy is larger than the observed.
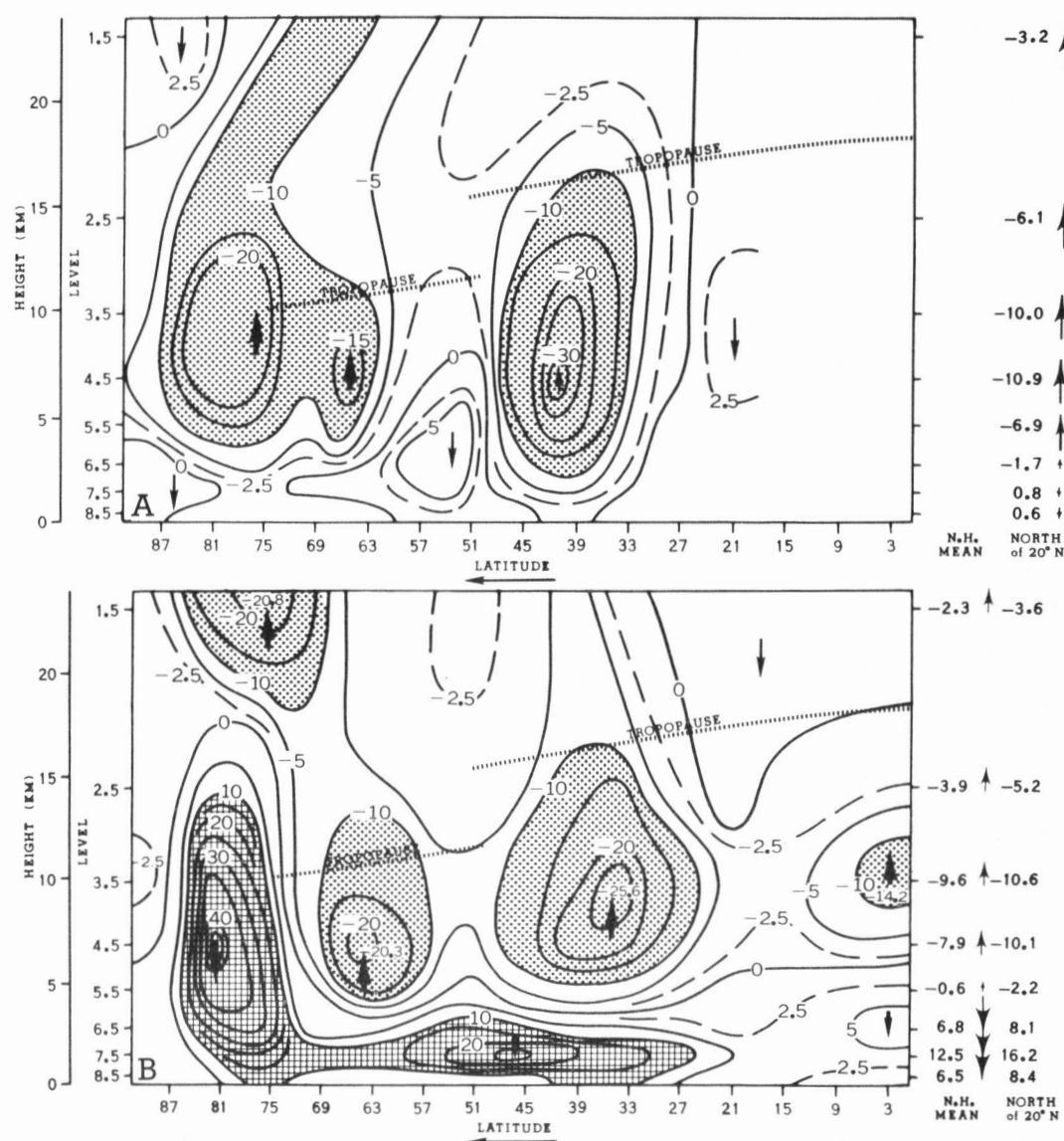
FIGURE 57.—Vertical flux of geopotential height by eddies $\overline{\omega'\phi'}$ in units of 10^2 gm sec⁻³. (A) from the ω-equation, and (B) the prediction. This quantity indicates the vertical redistribution of eddy kinetic energy. The arrows show the direction of propagation.
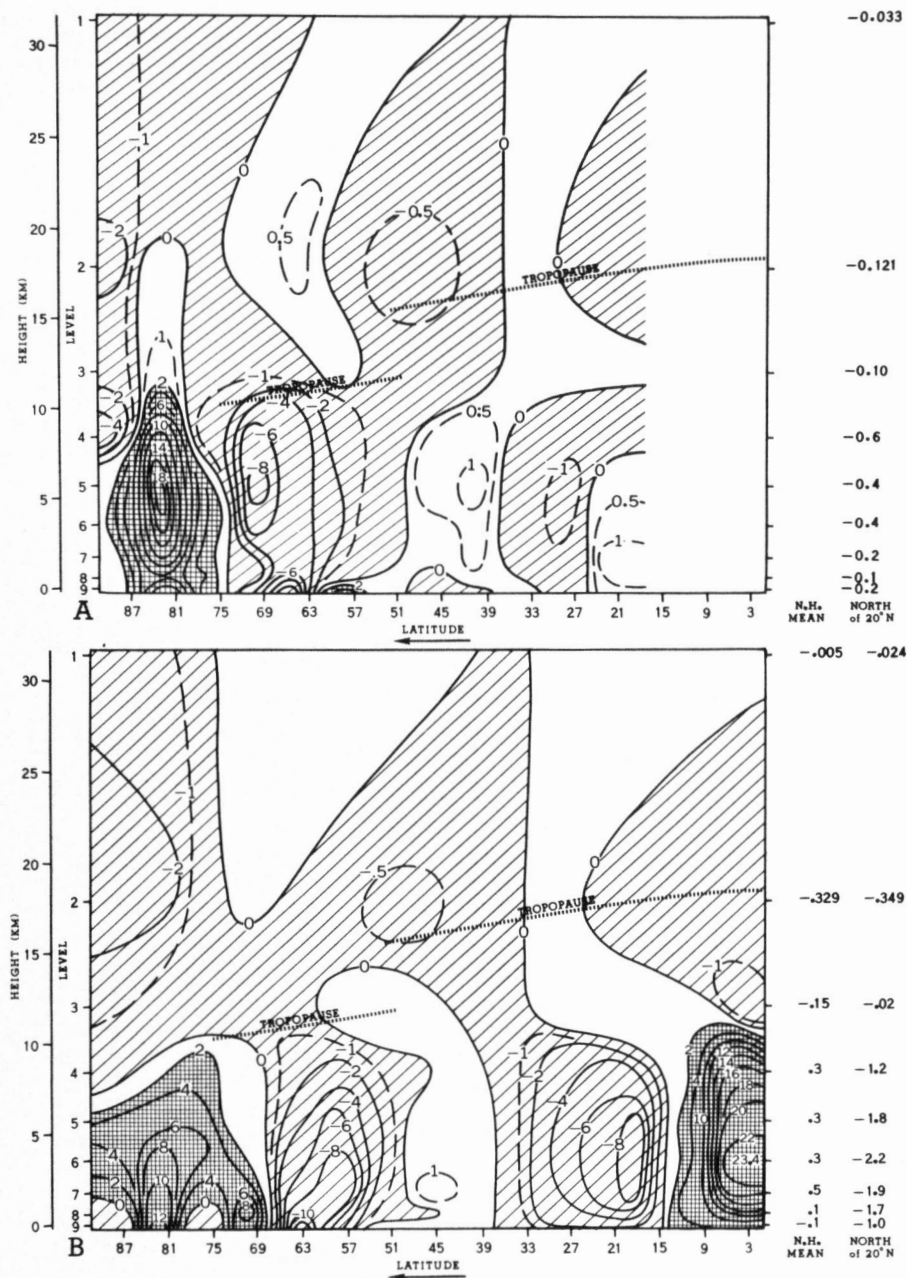
FIGURE 58.—Conversion of zonal available potential energy to zonal kinetic energy $-\rho\overline{\omega}\cdot\overline{\alpha}$ in units of 10^{-3} ergs cm^{-3}sec^{-1}, where $\alpha=1/\rho$. (A) from the ω-equation, and (B) the prediction.
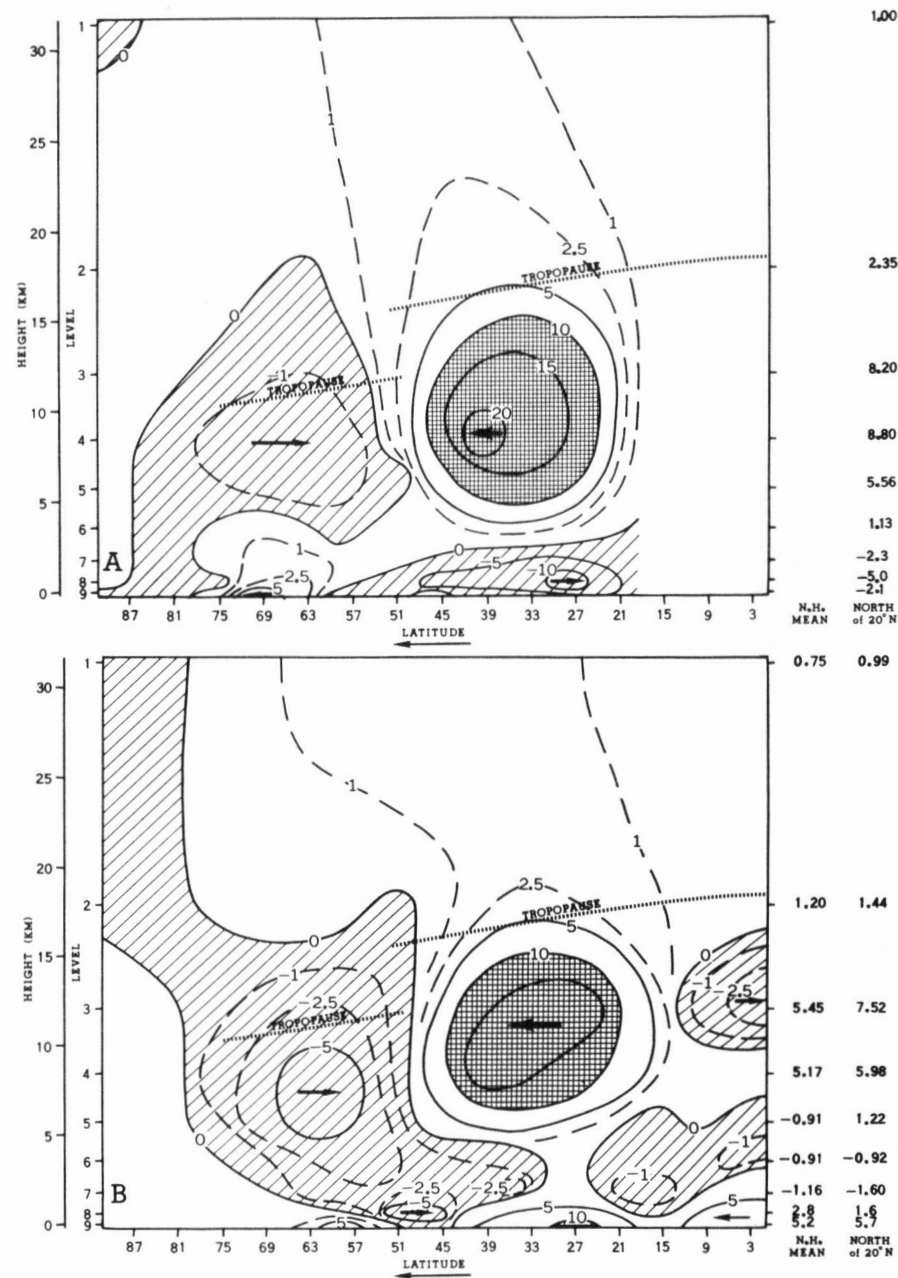
FIGURE 59.—Meridional flux of angular momentum by eddies $\rho\cdot 2\pi a\cdot\cos\varphi\cdot\overline{v'M'_A}$ in units of 10^{19} gm cm sec^{-2}, where M_A is the absolute angular momentum, i.e., $M_A=a\cdot\cos\varphi\cdot(u+a\cdot\cos\varphi\cdot\Omega)$, a is the radius of the earth, Ω is the rate of rotation of the earth. (A) the observed, and (B) the prediction. The negative area is hatched.

FIGURE 61.—Meridional flux of temperature by eddies $\rho \cdot 2\pi a \cdot \cos \varphi \cdot \overline{v'T'}$ in units of 10^{16} ergs cm^{-1} sec^{-1}. (A) the observed, and (B) the prediction. The negative area is hatched.
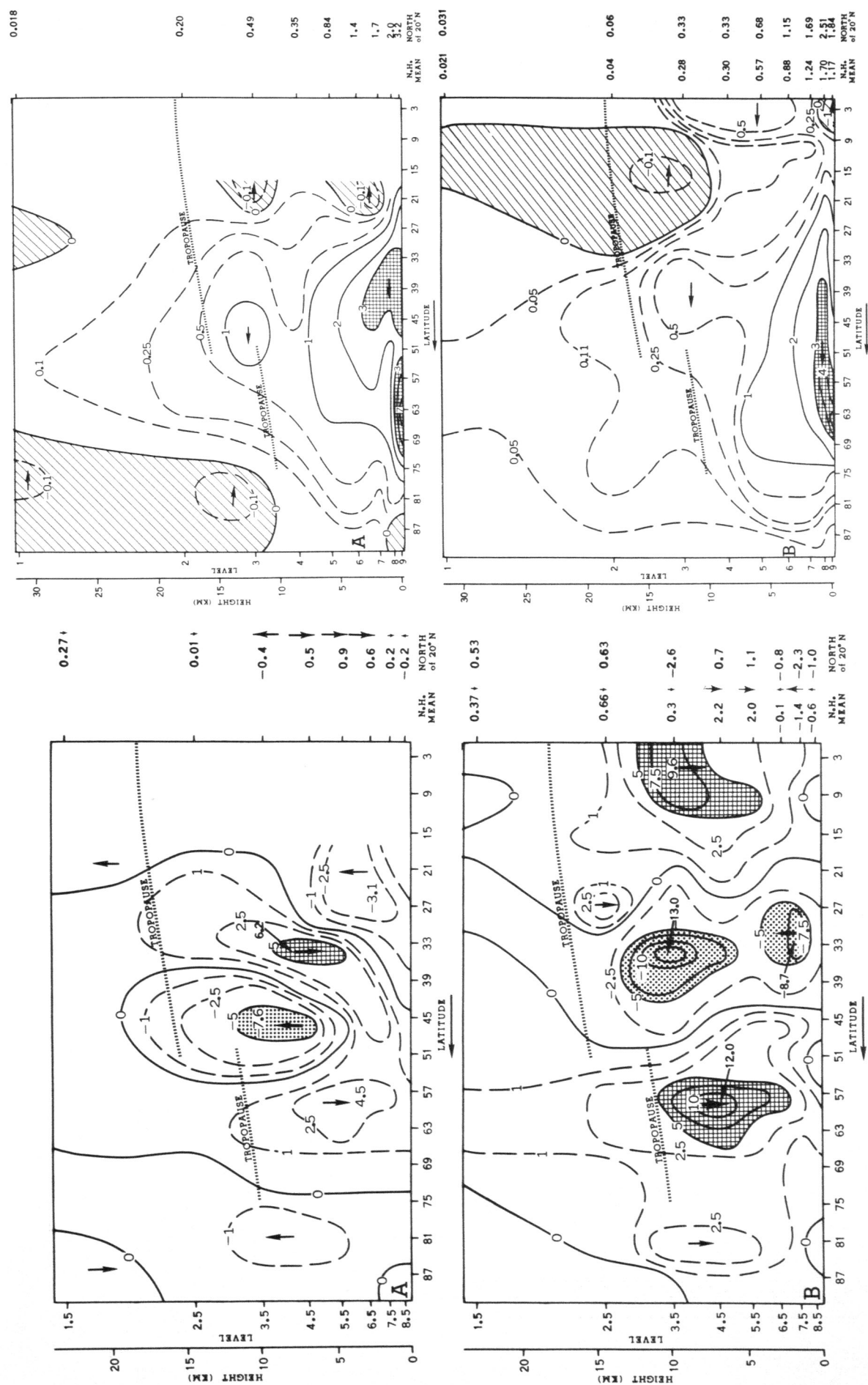
FIGURE 60.—Vertical flux of angular momentum by eddies $\overline{\left(\dfrac{p*\tilde{\omega}}{g}\right)' M_A'}$ in units of 10^7 gm sec^{-2}. (A) from the ω-equation, and (B) the prediction. The arrows show the direction of flux. See figure 59 for M_A, $\tilde{\omega} = d(p/p*)/dt$, $p*$ is the surface pressure, and p is the pressure.
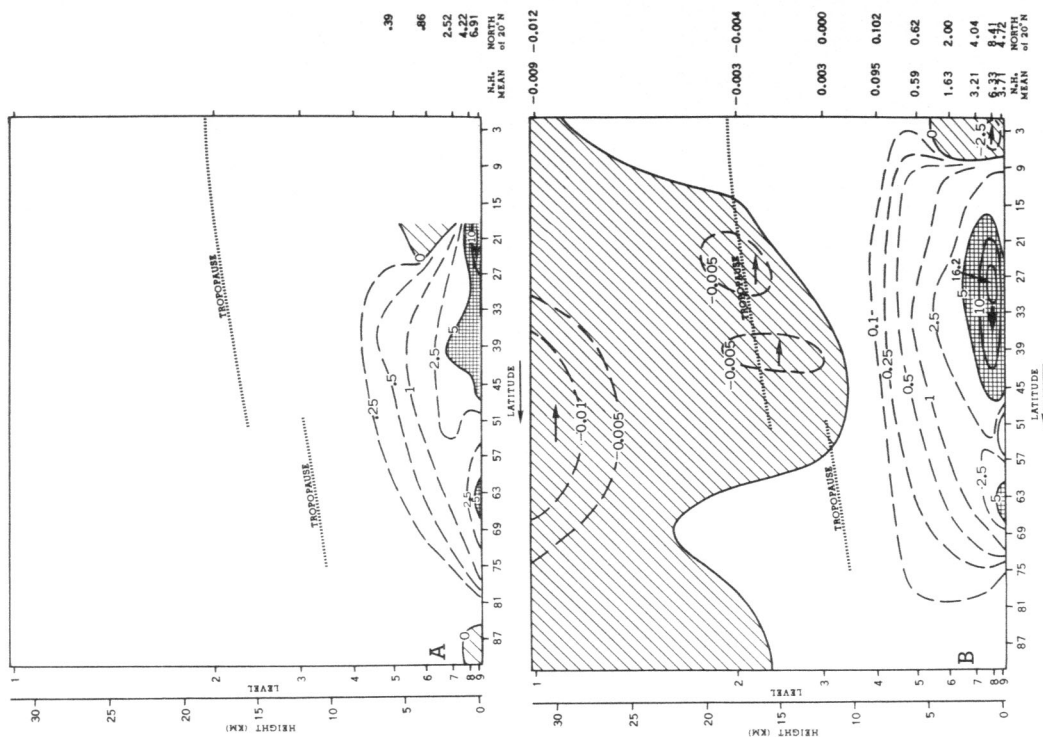
FIGURE 63.—Meridional flux of water vapor by eddies $\rho \cdot 2\pi \cdot a \cdot \cos \varphi \cdot \overline{v'r'}$ in units of 10^5 gm cm^{-1} sec^{-1} where r is the mixing ratio of water vapor. (A) the observed, valid between 850 and 500 mb, and (B) the prediction. The negative area is hatched. As for the flux due to the mean meridional circulation, it is known that the tropical values are larger; but only the flux by eddies is shown here.
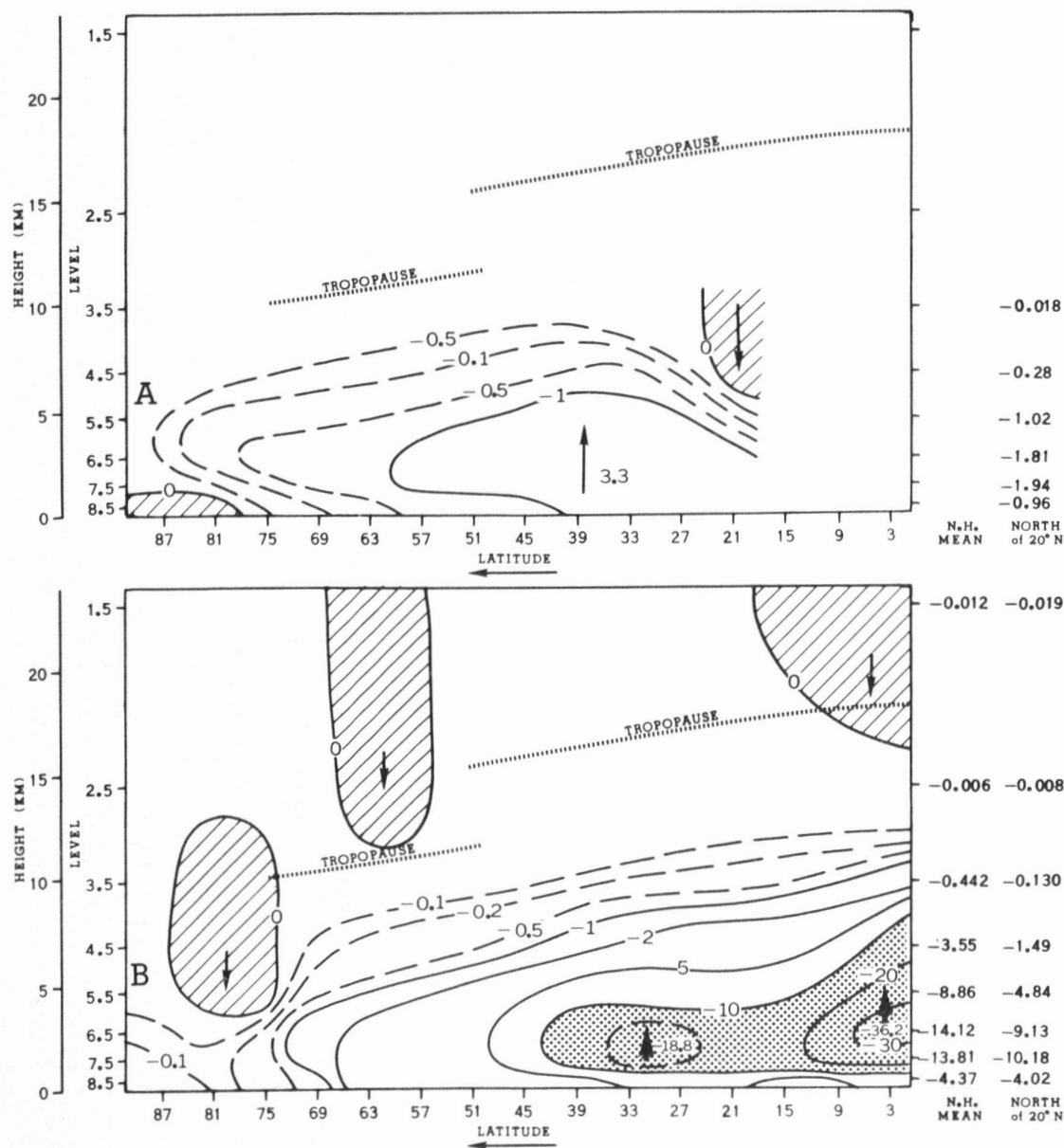

FIGURE 62.—Vertical flux of temperature by eddies $C_p \overline{\left(\frac{p*\tilde{\omega}}{g}\right)' T'}$ in units of 10^3 gm sec^{-3}. (A) from the ω-equation, and (B) the prediction. The arrows show the direction of flux.

FIGURE 64.—Vertical flux of water vapor by eddies $C_p \overline{\left(\frac{p_* \tilde{\omega}}{g}\right)' r'}$ in units of 10^{-7} gm cm^{-2} sec^{-1}. (A) from the ω-equation valid between 850 and 500 mb, and (B) the prediction.

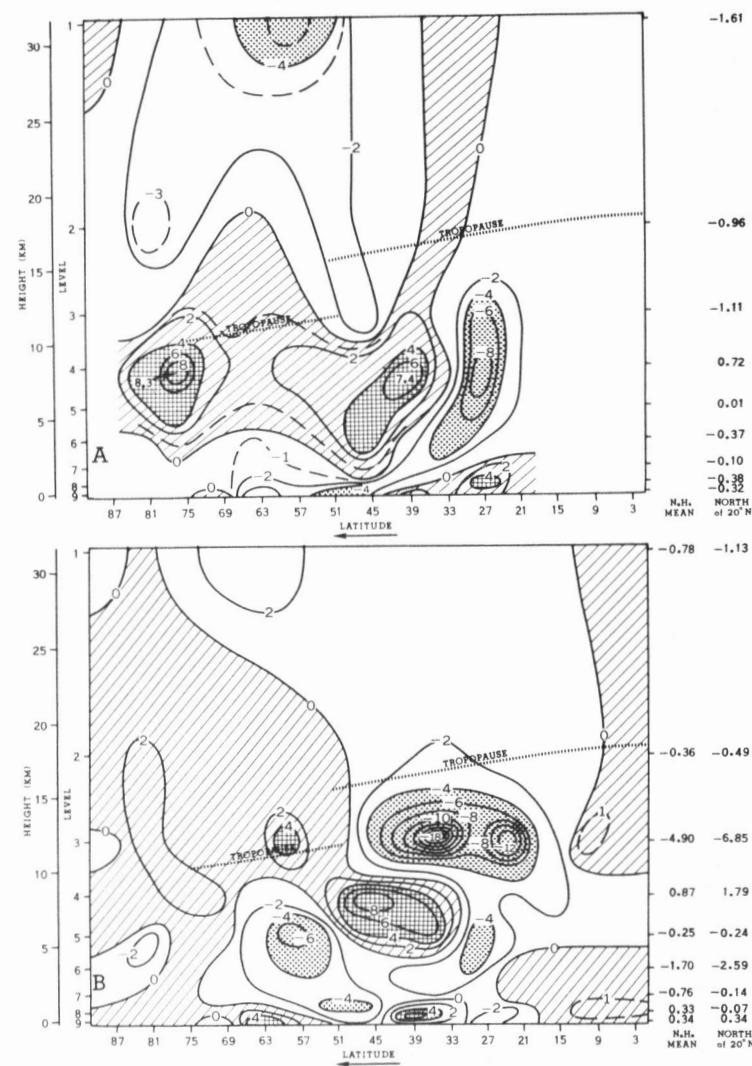FIGURE 66.—Budyko's (1963) 24-hr rate of evaporation for winter.

FIGURE 65.—Conversion from zonal kinetic to eddy kinetic energy $\langle k_z \cdot k_E \rangle$ in units of 10^{-4} ergs cm^{-3} sec^{-1}. The terms taken here are:

$$\langle k_z \cdot k_E \rangle = \frac{1}{a} \cdot \cos \varphi \cdot \overline{u'v'} \frac{\partial}{\partial \varphi}\left(\frac{\overline{u}}{\cos \varphi}\right) + \overline{(p_* \tilde{\omega})'u'} \cdot \frac{\partial \overline{u}}{\partial p} - \frac{\partial}{\partial p}[\overline{u}\,\overline{(p_* \tilde{\omega})'u'}],$$

where $\tilde{\omega} = \frac{d}{dt}(p/p_*)$. In the positive area, $K_z \rightarrow K_E$. (A) from the ω-equation, and (B) the prediction.
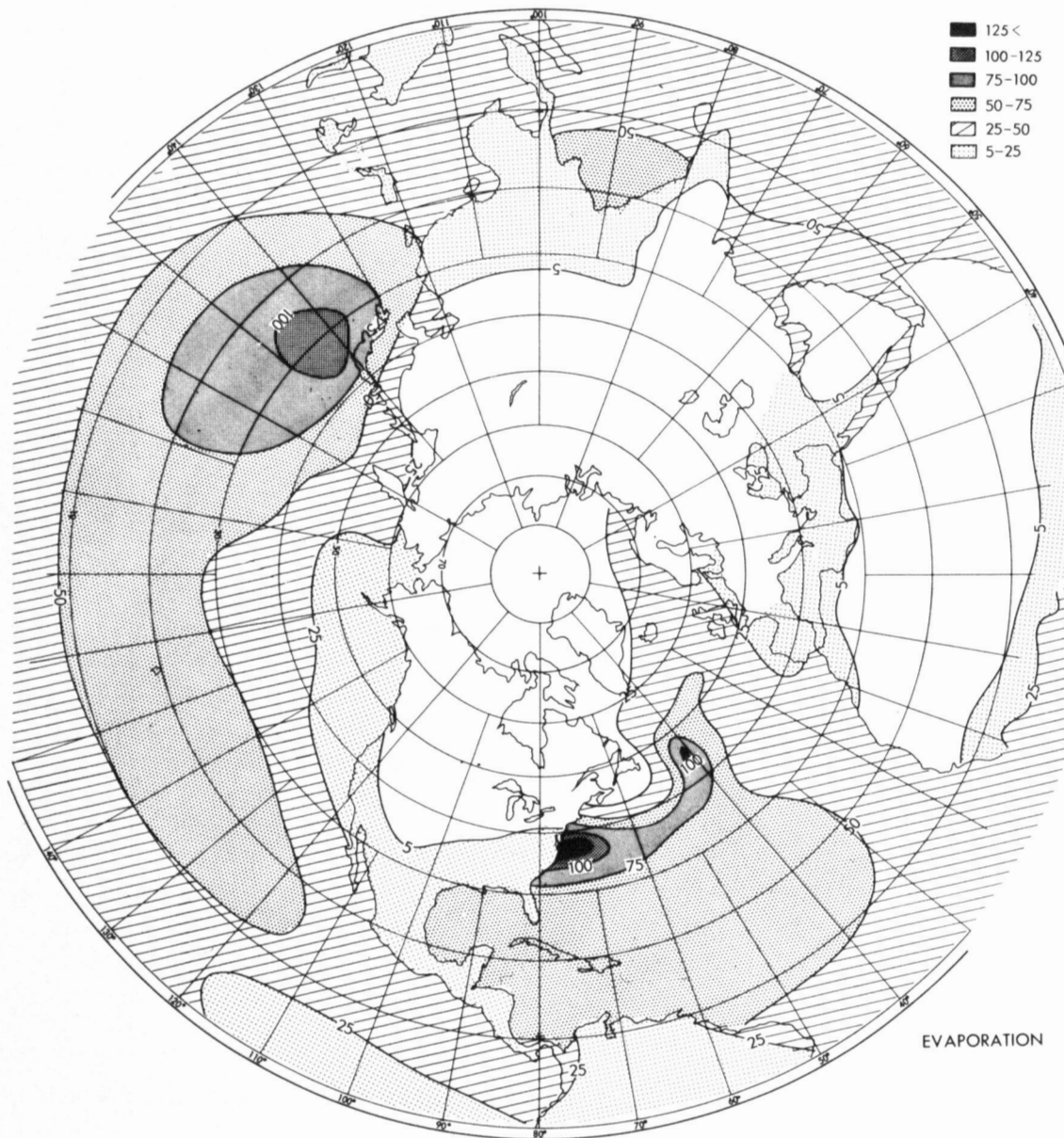
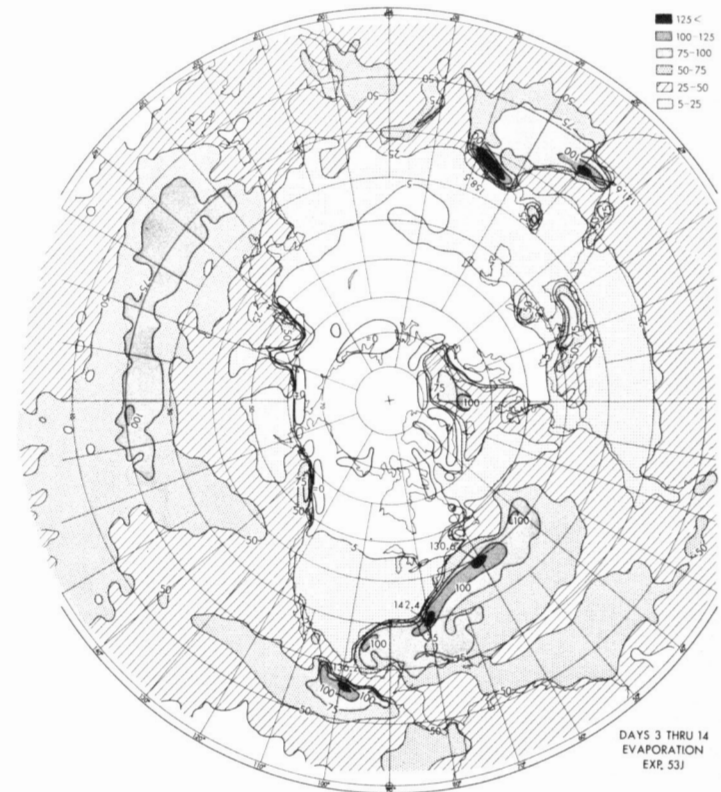FIGURE 66.—Budyko's (1963) 24-hr rate of evaporation for winter.

FIGURE 67.—Twenty-four-hour rate of evaporation in Experiment 3 of the 1964 case averaged for the period 3 to 14 days in units of 10^{-2} cm. In the polar region there are dry streaks which are the same phenomena as the so-called fictitious "land breeze" effect in figure 12. Comparing the computed evaporation for the 1964 (this figure) and 1966 (fig. 92) cases with Budyko's (1963) distribution (fig. 66), the following items are noted. 1) The computed distributions are more similar to each other than to Budyko's distribution. 2) In his map, there are three major evaporation regions in the Northern Hemisphere, i.e., the *Gulf Stream*, the *Kuroshio Current*, and the *North Atlantic*. In the computed results these have been to some extent obtained, but the computed evaporation east of the Asian Continent, i.e., near Japan, is smaller. 3) The computed evaporations near Mexico in the Pacific Ocean and over the Arabian Sea are very large. 4) The computed evaporation over land in the middle and low latitudes are large, especially over the Sahara Desert for instance.

APPENDIX III.—FIGURES FOR AN ADDITIONAL CASE, I.E., THE 1966 CASE

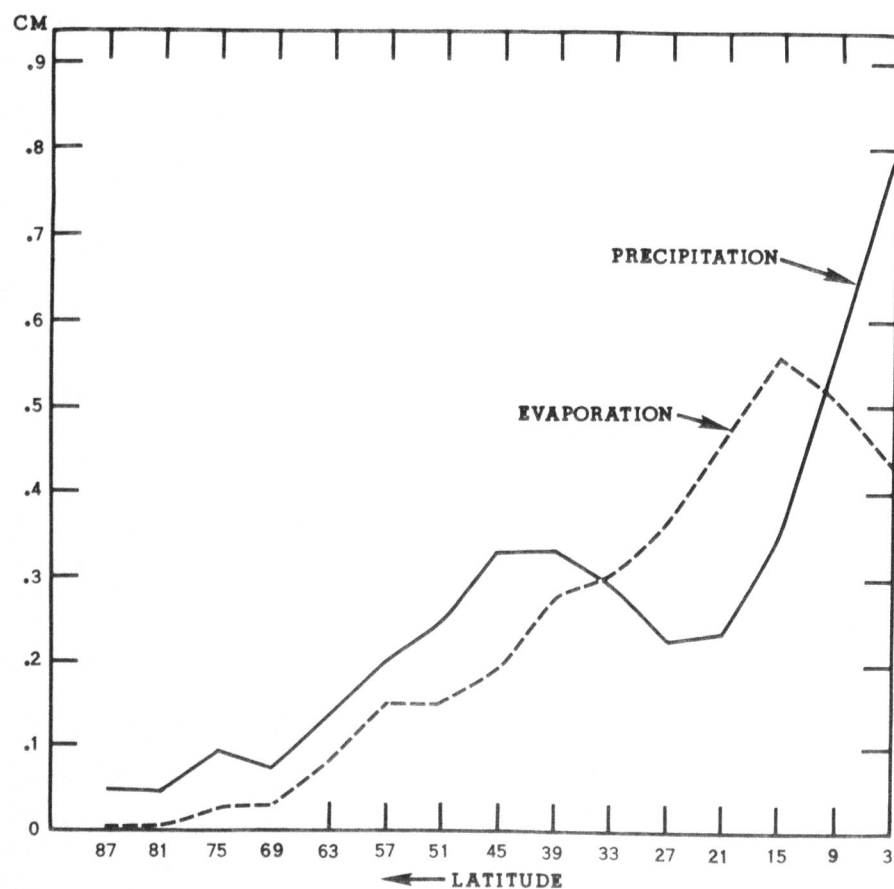## ZONALLY AVERAGED PRECIPITATION AND EVAPORATION

FIGURE 68.—Latitudinal distribution of the 24-hr rates of precipitation and evaporation. This is zonally and time averaged for the period 3 to 14 days. See figure 45.
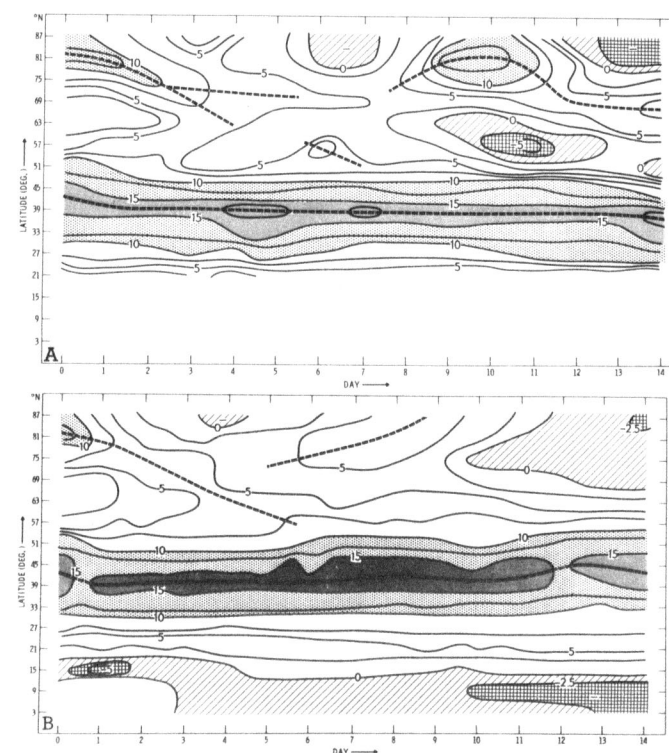
TIME-LATITUDE CHART OF ZONAL WIND

FIGURE 69.—Time-latitude charts of the zonally averaged zonal wind at level 6 (664 mb). (A) the observed, and (B) the result for the 1966 case. In both the 1964 case (fig. 33) and the 1966 case, there is a common defect; the latitudinal splitting of the westerlies in the observed pattern is not well formed in the later stages of the prediction. This is shown in the height-latitude diagram of the zonally averaged zonal winds (see figs. 36 and 71).

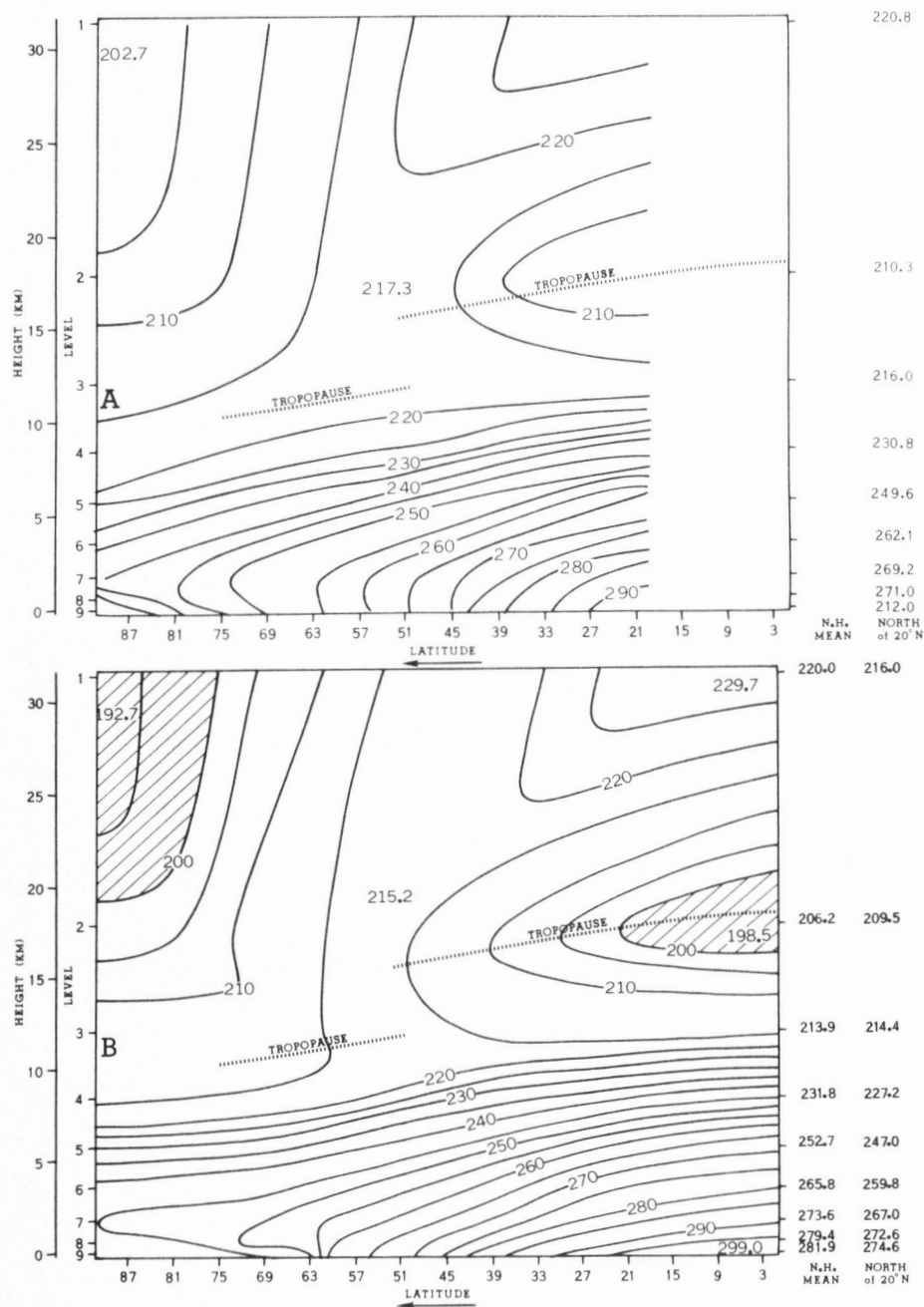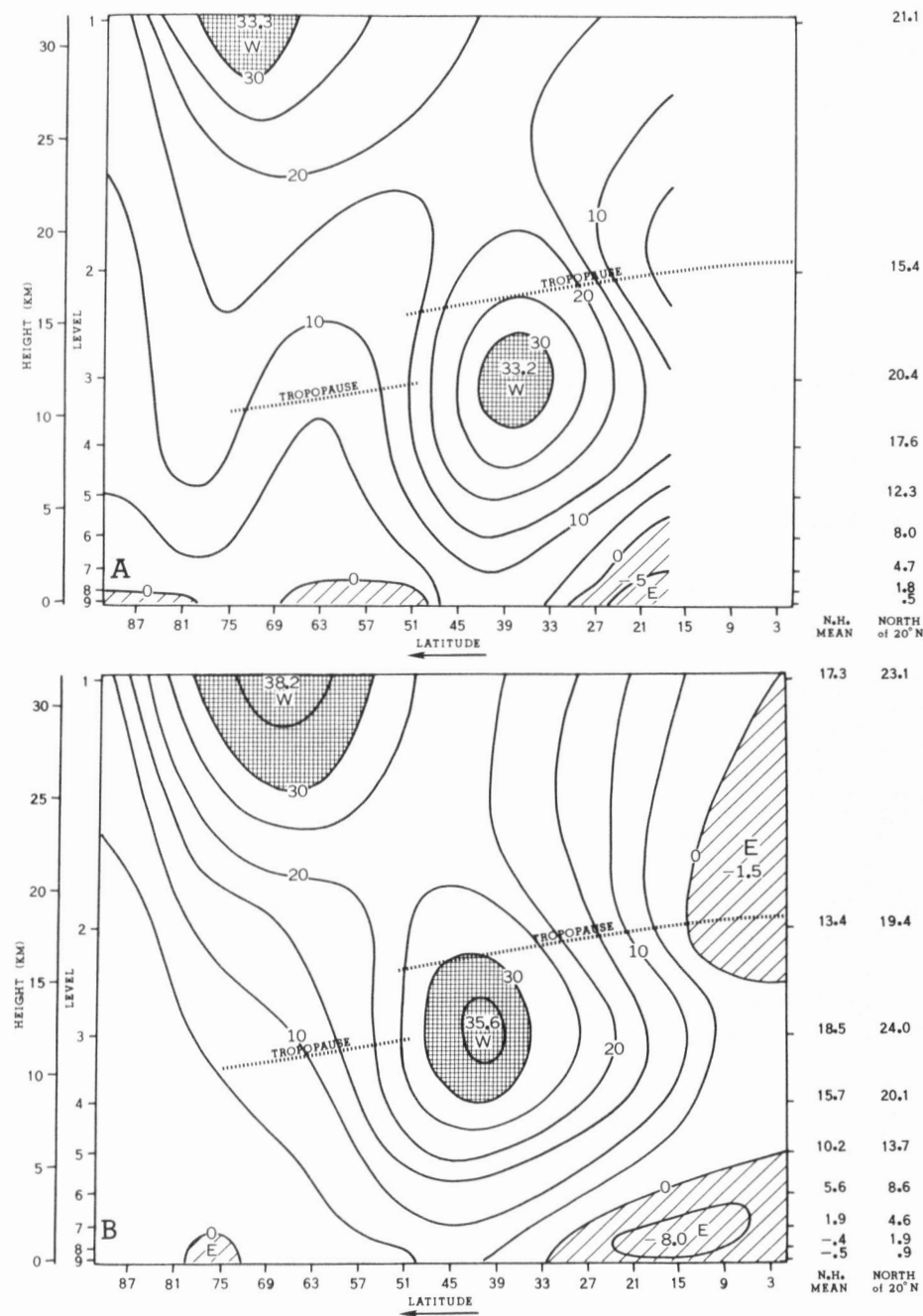FIGURE 70.—Temperature $\overline{T}$ in units of °K (A) the observed, and (B) the prediction. See figure 54.

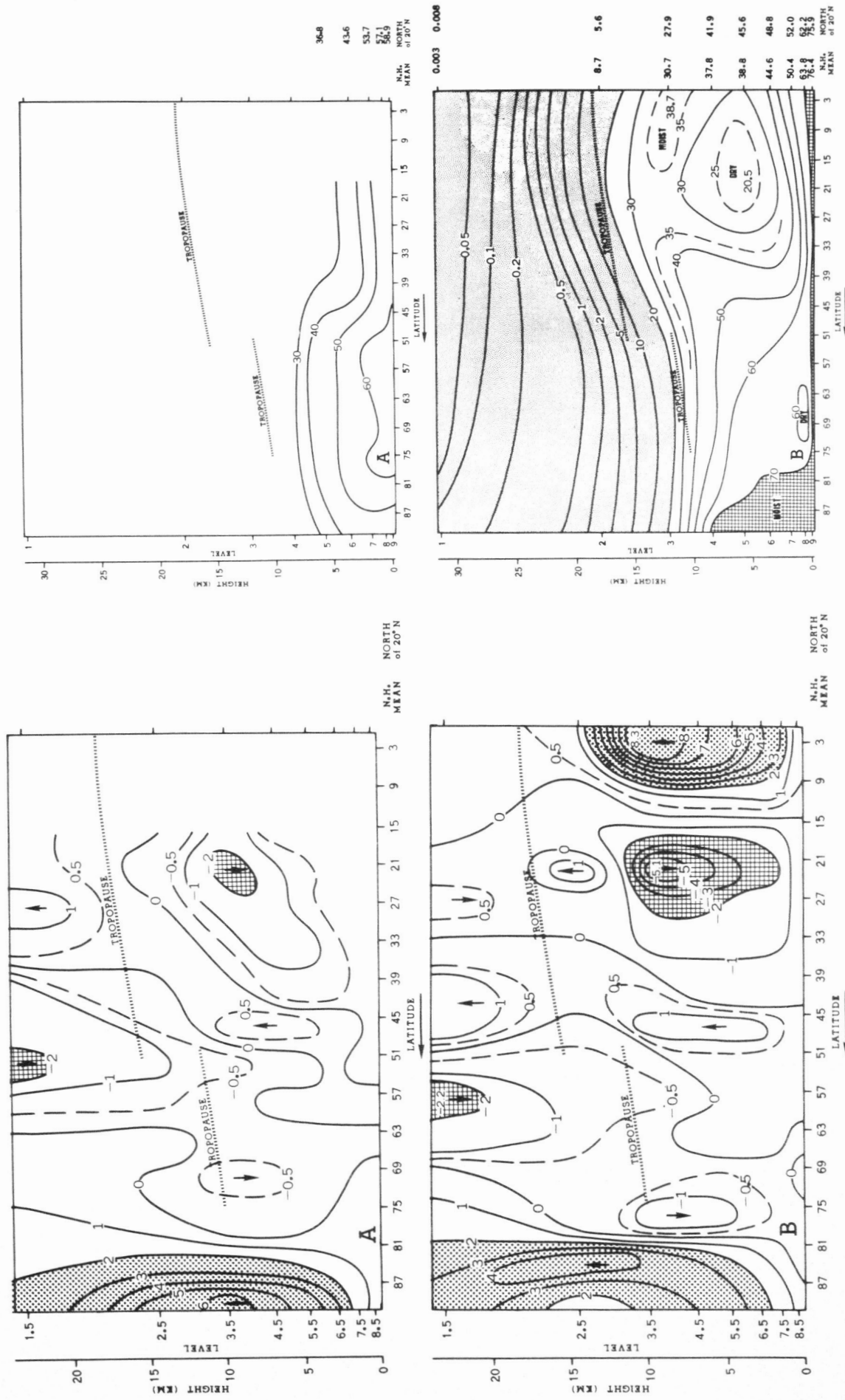FIGURE 71.—Zonal wind $\overline{U}$ in units of meters per second. (A) the observed, and (B) the prediction. See figure 36.
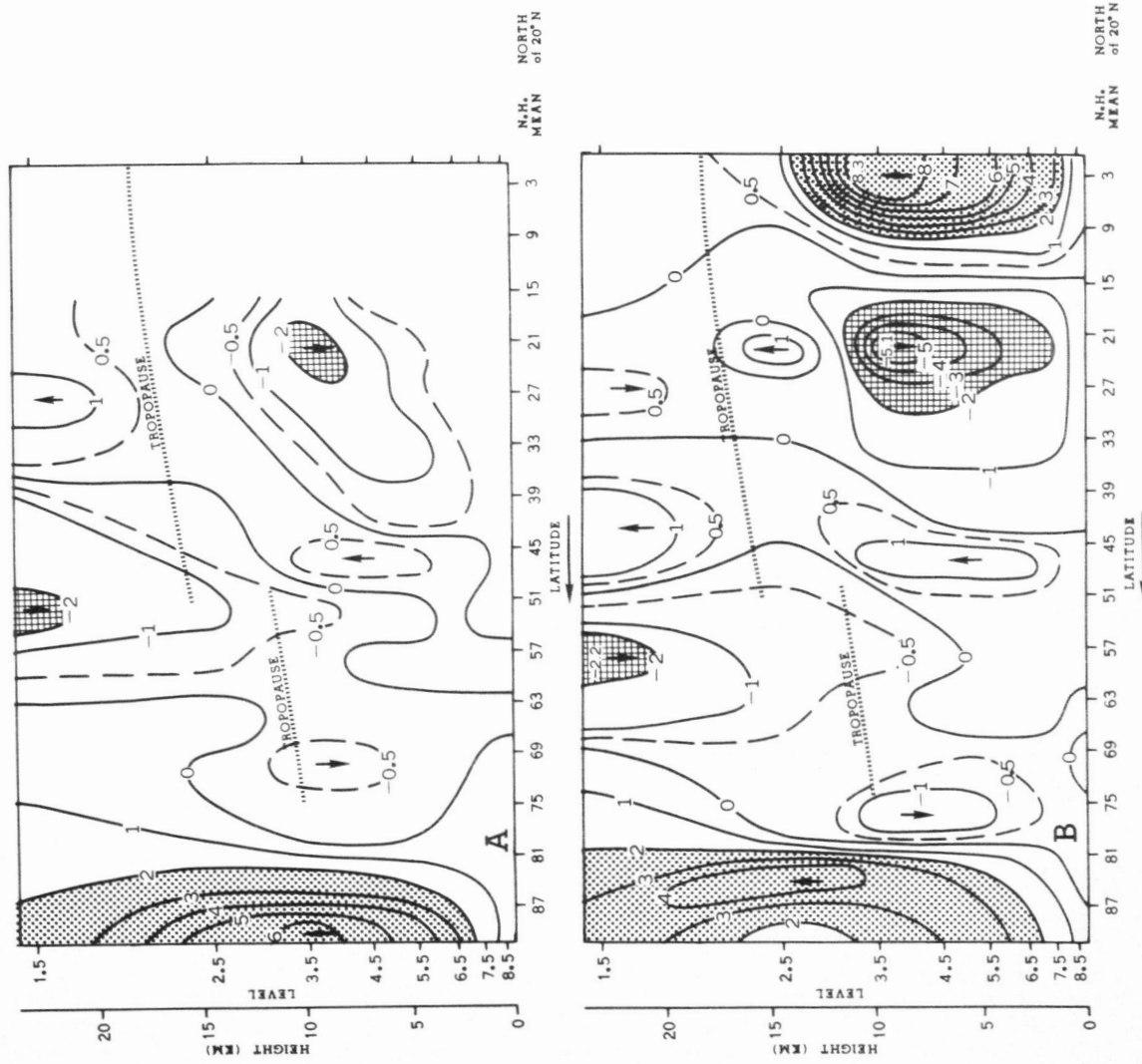
FIGURE 73.—Humidity $\bar{h}$ in units of percent. (A) the observed, and (B) the prediction. See figure 3 of Manabe et al. (1965) for further explanation. See also figure 55.
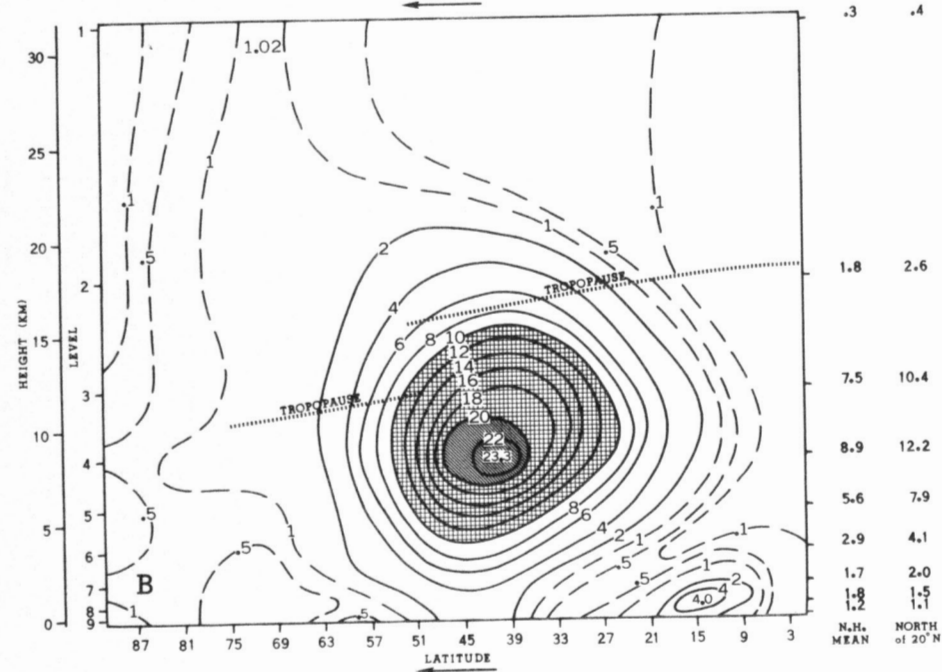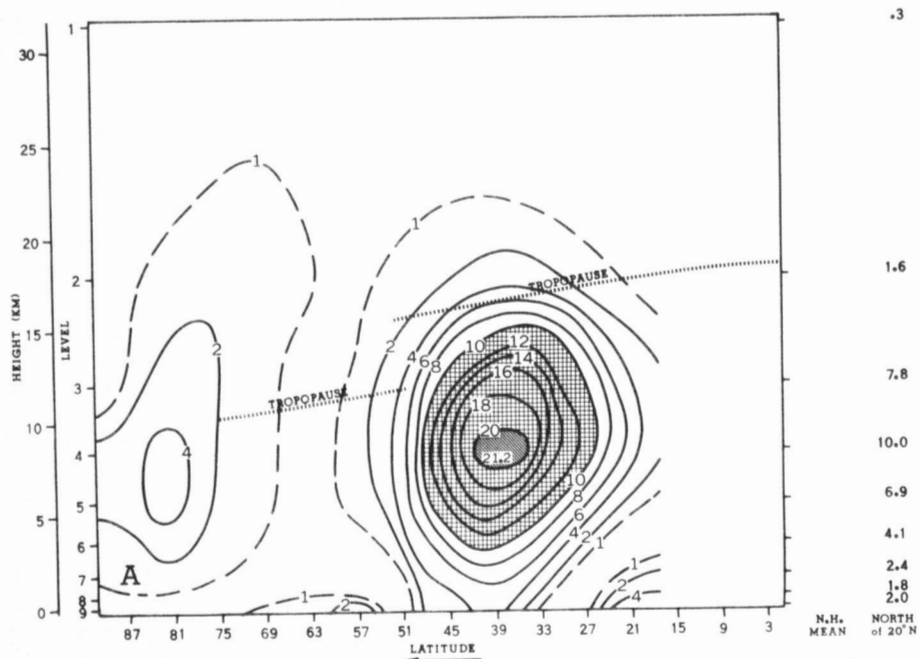

FIGURE 72.—Vertical velocity $\overline{W}$ in units of centimeters per second. (A) from the ω-equation, and (B) the prediction. See figure 38.

FIGURE 74.—Zonal kinetic energy ρK_z in units of 10^2 ergs/cm³. (A) the observed, and (B) the prediction. See figure 56.
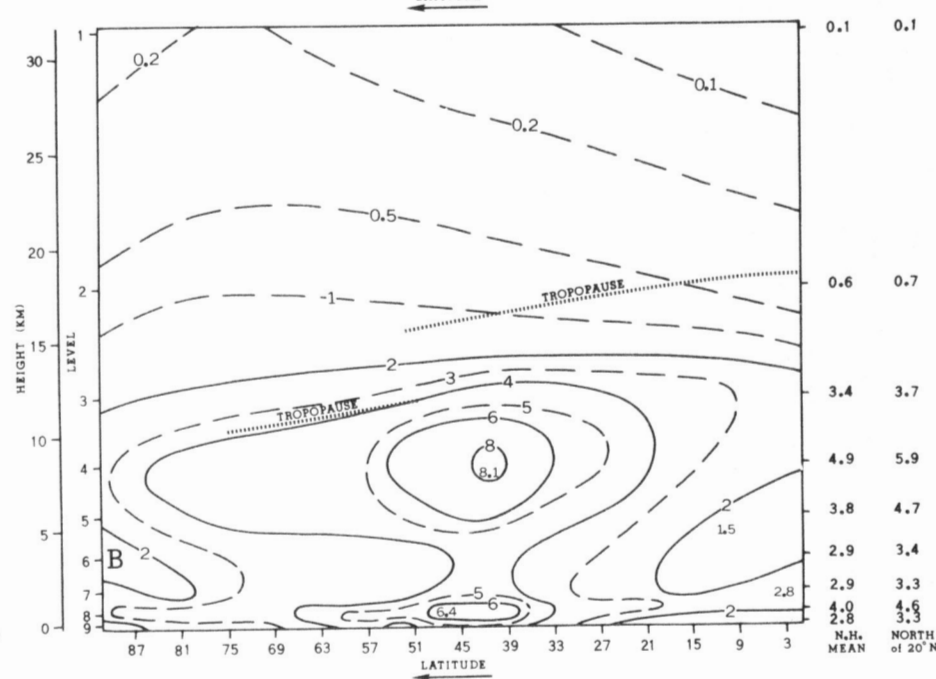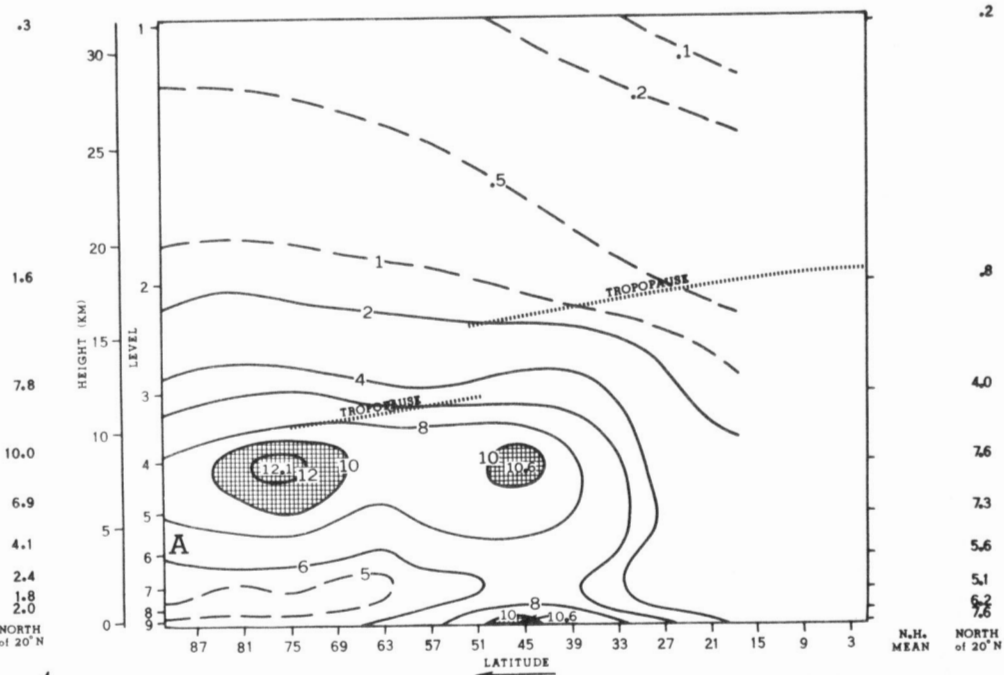

FIGURE 75.—Eddy kinetic energy ρK_E in units of 10^2 ergs/cm³. (A) the observed, and (B) the prediction. The areas where the intensity is larger than 10^3 ergs/cm³ are cross-hatched. See figure 37.
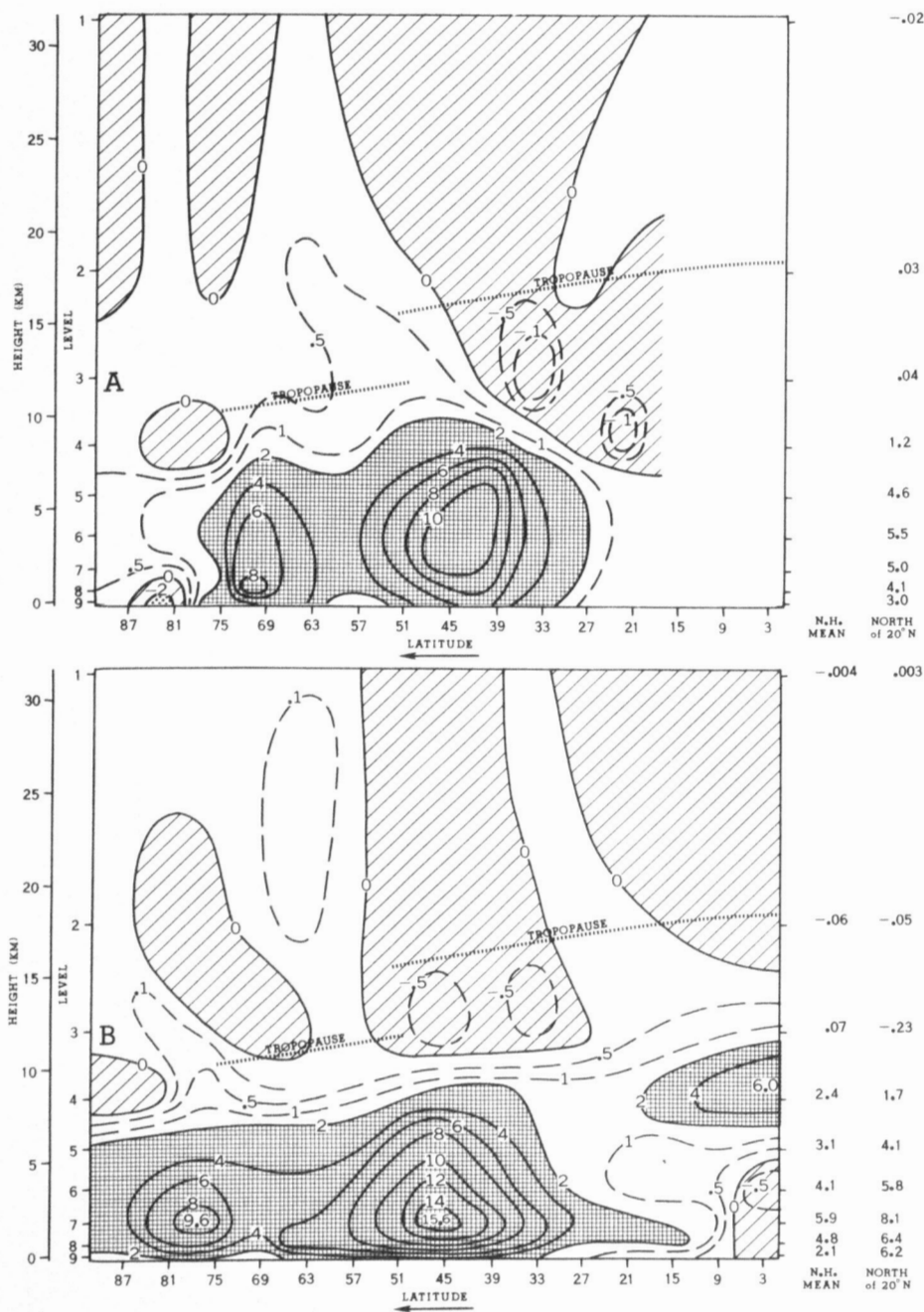
FIGURE 76.—Conversion of eddy available potential energy to eddy kinetic energy $-\overline{\rho \omega' \alpha'}$ in units of 10^{-3} ergs cm^{-3}sec^{-1}, where $\alpha = 1/\rho$. (A) from the ω-equation, and (B) the prediction. The areas where the intensity is larger than 2×10^{-3} ergs cm^{-3}sec^{-1} are crosshatched, and the negative areas are hatched. See figure 40.

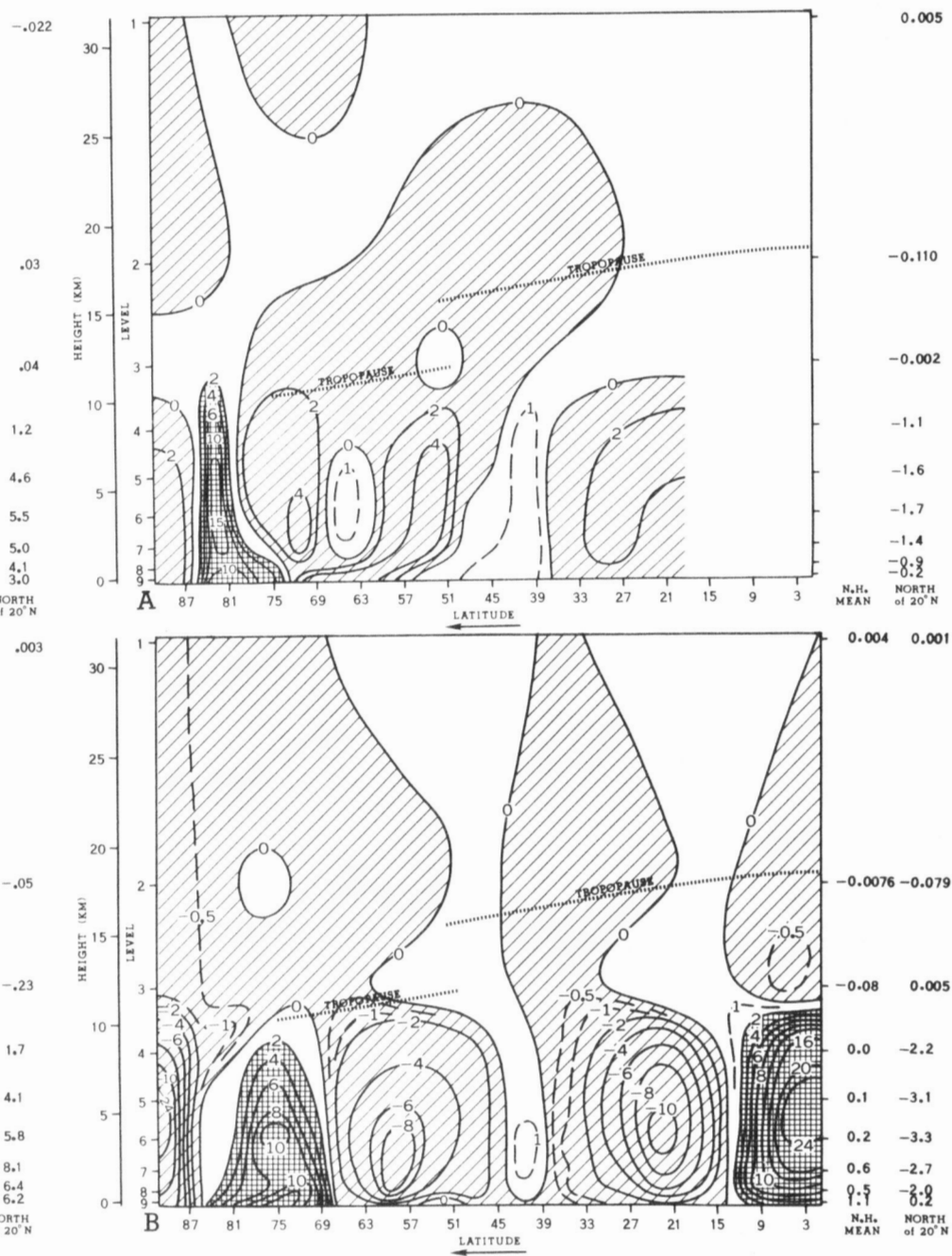FIGURE 77.—Conversion of zonal available potential energy to zonal kinetic energy $-\rho \overline{\omega} \cdot \overline{\alpha}$ in units of 10^{-3} ergs cm^{-3} sec^{-1}. (A) from the ω-equation, and (B) the prediction. See figure 58.
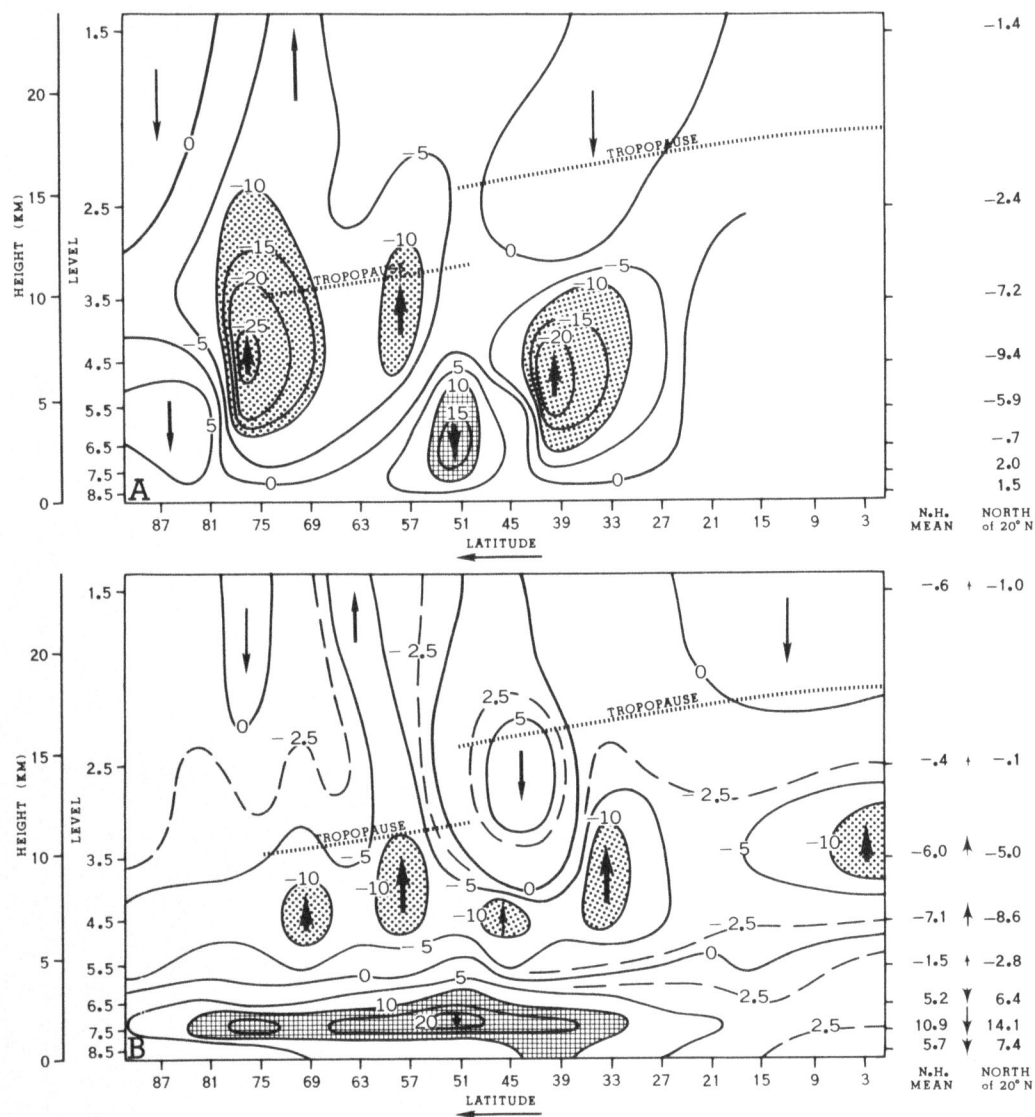
FIGURE 78.—Vertical flux of geopotential height by eddies $\overline{\omega'\phi'}$ in units of 10^2 gm sec^{-3}. (A) from the ω-equation, and (B) the prediction. The arrows show the direction of propagation of eddy kinetic energy. See figure 57.
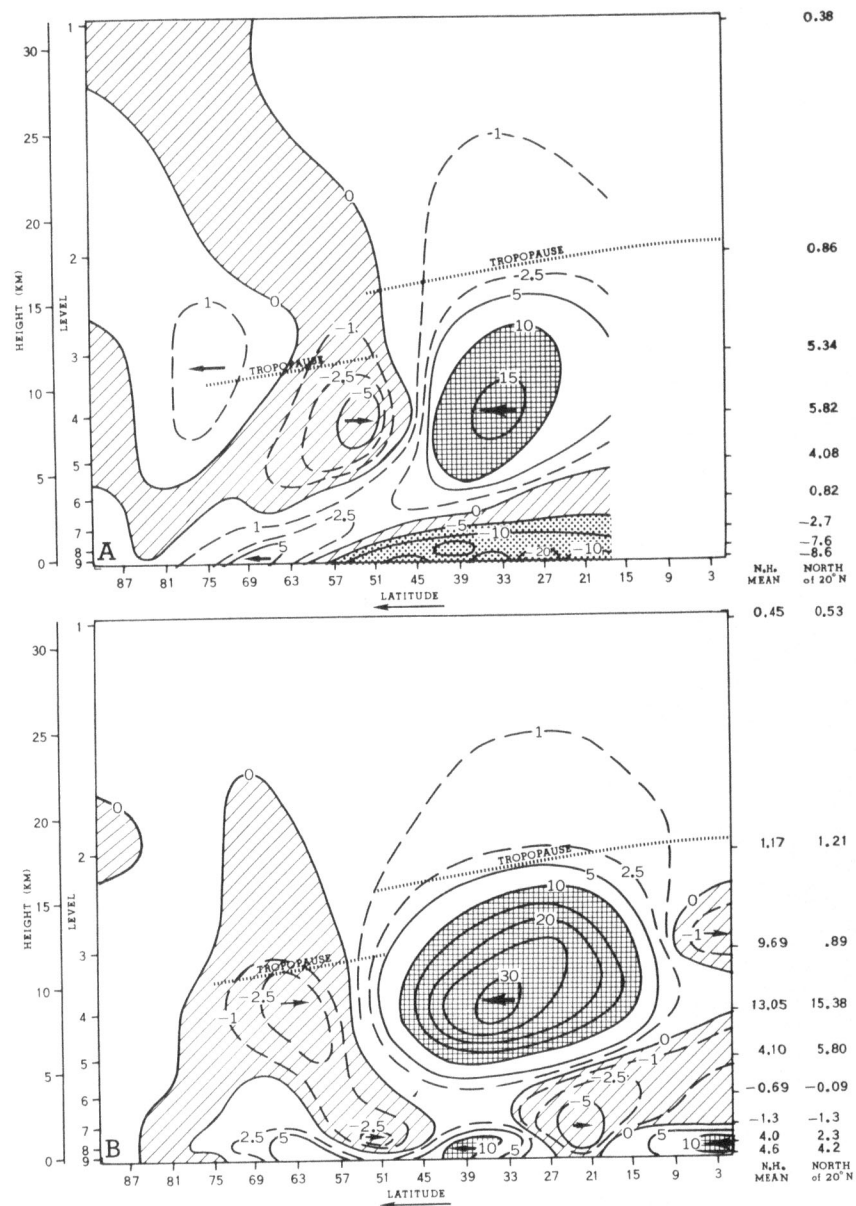
FIGURE 79.—Meridional flux of angular momentum by eddies $\rho \cdot 2\pi a \cdot \cos\varphi$ $\overline{v'M_A'}$ in units of 10^{19} gm cm sec^{-2}. (A) the observed, and (B) the prediction. See figure 59.

FIGURE 81.—Meridional flux of temperature by eddies $\rho c_p \cdot 2\pi a \cdot \cos \varphi \cdot \overline{v'T'}$, in units of 10^{16} ergs cm^{-1} sec^{-1}. (A) the observed, and (B) the prediction. See figure 61.

FIGURE 80.—Vertical flux of angular momentum by eddies $\overline{\left(\dfrac{p_* \tilde{\omega}}{g}\right)' M_A'}$ in units of 10 gm sec^{-2}, where p_* is the surface pressure and $\tilde{\omega} = d(p/p_*)/dt$. (A) from the ω-equation, and (B) the prediction. The arrows show the direction of flux. See figure 60.
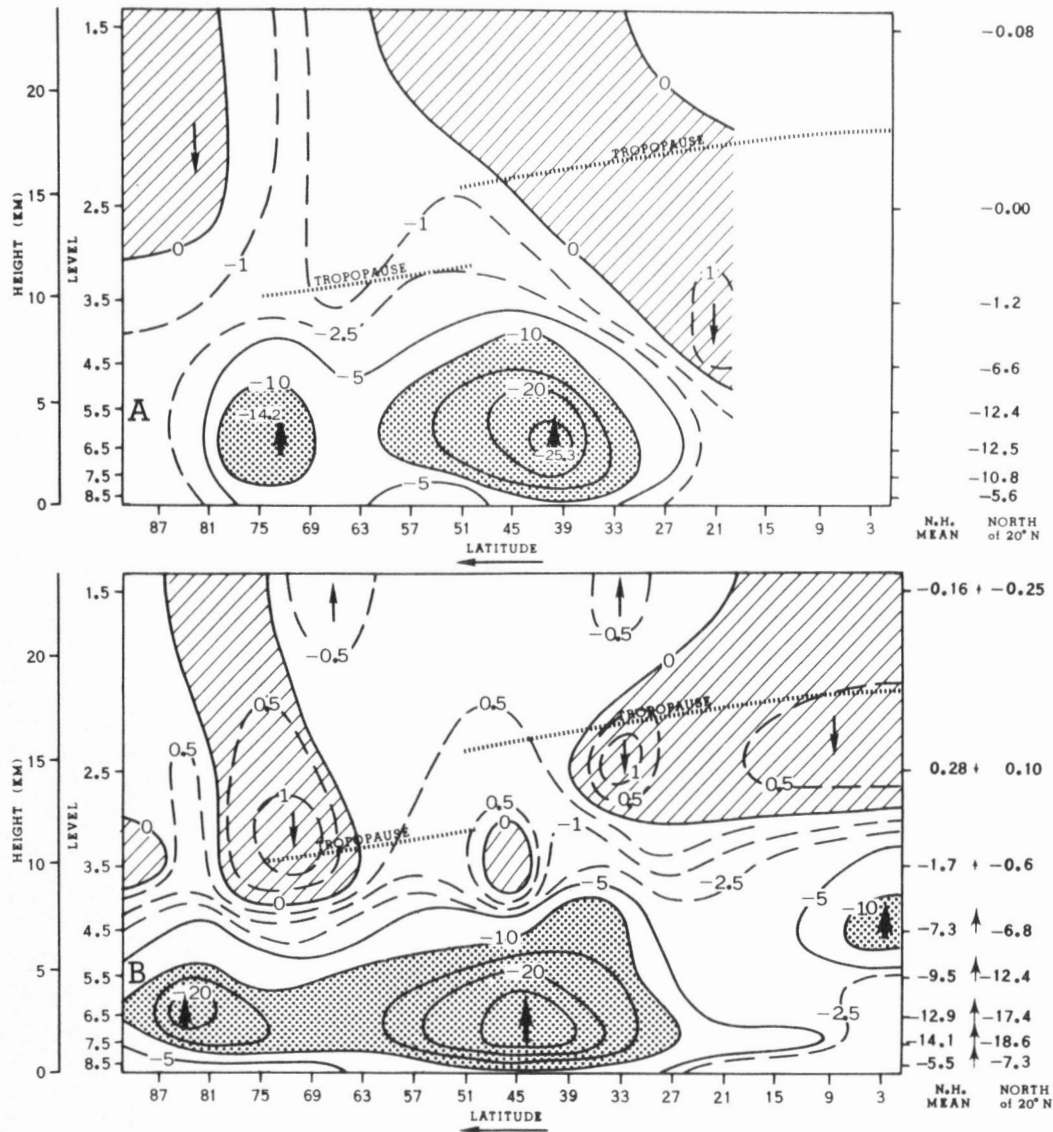
FIGURE 82.—Vertical flux of temperature by eddies $c_p \overline{\left(\dfrac{p_* \tilde{\omega}}{g}\right)' T'}$ in units of 10^3 gm sec^{-3}. (A) from the ω-equation, and (B) the prediction. The arrows show the direction of flux. See figure 62.
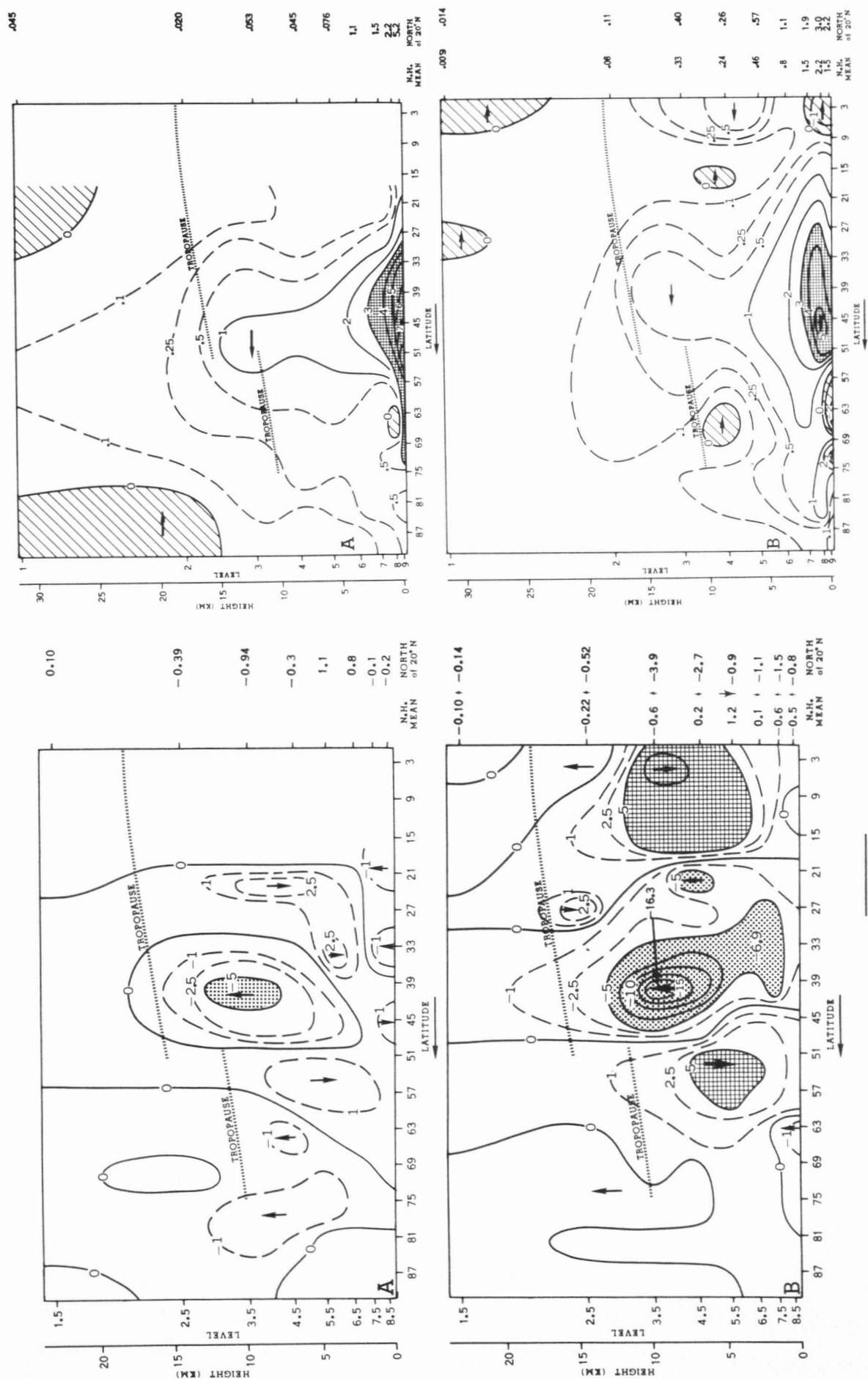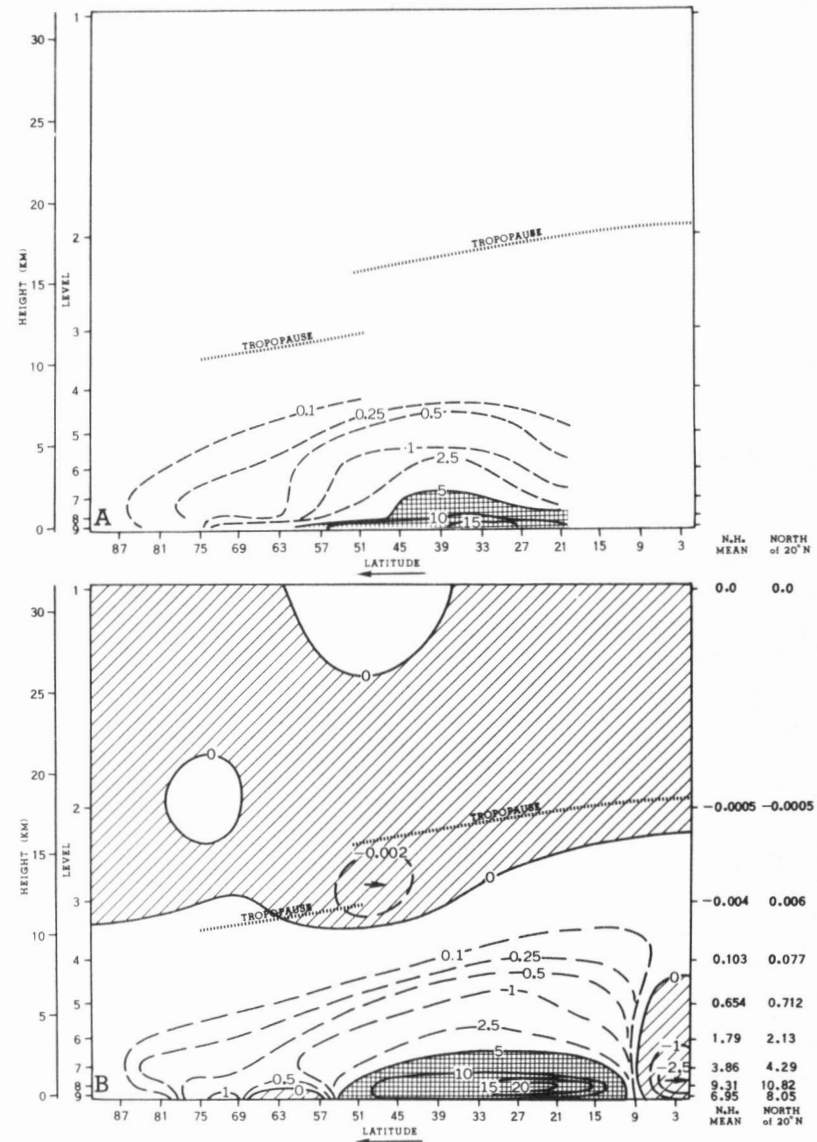
FIGURE 83.—Meridional flux of water vapor by eddies $\rho \cdot 2\pi a \cos \varphi \cdot \overline{v' r'}$ in units of 10^5 gm cm^{-1} sec^{-1}. (A) the observed, valid between 850 and 500 mb, and (B) the prediction. See figure 63.
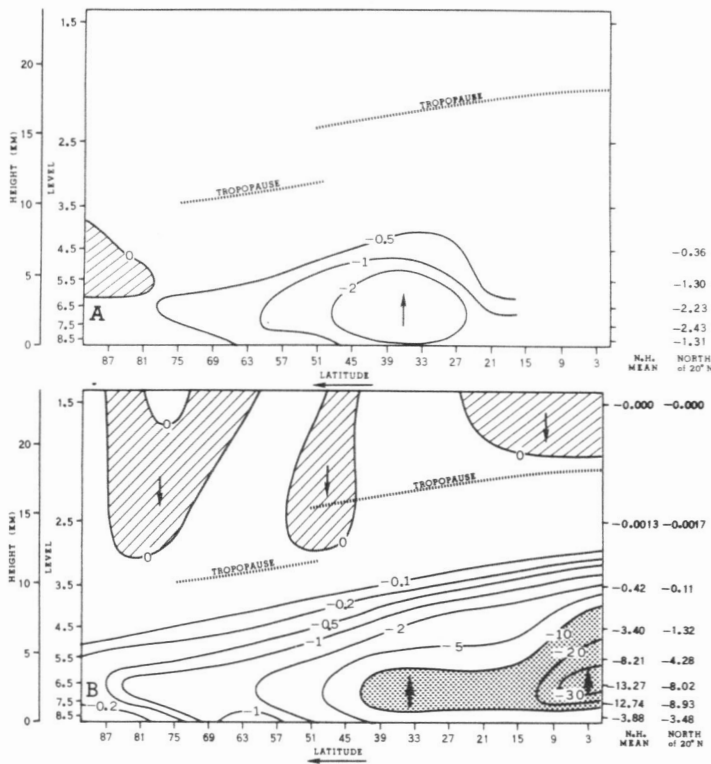
FIGURE 84.—Vertical flux of water vapor by eddies $\overline{\left(\dfrac{p_*\tilde{\omega}}{g}\right)' r'}$ in units of 10^{-7} gm cm^{-2} sec^{-1}. (A) from the ω-equation, valid between 850 and 500 mb, and (B) the prediction. See figure 64.
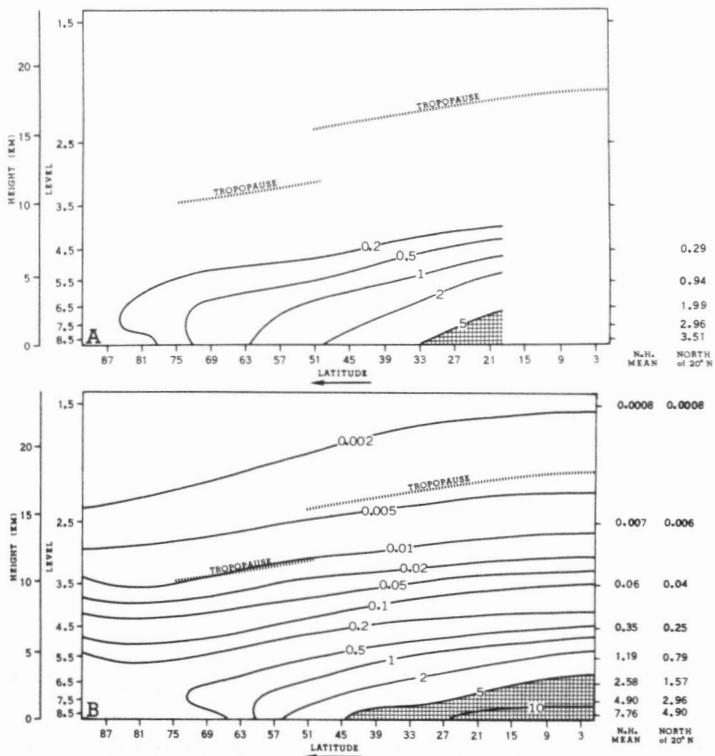
FIGURE 85.—Mixing ratio of water vapor $\bar{r}$ in units of gr/kg. (A) the observed, and (B) the prediction.
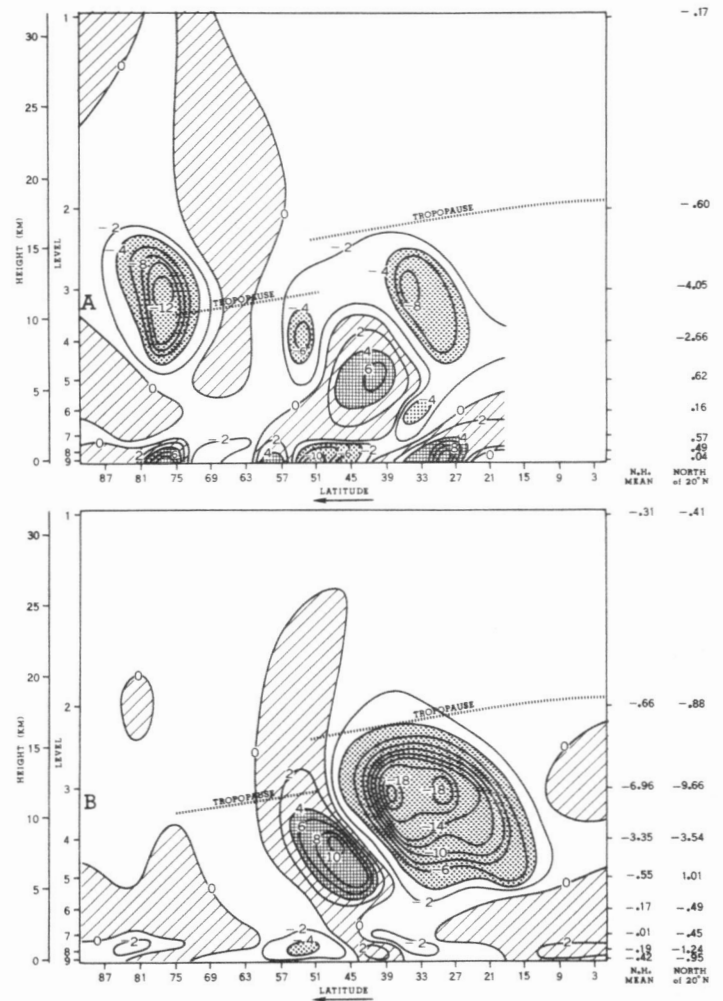
FIGURE 86.—Conversion from zonal kinetic to eddy kinetic energy $\langle k_z \cdot k_E \rangle$ in units of 10^{-4} ergs cm^{-3} sec^{-1}. (A) observed data and from the ω-equation, and (B) the prediction. See figure 65.

TROUGH AND RIDGE DIAGRAMS

FIGURE 87.—Trough-and-ridge diagrams for 35°–45° lat. at 500 mb in the 1966 case. (A) the observed, and (B) the prediction. See figure 22.

FIGURE 88.—Trough-and-ridge diagrams for 35°–45° lat. at 1000 mb in the 1966 case. (A) the observed, and (B) the prediction. See figure 23.
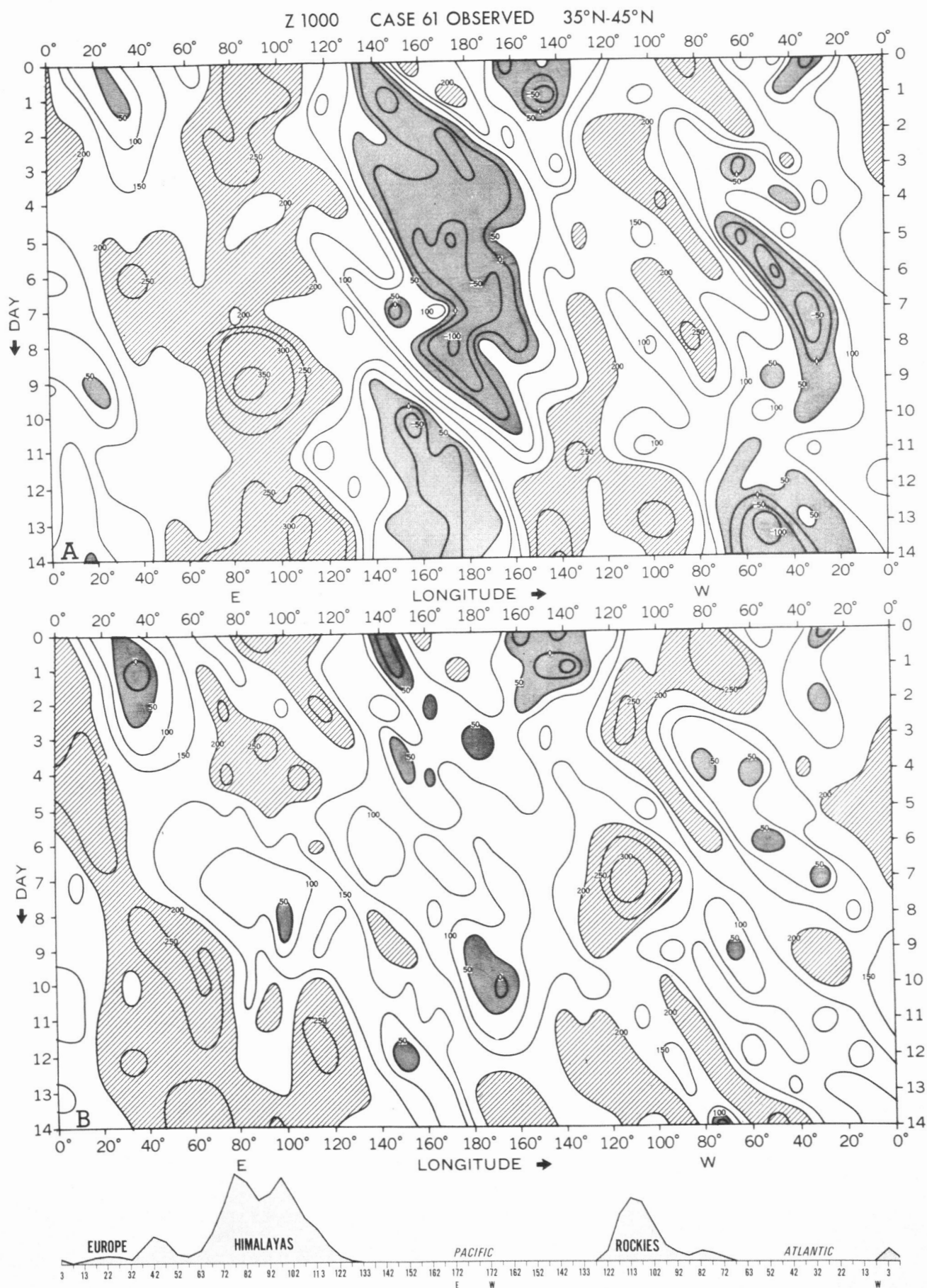
VERIFICATION STATISTICS
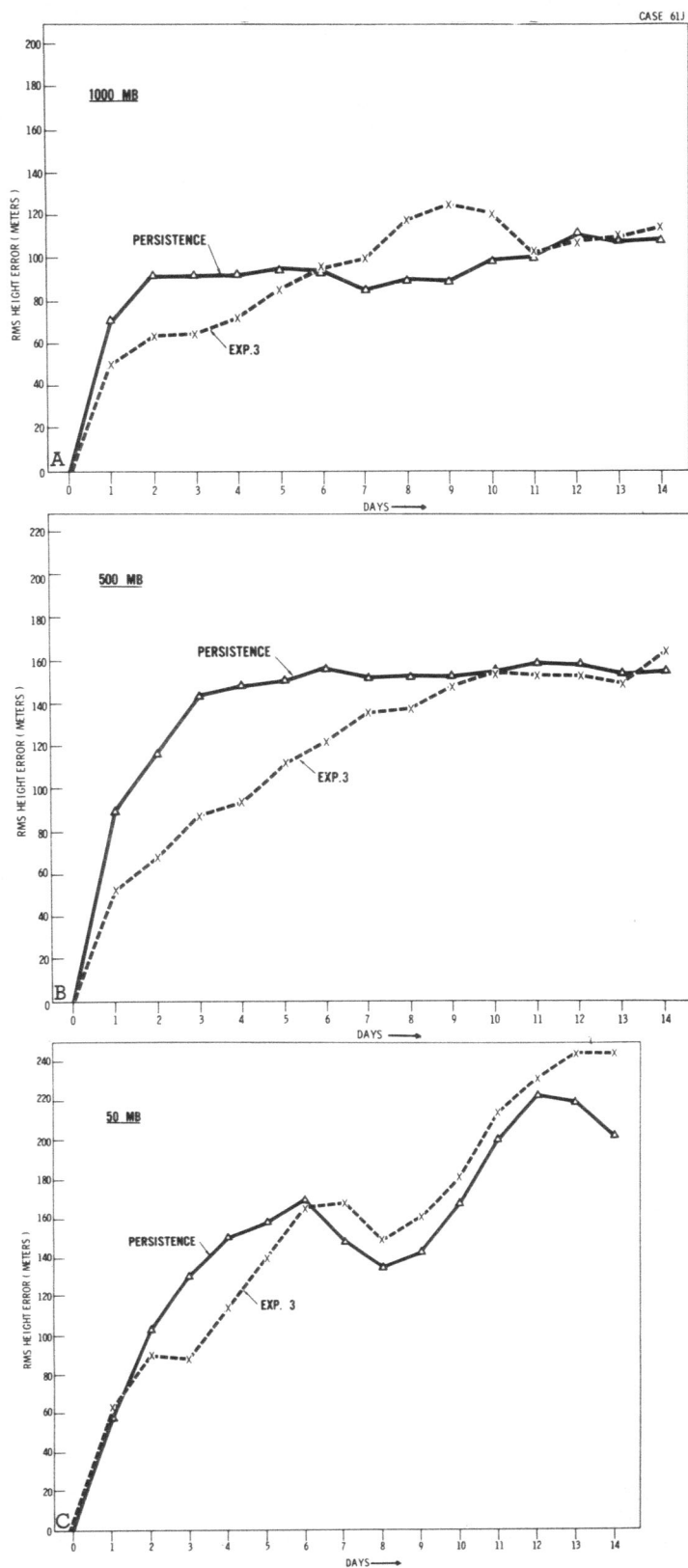
FIGURE 89.—Standard deviation of the difference between the observed and predicted geopotential heights for the 1966 case. (A) 1000 mb, (B) 500 mb, and (C) 50 mb. See section 7 and figure 24 for further details.
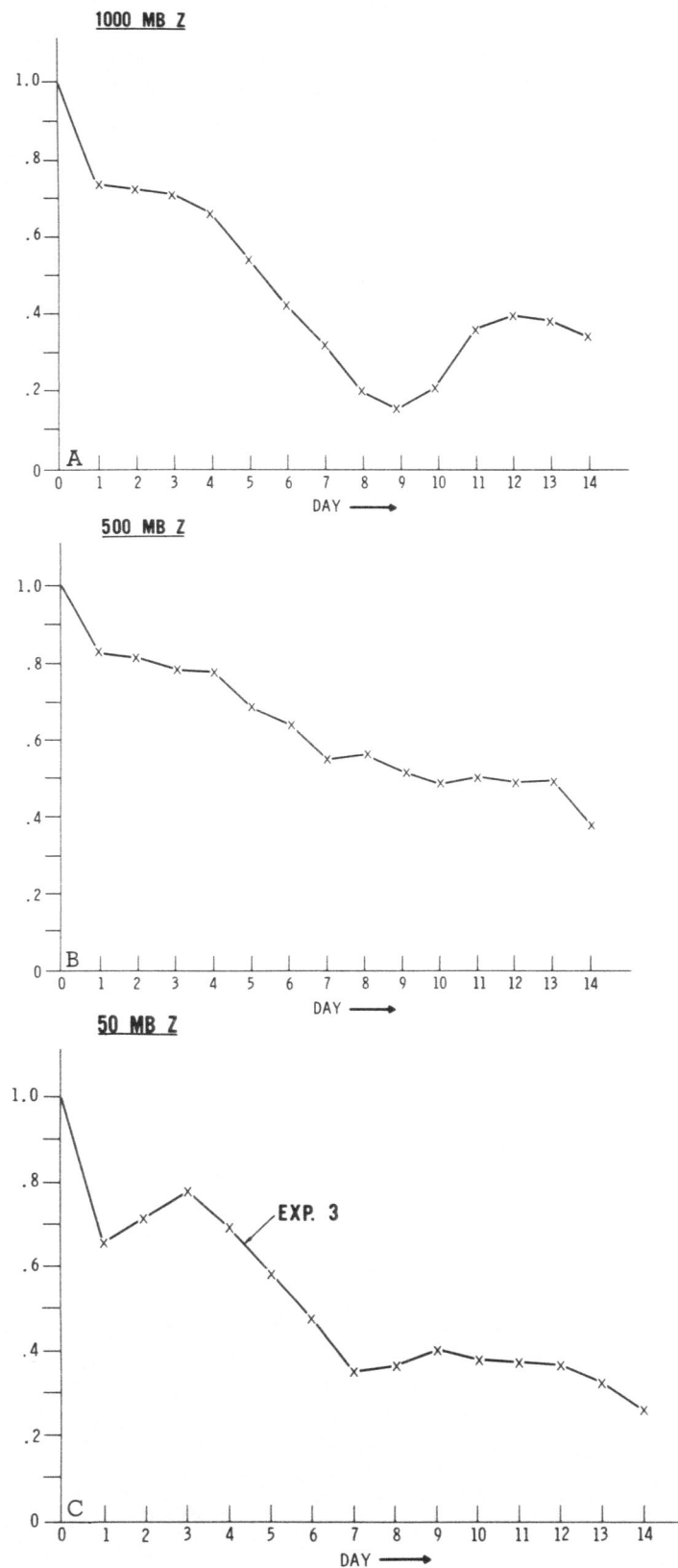
FIGURE 90.—Correlation coefficient for the observed and predicted patterns of time change of the geopotential heights for the 1966 case. (A) 1000 mb, (B) 500 mb, and (C) 50 mb. See section 7 and figure 25 for further details.

HEMISPHERIC MAPS OF PRECIPITATION AND EVAPORATION

REFERENCES

FIGURE 91.—Twenty-four-hour rate of precipitation averaged for the period 3 to 14 days. The details are the same as given for figure 42.

FIGURE 92.—Twenty-four-hour rate of evaporation averaged for the period 3 to 14 days. The details are the same as given for figure 67. Compare this with figure 66.

Budyko, M. I., *The Heat Balance of the Earth's Surface*, (Teplovoĭ Balans Zemnoĭ Poverkhnosti, 1956), N. A. Stepanova, Translator, U.S. Weather Bureau, Washington, D.C., **1958**, 259 pp.
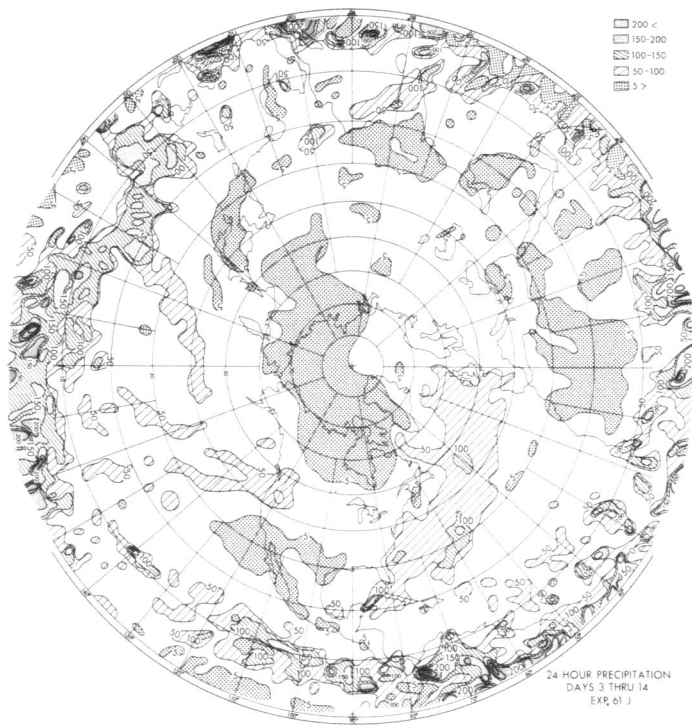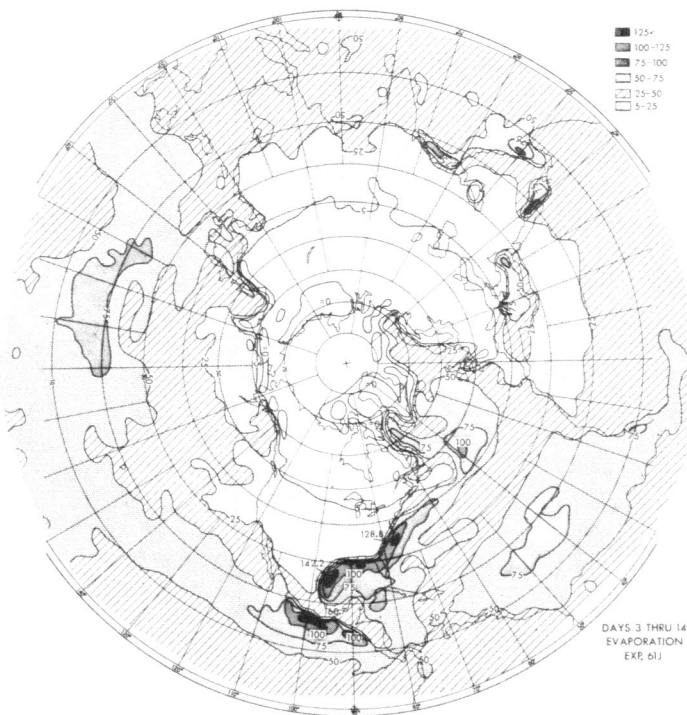
Budyko, M. I., Editor, "Atlas Teplovogo Balansa Zemnogo Shara," (Atlas of the Heat Balance of the Globe), *Mezhduredomstvennyĭ Geofizicheskiĭ Komitet pri Prezidiume*, U.S.S.R. Academy of Sciences, Moscow, **1963**, 69 pp.

Bushby, F. H., and Hinds, M. K., "Further Computations of 24-Hr. Pressure Changes Based on a Two-Parameter Model," *Quarterly Journal of the Royal Meteorological Society*, Vol. 81, No. 349, July **1955**, pp. 396–402.

Charney, J. G., "Dynamic Forecasting by Numerical Process," *Compendium of Meteorology*, American Meteorological Society, **1951**, pp. 470–482.

Charney, J. G., and Eliassen, A., "A Numerical Method for Predicting the Perturbations of the Middle-Latitude Westerlies," *Tellus*, Vol. 1, No. 2, May **1949**, pp. 38–54.

Clapp, P. F., "Global Cloud Cover for Seasons Using TIROS Nephanalyses," *Monthly Weather Review*, Vol. 92, No. 11, Nov. **1964**, pp. 495–507.

Cressman, G. P., "Barotropic Divergence and Very Long Atmospheric Waves," *Monthly Weather Review*, Vol. 86, No. 8, Aug. **1958**, pp. 293–297.

Gilman, D. L., "The Primitive Equations in Extended Forecasting," (Abstract), *Transactions, American Geophysical Union*, Vol. 49, No. 1, Mar. **1968**, p. 183.

Graham, R. D., "An Empirical Study of Planetary Waves by Means of Harmonic Analysis," *Journal of Meteorology*, Vol. 12, No. 4, Aug. **1955**, pp. 298–307.

Hovmöller, E., "The Trough-and-Ridge Diagram," *Tellus*, Vol. 1, No. 2, May **1949**, pp. 62–66.

Japan Meteorological Agency, Electronic Computation Center, "72-Hour Baroclinic Forecast by the Diabatic Quasi-Geostrophic Model," *Journal of the Meteorological Society of Japan*, Vol. 43, No. 5, Oct. **1965**, pp. 246–261.

Kung, E. C., Bryson, R. A., and Lenschow, D. H. "Study of a Continental Surface Albedo on the Basis of Flight Measurements and Structure of the Earth's Surface Cover Over North America," *Monthly Weather Review*, Vol. 92, No. 12, Dec. **1964**, pp. 543–564.

Landsberg, H., "Climatology," *Handbook of Meteorology*, McGraw-Hill Book Co., Inc., New York, **1945**, pp. 927–997.

London, J., "A Study of the Atmospheric Heat Balance," *Final Report*, Contract No. AF 19(122)-165, Department of Meteorology and Oceanography, New York University, **1957**, 99 pp.

Manabe, S., and Hunt, B. G., "Experiments With a Stratospheric General Circulation Model: I. Radiative and Dynamic Aspects," *Monthly Weather Review*, Vol. 96, No. 8, Aug. **1968**, pp. 477–502.

Manabe, S., and Smagorinsky, J., "Simulated Climatology of a General Circulation Model With a Hydrologic Cycle: II. Analysis of the Tropical Atmosphere," *Monthly Weather Review*, Vol. 95, No. 4, Apr. **1967**, pp. 155–169.

Manabe, S., Smagorinsky, J., and Strickler, R. F., "Simulated Climatology of a General Circulation Model With a Hydrologic Cycle," *Monthly Weather Review*, Vol. 93, No. 12, Dec. **1965**, pp. 769–798.

Manabe, S., and Strickler, R. F., "On the Thermal Equilibrium of the Atmosphere with a Convective Adjustment," *Journal of the Atmospheric Sciences*, Vol. 21, No. 4, July **1964**, pp. 361–385.

Mintz, Y., "Very Long-Term Global Integration of the Primitive Equations of Atmospheric Motion," *WMO Technical Note* No. 66, World Meteorological Organization, **1965**, pp. 141–161.

Möller, F., "Vierteljahrskarten des Niederschlags für die ganze Erde," (Quarterly Charts of Rainfall for the Whole Earth), *Petermanns Geographische Mitteilungen*, Vol. 95, No. 1, **1951**, pp. 1–7.

Namias, J., "General Aspects of Extended Range Forecasting," *Compendium of Meteorology*, American Meteorological Society, **1951,** pp. 802–813.

Namias, J., "Quasi-Periodic Cyclogenesis in Relation to the General Circulation," *Tellus*, Vol. 6, No. 1, Feb. **1954,** pp. 8–22.

Namias, J., "Long Range Weather Forecasting—History, Current Status, and Outlook," *Bulletin of the American Meteorological Society*, Vol. 49, No. 5, May **1968,** pp. 438–470.

Oort, A. H., "On Estimates of the Atmospheric Energy Cycle," *Monthly Weather Review*, Vol. 92, No. 11, Nov. **1964,** pp. 483–493.

Panel on International Meteorological Cooperation to the Committee on Atmospheric Sciences, National Academy of Sciences—National Research Council, October 1965, "The Feasibility of a Global Observation and Analysis Experiment," *Bulletin of the American Meteorological Society*, Vol. 47, No. 3, Mar. **1966,** pp. 200–220.

Petterssen, S., Bradbury, D. L., and Pedersen, K., "The Norwegian Cyclone Models in Relation to Heat and Cold Sources," *Geofysiske Publikasjoner*, Oslo, Vol. 24, No. 9, **1962,** pp. 243–280.

Posey, J., and Clapp, P. F., "Global Distribution of Normal Surface Albedo," *Geofisica Internacional*, Vol. 4, No. 1, Jan. **1964,** pp. 33–48.

Reed, R. J., "A Graphical Prediction Model Incorporating a Form of Nonadiabatic Heating," *Journal of Meteorology*, Vol. 15, No. 1, Feb. **1958,** pp. 1–8.

Sadler, J. C., "Monthly Cloud Cover Over the Tropics From Satellite Observations," paper presented at 5th Technical Conference on Hurricanes and Tropical Meteorology, Caracas, Venezuela, November 20–27, **1967.**

Saltzman, B., "On the Theory of the Mean Temperature of the Earth's Surface," *Tellus*, Vol. 19, No. 2, May **1967,** pp. 219–229.

Sawyer, J. S., "Notes on the Possible Physical Causes of Long-Term Weather Anomalies," *WMO Technical Note* No. 66, World Meteorological Organization, **1965,** pp. 227–248.

Smagorinsky, J., "On the Dynamical Prediction of Large-Scale Condensation by Numerical Methods," *Geophysical Monograph* No. 5, American Geophysical Union, **1960,** pp. 71–78.

Smagorinsky, J., Manabe, S., and Holloway, J. L., Jr., "Numerical Results From a Nine-Level General Circulation Model of the Atmosphere," *Monthly Weather Review*, Vol. 93, No. 12, Dec. **1965,** pp. 727–768.

Smagorinsky, J., Strickler, R. F., Sangster, W. E., Manabe, S., Holloway, J. L., and Hembree, G. D., "Prediction Experiments With a General Circulation Model," *Proceedings of the International Symposium on Dynamics of Large Scale Processes in the Atmosphere, Moscow, USSR, June 23–30, 1965*, Izdatel stvo ʼʼnaukaʼʼ, Moscow, **1967,** pp. 70–134.

Spar, J., "A Vertically Integrated Wet, Diabatic Model for the Study of Cyclogenesis," *Proceedings of the International Symposium on Numerical Weather Prediction, Tokyo, November 7–13, 1960*, Meteorological Society of Japan, **1962,** pp. 185–204.

Sverdrup, H. U., Johnson, M. W., and Fleming, R. H., *The Oceans, Their Physics, Chemistry and General Biology*, Prentice-Hall, Inc., New York, **1942,** 1,087 pp.

Syōno, S., and Yamasaki, M., "Stability of Symmetrical Motions Driven by Latent Heat Release by Cumulus Convection Under the Existence of Surface Friction," *Journal of the Meteorological Society of Japan*, Tokyo, Vol. 44, No. 6, Dec. **1966,** pp. 353–375.

Telegadas, K., and London, J., "A Physical Model of the Northern Hemisphere Troposphere for Winter and Summer," *Scientific Report* No. 1, Contract No. AF 19(122)-165, Research Division, College of Engineering, New York University, Feb. **1954,** 55 pp.

U.S. Navy Hydrographic Office, *World Atlas of Sea Surface Temperature*, Washington, D.C., **1944,** 48 pp.

World Meteorological Organization, The Joint CAe/CSM Working Group on Numerical Weather Prediction, "The Present Situation With Regard to the Application of Numerical Methods for Routine Weather Prediction and Prospects for the Future," *WMO Technical Note* No. 67, WMO-No. 165, **1965,** 64 pp.

Wolff, P. M., "The Error in Numerical Forecasts Due to Retrogression of Ultra-Long Waves," *Monthly Weather Review*, Vol. 86, No. 7, July **1958,** pp. 245–250.

CORRECTION NOTICE

Vol. 96, No. 5, May 1968, pp. 271–272: equations (18), (19), and (20) should read

$$U_* = \frac{kU(\Delta z + h\lambda)}{\frac{\Delta z}{h + z_0} \cdot \phi_M\left(\frac{h}{L}\right) + \int_0^h \frac{\phi_M\left(\frac{z}{L}\right)}{z + z_0}\,dz} \tag{18}$$

$$\theta_* = \frac{k[\theta(\Delta z + h) - \theta_0]}{\frac{\Delta z}{h + z_0} \cdot \phi_H\left(\frac{h}{L}\right) + \int_0^h \frac{\phi_H\left(\frac{z}{L}\right)}{z + z_0}\,dz} \tag{19}$$

$$q_* = \frac{k[q(\Delta z + h) - q_0]}{\frac{\Delta z}{h + z_0} \cdot \phi_q\left(\frac{h}{L}\right) + \int_0^h \frac{\phi_q\left(\frac{z}{L}\right)}{z + z_0}\,dz} \cdot \tag{20}$$

Also on p. 272 add the following paragraph just above "GROUND TEMPERATURE."

The values of K_M, K_H, and K_q obtained from the formulation of Estoque [3] when $0 \leq R_i \leq 0.2$ and the formulations explained above in respect of the other ranges of R_i are assigned to the level $z = h$. A linear fall of this value to $\frac{1}{10}$th at $H = 2050$ m is assumed.